PhD-FSTC-2018-28
The Faculty of Sciences, Technology and Communication

DISSERTATION

Presented on 24/04/2018 in Luxembourg

to obtain the degree of

DOCTEUR DE L'UNIVERSITÉ DU LUXEMBOURG

EN PHYSIQUE

by

Nils Reiners
Born on 4 February 1982 in Büdingen (Germany)

ANGLE AND SPECTRAL DEPENDENCE OF THE INTERNAL AND THE EXTERNAL QUANTUM EFFICIENCY OF SOLAR MODULES

Abstract

Reviewing scientific publications in the field of photovoltaic research, it becomes apparent that most of the investigations are carried out under perpendicular light incidence even though many of the relevant processes in a solar cell or module may strongly depend on the angle of incidence. The reasons for this are most likely due to three facts. Firstly, the equipment that is available for measurements and characterization in research laboratories is mainly constructed for perpendicular incidence. Secondly, the complexity of the analysis strongly increases when the angle of incidence is considered and thirdly, there is still a lack of standardization, which makes it difficult to compare the performance of solar modules at oblique incidence.

Regarding the maximization of the annual energy yield of a solar module it is crucial to be aware of operating conditions in the field. It is obvious that most of the time, light is incident on the module's surface with an oblique angle. However, it is not sufficient to investigate the short circuit current density effects due to the variation of the angle of incidence as it is often done. The reflection and absorption properties of the materials in a solar module generally vary with the wavelength of the incident light. This is the reason why it is convenient to take the angular and the spectral performance of solar modules into account simultaneously.

In this thesis a synopsis of all the relevant angle and spectral dependent effects is presented for silicon solar cells and modules. It is shown that not only optical effects are occurring, but that the internal quantum efficiency (IQE) also varies with the angle of incidence. It is also shown to which extent the implementation of textured surfaces influences the angle dependence of the external quantum efficiency (EQE) and the IQE. The analysis is performed using a newly developed analytical solar cell model that takes into account all relevant parasitic absorption processes in an untextured solar cell. Using an effective angle approach, the analysis can be extended to a textured solar cell. For more complex structures, a ray tracing tool was developed that is capable of simulating several textured layers and subsequently, of determining the corresponding EQE and IQE at all desired angles of incidence.

The angle and spectral dependence of the cells and modules under investigation were determined using measurement equipment that was particularly constructed for this purpose. The angle dependence of the EQE of the samples was determined with two different systems: A filter monochromator to determine the spectral response and by transforming the electroluminescence spectrum of the samples to the EQE using the opto-electronic reciprocity relation of solar cells. To determine the angle dependence of the IQE, a measurement setup was constructed for the determination of the angular reflection spectra.

Finally, the different angle and spectral dependent effects that were identified were analyzed with respect to their influence on the energy yield estimation of standard solar modules under outdoor conditions.

Contents

List of Figures

List of Tables

1 Introduction

The established global energy system, defined by the IPCC as all "components related to the production, conversion, delivery, and use of energy" [1], is causing several fundamental problems for humanity. Starting with the electricity production by means of nuclear fission, the events in Fukushima in March 2011 showed again the danger for people who live in the proximity of nuclear power plants. Besides this permanent hazard, there is still no satisfactory solution available for the appropriate management of the nuclear waste. Seven of the multiple fission products are classified as LLFP (long-lived fission products) meaning that they have a half-life of 211,000 years and more [2]. Thus, many generations to come will have to deal with the cost and health issues that are caused by this nuclear waste.

Burning fossil fuels in power plants (coal, oil, and gas), generators, industrial plants, and in vehicles is causing, among other problems, immense emissions of, e.g. particulate matter and nitrogen oxides. According to the European Environmental Agency (EEA) in 40 countries of the European Union alone, 491,000 people prematurely died as a result of the high air pollution in 2012, which is to a large extent created by the energy system driven by fossil fuels [3].

The exploitation of fossil fuels generally leads to the destruction of the environment. Damaged pipelines and oil drilling platforms pollute soil and water. By digging for lignite and oil sands, large territories containing forests and rivers are completely transferred into veritable lunar landscapes.

But as if these were not yet enough reasons to ban fossil fuels; the most harmful of the consequences has not even been mentioned. Due to the excessive burning of fossil fuels and the consequential emissions of greenhouse gases, the mean temperature of the planet is increasing, which is leading to what is generally referred to as climate change [4]. Already today many people are suffering from the impacts of global warming. If the temperature increases by more than 3°C as projected, millions of people will lose their livelihood due to an increasing frequency of extreme weather events [5–8]. And this is not only because of the direct results of climate change, but also because of secondary political conflicts that will be triggered by scarce resources (e.g., water, farmland) and conflicts due to migration [9]. In addition, the extinction of rare species will increase, which will lead to a further reduction of biodiversity [10]. Concerning the biosphere as well as the complete climate system, it cannot be excluded that there are tipping-points, which if they are surpassed, would lead to an abrupt and permanent change of these systems [10, 11].

Even though the facts have been proven, many politicians in power and companies still deny the existence of evidence for climate change and keep on advocating low environmental requirements; thus, helping to destroy the basis of life for the present generation and those to come.

Ironically not only the facts about of the menace that is created by the further burning of fossil fuels are well-known, but also the solution to the problem is in principle very obvious.

The renewable energy technologies for the transition of our energy system exist and are already highly developed. Several serious studies showed that a transition to an energy system which entirely is based on renewable energy sources is possible [12, 13] and the costs for this conversion would soon fall below those that would result from remaining with the status quo with all its destructive consequences [13].

One major element of an energy transition will be the usage of the overwhelming energy that is sent to the earth by the sun each and every day. There are different ways to use the sun's energy for heating, industrial processes, and electricity production. Photovoltaics (PV) is currently the most common technology for solar electricity production. Photovoltaic can be defined as a technology that is using semiconducting materials to make use of the photo electric effect for electricity production. Different semiconducting materials and material compositions are available that are manipulated and combined to effectively separate and collect the free charge carriers that are generated by the absorption of photons [14].

This thesis solely investigated crystalline silicon solar cells and modules. It is currently the most common of all PV technologies in terms of installed module production capacity as well as in terms of installed electricity production capacity [15]. Furthermore, many decades of research and production have led to a very sophisticated product and an in-depth understanding of the physics of this solar cell type. Nevertheless, there are still many open questions concerning applied and fundamental research, which need to be addressed by further activities [16, 17].

The research topic that is addressed by this thesis is the analysis of all effects, which act on the performance of the solar cell when the angle of incidence (AOI) is different from perpendicular incidence. The relevance of this research topic becomes clear when looking at the distribution of angles of incidence that occur during the course of a year. This distribution of the AOI is plotted in Fig. 1.1 a) for the German town Lindenberg in 2004, which received a global radiation of 1073 kWh/m², which is comparable to the German mean value. The non-averaged data with one-minute resolution was provided by the German Meteorological Service (DWD) [18]. The distributions of the AOI for five different module tilt angles and an orientation to the south are presented in the figure. It can be seen that low values for the AOI are very rare also for the typical orientation of a 45° tilt angle. Modules that are horizontally positioned (0° tilt angle) mainly experience high AOI with a peak at 75°. Façade modules (90° tilt angle) and modules with a tilt angle of 20° also receive a high share of the radiation with a highly oblique AOI.

Regarding the energy that the modules receive in form of direct radiation at a specific AOI, it can be observed in Fig. 1.1 b) that a high share of it is incident at a high AOI, which is particularly true for the tilt angles 0°, 20° and 90°. Against this background is becomes apparent how important it is to optimize solar modules not only for perpendicular but also for oblique angles of incidence.

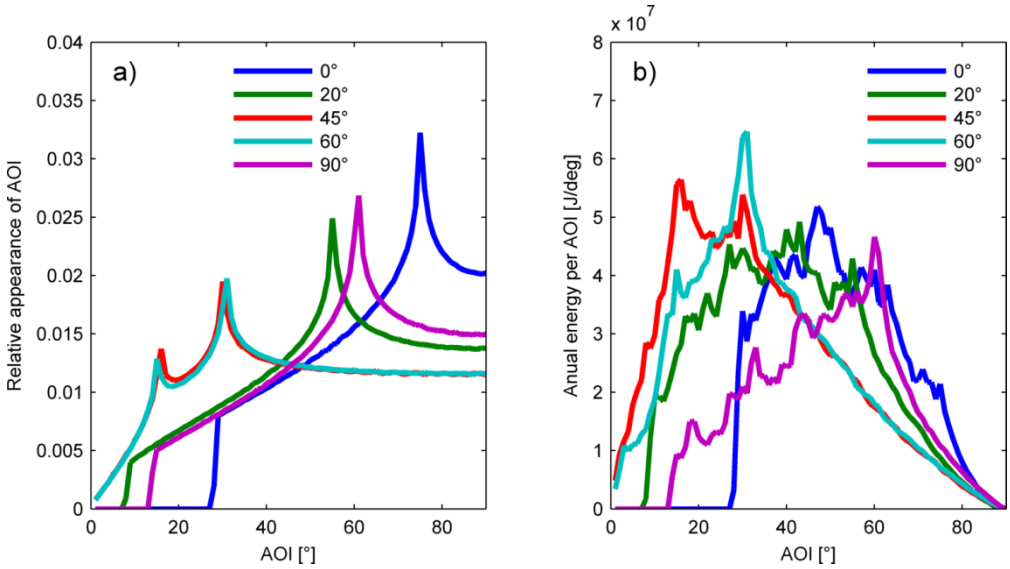

Fig. 1.1: Relative appearance of the AOI on a module surface with five different tilt angles for the town Lindenberg in the year 2004 a) and the corresponding annual energy from direct radiation that is incident on these modules with a specific AOI b)

For the state of the art energy yield prediction, the so-called incidence angle modifier (IAM) is applied. More details on this approach are given in section 2.2. However, even though much research has been done on the angular behavior of solar cells, the corresponding analysis has been mainly done without spectral resolution. Only a few research papers in the literature investigate the angle dependence as a function of wavelength. Carolin Ulbrich [19] performed a detailed analysis for the technology of amorphous solar cells and amorphous tandem solar cells, which of course are not directly comparable to the standard crystalline silicon (c-Si) technology. Dennler et al. [20] performed simulations of the angle dependence of the EQE and the IQE in bulk-heterojunction organic solar cells. Concerning the angle dependence of the EQE of c-Si cells and modules, two papers were published just recently: Geisemeyer et al. [21] presented the SR (spectral response) measurement results for solar cells with different front side textures at various AOI. For the bare cells as well as for the encapsulated cells they concluded: "The spectral responsivity of typical PV devices can significantly vary for different AOI". Unfortunately, no further theoretical investigation on the different effects which are involved in this process was given. Plag et al. [22] presented a detailed analysis of the measurement equipment for the determination of the angular EQE determination at the PTB (Federal Institute of Physical Technology in Braunschweig) and also concluded that a strong spectral variation with a change in AOI was measured. Here again, no detailed analysis of the different effects involved was given.

This thesis supplies the missing elements and presents all of the relevant effects that influence the angular and spectral performance of a silicon solar cell. The detailed investigation does not only explore the optical effects, but a particular focus is set on the analysis of the electrical effects incorporated into the IQE.

First of all, the fundamentals are presented which are needed to fully understand the physics behind the performed simulations and measurements. The next section presents the simulation tools that were developed to investigate the angular and spectral effects in detail. A newly developed analytical solar cell model is introduced and subsequently the ray tracing software that was named SMARTI is explained in detail.

In the section that follows the measurement equipment is described that was particularly constructed for the angle dependent EQE and IQE measurements performed for this thesis.

In section 5 the results of the measurements and simulations for different solar cell and module configurations are presented. First of all, the results for an untextured mono-c-Si solar cell is shown. This cell type does not represent a type that is used in todays solar modules, but it however allows to clearly distinguish the reflection mechanisms, the different parasitic absorption processes and the desired absorption in the semiconductor. Thereafter the identified optical and electrical processes are analyzed for a standard solar module containing a textured mono-c-Si solar cell. After this the effects of replacing the planar front side encapsulant by a textured encapsulant are described. Finally, the relevance of the different angle and spectral dependent effects concerning the output performance and hence the energy yield prediction is presented.

2 Fundamentals

2.1 Typical build-up of a crystalline silicon solar module

As this thesis focuses on the photovoltaic technology that is based on crystalline silicon, the components that make up a typical module of this type are presented in more detail in the following. The buildup of a typical c-Si solar module is schematically depicted in Fig. 2.1.

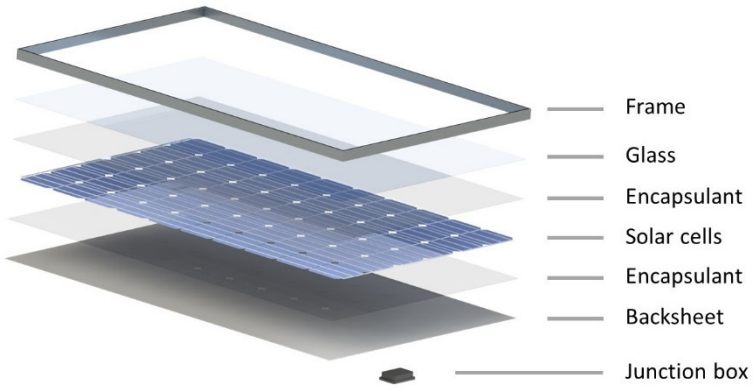

Fig. 2.1: Schematic representation of the buildup of a typical solar module with crystalline silicon solar cells

The current standard front glass sheets for photovoltaic applications have thicknesses of about 3.2 mm and are made of low-iron soda-lime-silica-glass. It is also referred to as "ultra-white" glass to indicate its high solar transmissivity [23]. In addition to the good optical performance, this glass type exhibits superior physical and chemical protection characteristics at low costs [24]. The production of flat glass can be performed by two different manufacturing processes: A float process, where the molten glass is poured onto the surface of molten tin, resulting in very plane mirror-like surfaces and a roller process where the molten glass is pressed by a pair of rollers to a ribbon of glass with the desired thickness. When applying the roller process, textures of different kinds can be implemented onto the surface of the glass [23]. These manufacturing steps are usually followed by a tempering process, which increases the mechanical stability of the glass sheet. Furthermore, it is possible to apply an anti-reflective coating onto the upper glass surface. Common processes for the application of such coatings are the Sol-gel process for rolled glass and a sputtering process for float glass [24, 25].

A typical solar module contains 60 solar cells (10 x 6) of either poly- or mono-crystalline silicon (poly-c-Si, mono-c-Si). The cells have contact fingers on the top, which are applied by a screen printing process. Tin plated copper ribbons are then applied to the busbars that are part of the front side grid and connect it to the back side contact of the neighboring solar cell [26]. The back side of the solar cell is mainly made from a screen-printed layer of aluminum, which forms an eutectic compound with silicon ($AlSi$). A back surface field is resulting that prevents the majority charge carriers from recombining at the back

surface [27]. Even though the $AlSi$ back surface contact scheme is still the standard in industry, for mass production, a new technology that can be summarized under the acronym PER(X)[1] is replacing more and more conventional production lines [28]. The core element of the PER(X) technology family is the surface passivation by the implementation of thin dielectric layers [28].

Two screen printed busbars made from silver paste are applied on the back side beneath the busbars at the front to effectively collect the minority charge carriers [27].

The front surfaces of the solar cells are textured and typically a silicon nitride (SiN_x) AR-coating is subsequently added by means of PECVD (Plasma Enhanced Chemical Vapor Deposition). The texturing on the surface of mono-c-Si cells is done by means of KOH (potassium hydroxide)-etching [29], which leads to a texture consisting of pyramids with randomly distributed positions and heights whereas the orientation of the facets is constant as well as the base angle of the pyramid which in theory is $\arctan(\sqrt{2}) = 54.74°$ but can differ from this value in standard industrial production processes [30]. For the texturing of multi-c-Si wafers a different etching procedure needs to be applied because of the inhomogeneously oriented crystals. This process is based on an isotropic acidic etching using HNO_3/HF. As the current multi-wire slurry sawing (MWSS) process is currently being replaced by a more cost effective diamond wire sawing (DWS) process, the etching procedure also needs to be reconsidered as the standard multi-c-Si etching process leads to unsatisfactory results when DWS is used [31].

The solar cells are encapsulated between the glass layer and the back sheet using a transparent synthetic material. The typical encapsulation material for standard modules is duroplastic cross-linked EVA (ethylene-vinyl-acetate) [32], whereas for glass-glass modules that are mainly used for BIPV (building integrated photovoltaic), the thermoplastic encapsulation material PVB (polyvinyl butyral) is the common encapsulation material [33].

The back sheet of a standard solar module needs to protect the cells against mechanical stress and degradation and it needs to provide electrical insulation. Here the most common product type consists of a three-layer stack that is referred to as TPT (Tedlar®/PET/Tedlar®) [23, 34].

2.2 Angle of incidence effects in energy yield prediction procedures

In optimizing solar modules, it is crucial to distinguish between efficiency optimization and energy yield maximization. A module, which is optimized for high efficiency, does not necessarily provide a higher annual yield compared to a module with lower efficiency. This is due to the fact that efficiency measurements are carried out under standardized test

[1] The 'X' can be replaced by either 'C' indicating the notation PERC (mainly: Passivated Emitter and Rear Cell, sometimes: Passivated Emitter and Rear Contact), or 'T' for PERT (Passivated Emitter Rear Totally-diffused) or by 'L' indicating the PERL cell (Passivated Emitter Rear Locally-diffused). Other less common abbreviations are PERD (Passivated Emitter and Rear Directly-contacted) and PERF (Passivated Emitter, Rear Floating-junction) [28].

conditions (STC), at which the module temperature is kept at 25°C, the light intensity is set to a value of 1000W/m², the spectrum of the radiation is standardized to an air mass (AM) value of 1.5, and the light's angle of incidence to the module's surface is perpendicular, i.e., 0° [35]. These conditions are extremely rare of course or never even occur in reality. Thus, it is not possible to estimate the energy yield of a solar system by solely knowing the STC results of a module. Multiple factors act on the performance of the module and need to be taken into account. The temperature of the module changes permanently. The intensity of the sunlight as well as its spectrum vary over the course of a day depending on the location and the orientation of the module[2]. The angle of incidence also changes permanently and for a PV-system with standard orientation, the perpendicular positioning of the sun to the module's surface only occurs twice a year. There are many other factors that influence the energy yield of a PV-system, making it extremely difficult to perform precise energy yield predictions [36]. The most important of these effects are weather phenomena (clouds, rain, fog, snow, etc.) [37], the shadowing caused by objects [38], soiling of the modules (dust, smog, organic particles, etc.) [39], ground reflection, degradation of modules [40, 41], system losses, and failure losses (defects in modules, inverters or periphery) [42, 43].

The most common strategy to estimate the energy yield of a PV-system is to calculate the output power for discrete time steps for a whole year. Often hourly steps are chosen and thus the year is divided into 8760 discrete steps. The weather data for each step mainly consists of mean values for the global radiation and the diffuse radiation on a horizontal plane, the ambient temperature, and the wind speed. Systematic investigations to find corresponding correction factors are needed to determine all of the factors that influence the energy yield. First, the output power of the solar module needs to be determined, followed by the inclusion of the system losses up to feeding into the electricity grid.

Different approaches for the estimation of the yearly energy output of a solar module have been developed and extensively compared to each other in various papers in the scientific literature [36, 44]. A typical approach for the power output estimation of a solar module is illustrated in Fig. 2.2. A similar approach is implemented in computer simulation tools such as the Sandia PV Array Performance Model (SAPM) [45], PV-Syst [46], PV-Sol [47], and others. First the short circuit density j_{sc} and the cell's temperature T_{cell} are determined as input into the calculation of the j-V curve. It is common to use the so-called single diode equivalent diode model for which the saturation current density j_0, the shunt resistance R_{sh}, the series resistance R_s and the diode ideality factor m are needed as fitting parameters [48]. These variables are generally determined by j-V-measurements in a solar flashing system. The maximum power point P_{mpp} is then obtained by finding the maximum value of the product of current density j and voltage V.

[2] The spectrum not only depends on where the radiation is coming from in the sky, but it also depends on how much of the ground reflected light with a different spectrum will be incident on the module's surface.

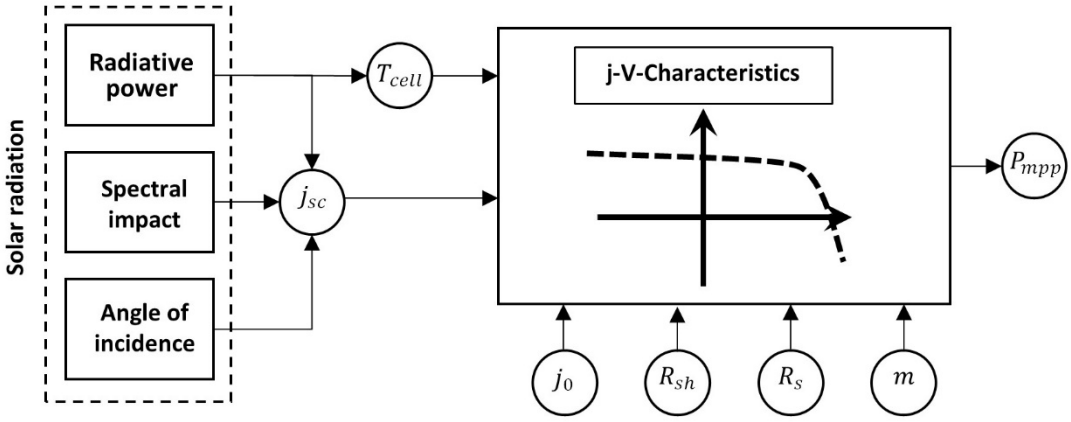

Fig. 2.2: Symbolic representation of a standard procedure for the yield estimation of a PV-module

One step is to evaluate the temperature dependency of the modules by the determination of the temperature coefficients, which allow translating the j-V-curve of the solar module at 25°C to any other temperature [49]. However, the cell temperature of the cell T_{cell} at the specific ambient temperature and irradiation needs to be known. To account for this effect, the normal operating cell temperature ($NOCT$) is defined. It is the measured temperature that the solar cell has at 800 W/m², 20°C ambient temperature, and a wind speed of 1m/s. Now a linear dependency of the cell's temperature and the incident light intensity is assumed. The equation for the determination of the cell's temperature using the $NOCT$ value is given in (A.1) in the appendix [50].

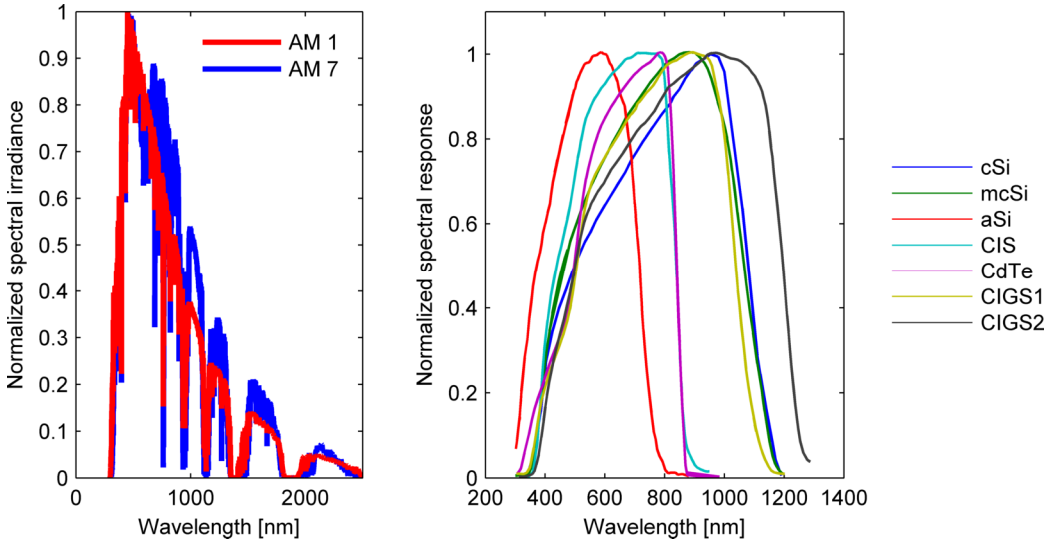

Fig. 2.3: a) Simulated solar spectra for AM 1 and AM 7 using the software SMARTS2, b) Examples for normalized spectral response curves of different solar cell technologies (cSi: crystalline silicon; mcSi: multi crystalline silicon; aSi: Amorphous silicon; CIS: Copper indium selenide; CdTe: Cadmium telluride; CIGS: Cupper indium gallium selenide)

To include the influence of a changing solar spectrum, it is common to derive a correction factor, which depends on the air mass that the light needs to traverse before hitting the module's surface. The shape of the solar spectrum that reaches the earth's surface is influenced by absorption, and Rayleigh or Mie scattering on atmospheric particles. Using

the software SMARTS2, it is possible to generate solar spectra with different AM values [51] not accounting for clouds. The simulated spectra for the air mass 1 and 7 are plotted in Fig. 2.3 a), which clearly shows the strong influence of the air mass on the solar spectrum.

As the SR of a solar module generally stays constant at perpendicular incidence, a changing solar spectrum will therefore influence the short circuit current (j_{sc}). Depending on the technology, the SR can strongly vary and so will the spectral influence. Typical normalized SR curves of various photovoltaic technologies can be seen in Fig. 2.3 b) [51].

The factor for the spectral correction of the short circuit current is called the air mass correction factor f_{AM} here, which is defined as [52]

$$f_{Am} = \frac{\frac{I_{g,0}}{I_g(AM)} \cdot j_{sc}(AM)}{j_{sc,0}} = \frac{\frac{I_{g,0}}{I_g(AM)} \cdot \int_a^b I_g(AM,\lambda) SR(\lambda) d\lambda}{\int_a^b I_{g,0}(\lambda) SR(\lambda) d\lambda}, \tag{1}$$

where $I_{g,0}$ is the global irradiation corresponding to the solar spectrum of AM 1.5g and $I_g(AM)$ is the irradiation resulting from the AM-spectrum under investigation. The short circuit current densities j_{sc} are determined at perpendicular incidence. The factor f_{AM} can either be calculated using measurement values of I_g and j_{sc} when the spectrum is equal to the AM 1.5g and when the spectra are of any other AM value. If the SR of the corresponding cell or module is known it is possible to calculate f_{AM} using the integral form of (1) together with simulated or measured spectra at different AM.

The AM correction factors for different cell technologies are plotted in Fig. 2.4. Looking at the SR data in Fig. 2.3 b), it is evident that a shift of the solar spectrum to longer wavelengths will cause less photons to be absorbed by an amorphous cell and more to be absorbed by a cell with a low bandgap, such as crystalline or CIGS technology.

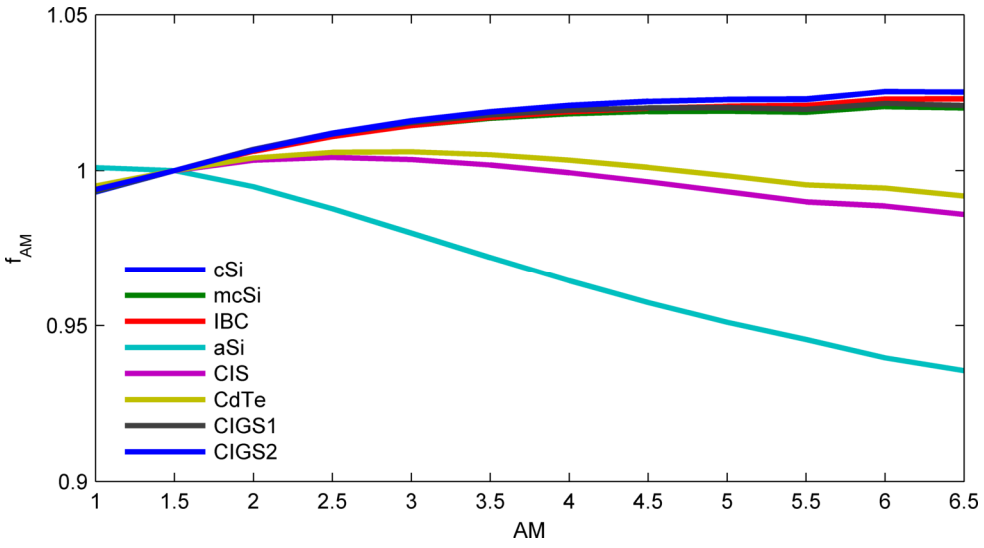

Fig. 2.4: Spectral correction factors for different solar cell technologies calculated from spectra of different AM simulated with SMARTS2 and the SR curves from Fig. 2.3 b)

The third factor for the correction of the short circuit current is the angle of incidence. The significance of this factor for the energy yield prediction can be seen in Fig. 2.5, where four typical examples are depicted in which PV-modules experience oblique light situations. It can be seen that these situations not only occur at installations that are not perfectly oriented (examples 1 and 2), but also for best possible orientations (examples 3 and 4).

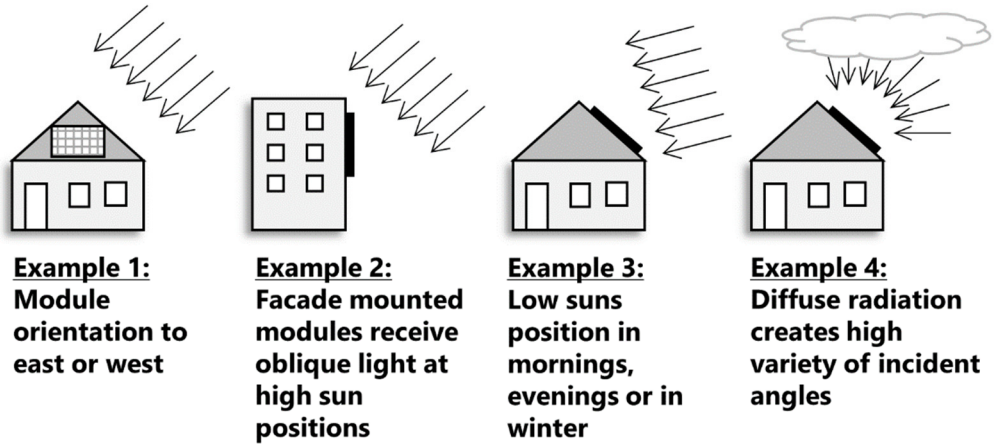

Fig. 2.5: Situations in which oblique light incidence plays an important role for the performance of the PV-module

While the first three examples all show situations where the oblique incidence is direct irradiation, the fourth example shows irradiation under a cloudy sky, i.e., a high share of diffuse radiation. It is important to note that under diffuse light conditions, a high share of the photons is incident on the module surface with a steep angle of incidence. Thus, understanding the oblique light performance of solar modules is crucial to understand its diffuse light performance [53].

The standard procedure to account for the effect of a changing incident angle on the short circuit current of a module is applying the so-called incidence angle modifier (IAM) [54][3]. It is defined as the ratio of the short circuit current density measured at an angle of incidence θ_{aoi} and the short circuit current density at perpendicular incidence. The value of $j_{sc}(\theta_{aoi})$ corrected by $\cos(\theta_{aoi})$ to eliminate the cosine effect and to keep all other angular effects.

$$IAM(\theta_{aoi}) = \frac{j_{sc}(\theta_{aoi})}{j_{sc,0} \cdot \cos(\theta_{aoi})} \tag{2}$$

It is important to know that these measurements are performed under a static solar spectrum and that this definition strictly holds only for modules with a perfect directional symmetry. The measurement of the IAM can either be performed indoors with the help of a solar simulator [55] or it can be determined outside under clear sky conditions using a solar tracking device [54]. Within the framework of this thesis a solar tracking device was constructed at the Cologne University of Applied Sciences (CUAS) which is capable of

[3] In the literature, different names are used for the same angular factor, e.g., $f_{I\alpha}$ [55] or $K_{I_{sc}}$ [56].

measuring the IAM of solar cells and whole modules. The solar tracking system is shown at the left side of Fig. 2.6.

Fig. 2.6: Left: Solar tracking system at the Cologne University of Applied Sciences. Right: Outdoor measuring station for the continuous determination of the module performance. The module tilt angle can be varied. The door is oriented to the east.

A further possibility to determine the IAM is the evaluation of long term outdoor performance measurements. The advantage of this technique is that many data points are available for many different outdoor conditions and thus a representative value can be extracted. However, correction procedures for the temperature are needed which adds another source of uncertainty. The measuring station which was constructed for this purpose at the CUAS can be seen at the right side of Fig. 2.6.

The procedure for the energy yield prediction of a solar module as described above was designed in this form to avoid handling the complete spectra in the simulation procedure. The reasons for choosing this approach can mainly be found in a lack of spectral data, lower computational load and an assumed reduction in complexity.

Even though these arguments are still valid, a revision of the current procedure should be considered as there are now reliable tools for the simulation of solar spectra, computational power has increased and is further increasing so that limitations are not necessary anymore and the handling of solar spectra and spectral response curves has provided many more insights into the physics of the investigated designs.

Here it needs to be emphasized that present studies underline the shift of the spectral response when the angle of incidence is changed [21]. In principle, these effects are included in the IAM, but only for the standard spectrum that prevailed during the

measurements. If the angle of incidence and the spectrum are changing at the same time, which is standard, the procedure does not account for the combined effect.

2.3 Geometrical optics and wave optics

A fundamental new understanding of light was developed when the quantum hypothesis was formulated by Max Planck, Albert Einstein, and others. The central idea of the theory that particular quantities (such as the energy of a photon) can only have distinct values, allowed combining the particle theory and the wave theory of light into one unified theory. This was the birthday of wave particle dualism: A photon is a quantum of energy that carries properties of both waves and particles at the same time. This is very counterintuitive and the reason why mathematical terms are needed to obtain a more in-depth description of the phenomenon of light.

A photon is said to be an "elementary particle" that describes a structure that is not composed of smaller parts. It belongs to the family of the bosons, i.e., it obeys Bose-Einstein statistics (particles that do not obey Pauli Exclusion Principle restrictions). A photon has no rest mass, which causes it to always travel with the maximum possible speed, the speed of light c_0. The energy of a photon is directly linked to its frequency f. The frequency is proportional to the wavelength by $\lambda = c_0/f$ such that the energy can be calculated with the help of Planck's constant h by [57]

$$\mathrm{E}_{ph} = \frac{hc_0}{\lambda} \tag{3}$$

While light, in the narrower sense, only refers to the electromagnetic radiation that can be received by the human eye (380 nm to 780 nm), here a broader definition will be used that includes ultraviolet (10nm to 380nm) and infrared light (780nm to 1mm).

It is not necessary to fully include the wave properties of light for many applications, e.g., simulating the light path along the mirrors and through the lens of a torch or an illumination study for a street lamp. For these kinds of problems, light is handled as streams of particles or as rays that are following simple rules of reflection, refraction, and absorption. This kind of procedure or method is commonly referred to as geometrical optics. Even though many problems can be handled that include effects based on the wave nature of light, such as polarization or dispersion, for some tasks, it is mandatory to fully calculate light propagation using mathematical wave descriptions. The field that describes this approach is called wave optics and the applications are for example anti-reflection-coatings (AR-coatings), Fourier optics, holography, and many others.

In the following, the basic wave optic equations are described that are needed to fully understand reflection, refraction, and absorption as the fundamental processes of light and matter interaction. These equations are furthermore needed to describe the angular optics of the anti-reflection coating that is normally applied onto the top of a solar cell.

As mentioned above, light can be described as an electromagnetic wave. Here it is important to understand that the magnetic field H and electric field E always mutually

produce each other and they are always perpendicular to each other. As the amplitude of the two fields fluctuates up and down and both are perpendicular to the direction in which the wave travels, they are called transversal waves. If the two fields are thought of as vectors and the cross product is formed, the result is a vector called the pointing vector $\vec{S}$, which represents the directional energy flux density. So the right-hand rule gives us the direction of the energy flow if the direction of the fields H and E are known.

The orientation of the electric field is called the polarization of light. The corresponding reference plane is the one created by the incident and the reflected beam. Two different orientations of the polarization can be distinguished: Perpendicular or s-polarization (s for the German "senkrecht") and parallel or p-polarization (p for the German "parallel"). All polarization directions in other angles can be seen as compositions of s- and p-polarized fields. The direction can also continuously change over time, which is then called elliptically polarized light [58].

The mathematical description of how the electric field $\boldsymbol{E}$ and the magnetic field $\boldsymbol{B}$ are generated by charges and currents and how they influence each other is given by four partial differential equations. These were composed by James Clerk Maxwell, they are referred to as Maxwell's Equations [59].

$$\nabla \cdot \boldsymbol{E} = \frac{\rho}{\varepsilon} \tag{4}$$

$$\nabla \cdot \boldsymbol{B} = 0 \tag{5}$$

$$\nabla \times \boldsymbol{E} = -\frac{\partial \boldsymbol{B}}{\partial t} \tag{6}$$

$$\nabla \times \boldsymbol{B} = \mu\sigma\boldsymbol{E} + \mu\varepsilon\frac{\partial \boldsymbol{E}}{\partial t} \tag{7}$$

where ρ is the total electric charge density and σ the material dependent conductivity. The variable ε is the material dependent permittivity (measure of resistance that is encountered when an electric field forms) and μ is the material dependent permeability (measure of the ability of a material to support the formation of a magnetic field within itself). Both ε and μ can be determined from their vacuum values ε_0 and μ_0 by $\varepsilon = K_E\varepsilon_0$ and $\mu = K_M\mu_0$ where K_E is the relative permittivity (or dielectric constant) and K_M is the relative permeability.

Combining (6) and (7) results in the so-called telegrapher's equations for the electric and the magnetic field. The detailed procedure can be found in Hecht [59]. The equations for the electric and the magnetic field are very similar, but as the main share of the transported energy is carried by the electric field, which will be discussed later, most of the operations will be carried out on E.

$$\nabla^2\boldsymbol{E} = \varepsilon\mu\frac{\partial^2 \boldsymbol{E}}{\partial t^2} + \mu\sigma\frac{\partial \boldsymbol{E}}{\partial t} \tag{8}$$

This equation has the same structure as the general wave equation as it is known from the description of waves in mechanics, which provides strong evidence that the electric as well as the magnetic field propagates in the form of a wave.

One of the solutions of (8) is the equation of a plane-polarized plane wave propagating in the x-direction is

$$E = E_0 \exp\left(i\left(\omega t - \frac{N\omega}{c_0}x\right)\right) \tag{9}$$

where N is the complex refractive index

$$N = n - ik \tag{10}$$

The real part of this expression is the so-called refractive index of the material. It is defined as the relation of the velocity of light in vacuum to the velocity of light inside the material ($n = c_0/c_m$). The variable k in the complex part of the equation is referred to as the extinction coefficient and describes the absorption inside the material. The absorption coefficient α can be calculated from the extinction coefficient with $\alpha = 4\pi k/\lambda$.

We now want to describe what happens when light interacts with the interface of two media such as, air and glass. A share of the light is reflected back with an angle θ_r which is equal to the angle of incidence θ_i.

$$\theta_i = \theta_r \tag{11}$$

However, even though this seems to be very obvious, the process that leads to this reflection is not equivalent to a collision of two objects such as a billiard ball and the cushion of the billiard table. To understand the reflection as well as the refraction at the interface, the Huygens-Fresnel principle must be used that states that every photon is absorbed by an atom, which is then forced to oscillate and send out a spherical secondary light wave [60]. This scattering process is mainly elastic and leads to secondary waves that have the same wavelengths as the incident photon.[4] The emitted waves interact constructively and destructively, which leads to a directed reflection and refraction beam of light.

The angle of the refracted beam is determined by Snell's law, which for dielectric media such as glass, is given as

$$n_0 sin\theta_0 = n_1 sin\theta_1 \tag{12}$$

For absorbing media, the complex form of Snell's law has to be applied, substituting the real refractive index n by the complex refractive index N. For the proof of equations (11) and (12) geometrical arguments using the Huygens-Fermat principle can be applied or the treatment of the electromagnetic waves at a boundary can be used. Both derivations can be found in [59].

[4] Some of the photons are inelastically scattered. Inelastic scattering processes are Brillouin scattering, Raman scattering, inelastic X-ray scattering, and Compton scattering.

Thus, the angle of incident and the angle of reflection can be determined, but there is no information on the ratio of reflected and transmitted energy at the interface yet. This can be found using the fact that the components of the electric and the magnetic field, which are parallel to the boundary, need to be continuous at any location on the boundary at any time. All possible orientations of the electric and the magnetic field can be expressed as the combination of an s-polarized and a p-polarized type of wave. For these two cases of p- and s-polarized light, the interaction with the interface needs to be analyzed separately [61].

For all polarizations the electric field vector, the vector of the magnetic field strength ($\boldsymbol{H} = \boldsymbol{B}/\mu$) and the direction vector $\vec{r}$ are mutually perpendicular, so that

$$\boldsymbol{H} = NY(\vec{r} \times \boldsymbol{E}) \tag{13}$$

can be written, where $Y = 1/c_0 = \sqrt{(\varepsilon_0/\mu_0)} = 2.6544x10^{-3}S$ and is the characteristic optical admittance in free space.

To include all kind of materials into this derivation, the tilted optical admittance η must be introduced, which for the two polarizations are

p-polarization: $$\eta_p = NY/cos\theta \tag{14}$$

s-polarization: $$\eta_s = NYcos\theta \tag{15}$$

This leads to the amplitude reflection and amplitude transmission coefficient, which are denoted by ρ and τ respectively.

$$r_E = \frac{E_r}{E_i} = \frac{\eta_0 - \eta_1}{\eta_0 + \eta_1} \tag{16}$$

$$t_E = \frac{E_t}{E_i} = \frac{2\eta_0}{\eta_0 + \eta_1} \tag{17}$$

The transformation from this ratio of the wave amplitudes to the ratio of the energy transported by the waves is done with the help of the pointing vector. The corresponding derivation can be found in [61]. Using the complex conjugate (*), the reflection R and the transmission T at the surface can be written as

$$R = |r_E|^2 = r_E r_E^* = \left(\frac{\eta_0 - \eta_1}{\eta_0 + \eta_1}\right)\left(\frac{\eta_0 - \eta_1}{\eta_0 + \eta_1}\right)^* \tag{18}$$

$$T = |t_E|^2 = t_E t_E^* = \frac{4\eta_0 Re(\eta_1)}{(\eta_0 + \eta_1)(\eta_0 + \eta_1)^*} \tag{19}$$

These are the so-called Fresnel equations in very general forms. If they are applied to the case of a dielectric non absorbing media such as glass, the equation for the reflection can be expressed as

p-polarized: $$R_p = \frac{\sin(\theta_0 - \theta_1)^2}{\sin(\theta_0 + \theta_1)^2} \tag{20}$$

s-polarized: $$R_s = \frac{\tan(\theta_0 - \theta_1)^2}{\tan(\theta_0 + \theta_1)^2} \quad (21)$$

Unpolarized: $$R = \frac{1}{2}\left(\frac{\sin(\theta_0 - \theta_1)^2}{\sin(\theta_0 + \theta_1)^2} + \frac{\tan(\theta_0 - \theta_1)^2}{\tan(\theta_0 + \theta_1)^2}\right) \quad (22)$$

For the case of a low iron solar glass with an assumed refractive index of 1.5 at a wavelength of 500nm, a reflection curve as depicted in Fig. 2.7 is obtained. As the refractive index does not change significantly for other wavelengths, the reflection values can be assumed to be representative for the total reflection on the glass surface. While the reflection of unpolarized light is stable at a value of 4 % for incident angles of 0° to 30°, it strongly increases for higher angles of incidence. At 50°, the reflection increases to 5.8 % and at 60° it is already at 8.9 %. For the angles 70° and 80°, which are still relevant concerning the sun's position to a tilted solar module, there are very high reflection values of 17.1 % and 38.8 % respectively.

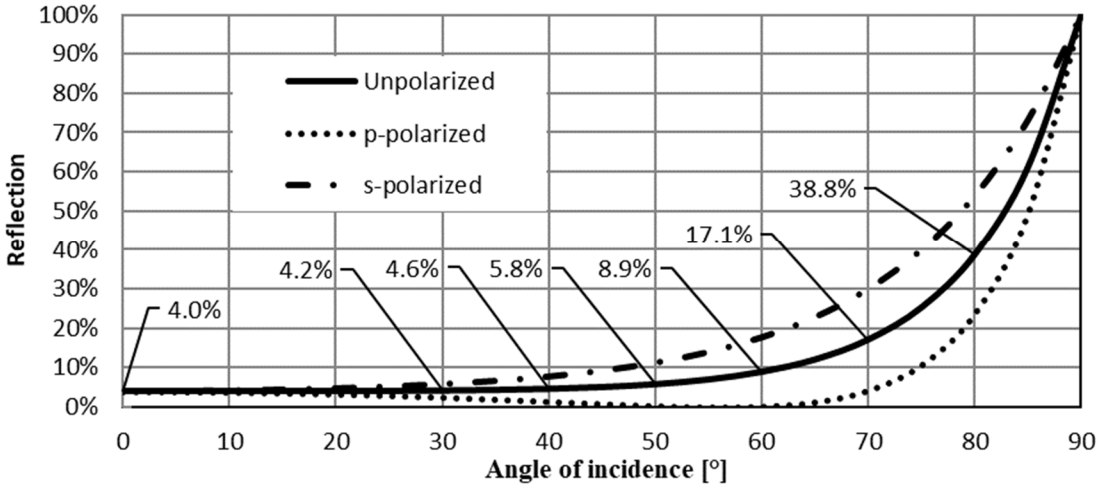

Fig. 2.7: Calculated reflection on the interface of air and a low iron solar glass with a refractive index of 1.5 at a wavelength of 500 nm

One possibility to decrease the reflection at low as well as at high angles of incidence is to apply an anti-reflective coating to the corresponding surface. The working principle builds upon the fact that two waves whose phases are shifted by a phase factor of π (phase condition) and whose amplitudes are equal (amplitude condition) experience a total destructive interference, meaning that no energy is flowing through this path. The two different waves are created at the top and the bottom of a thin layer. The thickness of this layer needs to be $d = \lambda/(4n)$ for perpendicular incidence, with n being the refractive index of the coating material. It is important to realize that the wavelength is shortened by the same amount (division by n) that the effective velocity of the photons is reduced. This can be deduced from equation (1) by realizing that energy has to be conserved even though the effective velocity is reduced [24].

A second condition to reduce the reflection to zero for a specific wavelength can be deduced from (23) that shows a simplification of Fresnel's law for the case of perpendicular incidence on an anti-reflective coating with a refractive index of n_s.

$$R = \left(\frac{n_s^2 - n_0 n_1}{n_s^2 + n_0 n_1}\right)^2 \tag{23}$$

It can easily be seen that the reflection becomes zero for the case of

$$n_s = \sqrt{n_0 n_1} \tag{24}$$

Calculating the reflection, the transmission, and the absorption of light at an AR-coating with multiple layers at any incidence angle is highly complex. A useful tool to do this is the so-called Transfer Matrix Method. A detailed description of this concept can be found in [61] and will only be briefly presented here.

First, the complex refractive indexes are defined for the ambient medium (N_0), the different layers (N_j), and the substrate to which the AR-coating is applied (N_m).

$$N_0 = n_0 - ik_0 \tag{25}$$

$$N_j = n_j - ik_j$$

$$N_m = n_m - ik_m$$

where $j = \{1, .., v\}$ with v being the number of layers applied to the substrate.

To implement the interaction of the waves reflected at the two interfaces of each layer, a factor is introduced that accounts for the phase shift that the waves experience when traversing the layer of thickness d_j extended by the cosine of the angle that the light adopts while traversing the layer.

$$\delta_j = \frac{2\pi N_j d_j \cos\theta_j}{\lambda} \tag{26}$$

The term for $\cos\theta_j$ can be found using the complex-valued Snell's law $N_0 \sin\theta_0 = N_j \sin\theta_j = N_m \sin\theta_m$. Leading to the expression

$$\cos\theta_j = \frac{\sqrt{N_j^2 - N_0^2 \sin^2\theta_0}}{N_j} \tag{27}$$

It is important to note that the angle inside the layer is not dependent on the angles or the refractive indexes of the layers above it, but only on the angle of incidence and the refractive index of the ambient medium.

The central strategy of the Transfer Matrix Method is to calculate the change that the electromagnetic wave experiences in every layer by the successive multiplication of a 2 x 2 matrix for every layer, each of which is called the characteristic matrix of the layer M [61].

$$\begin{bmatrix} B \\ C \end{bmatrix} = [M_1][M_2] \dots [M_v] \begin{bmatrix} 1 \\ \eta_m \end{bmatrix} = \left\{ \prod_{j=1}^{v} \begin{bmatrix} \cos\delta_j & (i/\eta_j)\sin\delta_j \\ (i\eta_j)\sin\delta_j & \cos\delta_j \end{bmatrix} \right\} \begin{bmatrix} 1 \\ \eta_m \end{bmatrix} \tag{28}$$

where v is the number of applied thin-films and η_m is the tilted optical admittance of the substrate. This expression forms the basis of nearly all calculations in thin-film optics [61] and is also of prime importance for the calculation of AR-coatings for photovoltaic devices. With the help of B and C, the total reflection, transmission, and absorption in the thin-film assembly can be calculated with

$$R = \left(\frac{\eta_0 B - C}{\eta_0 B + C}\right)\left(\frac{\eta_0 B - C}{\eta_0 B + C}\right)^* \tag{29}$$

$$T = \frac{4\eta_0 Re(\eta_m)}{(\eta_o B + C)(\eta_o B + C)^*} \tag{30}$$

$$A = \frac{4\eta_0 Re(BC^* - \eta_m)}{(\eta_o B + C)(\eta_o B + C)^*} \tag{31}$$

With the help of the derived equations, the optical properties of an interface with or without an anti-reflective coating can be calculated. However, in an optically thick layer, the light is not coherent anymore [62] and thus no systematic constructive or destructive interference is occurring. But in such a thick layer the light bounces forward and backwards several times, so that the light leaving the top and the bottom of this layer is the sum of all the subsequent interactions of the light with the surfaces.

There is a simple mathematical strategy to account for this effect that can be applied to find the total reflection R_{tot}, the total transmission T_{tot}, the total absorption A_{tot}, as well as the generation profile. The procedure will be exemplarily presented for the calculation of the total reflection.

To find the total reflection, the strategy is to sum up the photons that escape after each trajectory through the layer, up to n, so that an eternal sum is determined. For example, with a layer of thickness W and a flux of monochromatic photons ϕ_i that hit the layer with a perpendicular incidence, the first reflection on the external surface is referred to as R_{fe}, so that the flux of photons entering the layer is $\phi_{fi} = (1 - R_{fe})\phi_i$.

The strength of the absorption is a property of the material and can be described either with the extinction coefficient k or the absorption coefficient α. The extinction coefficient was already introduced as a part of the complex refractive index (10) that reduces the amplitude of the light wave as it moves through the medium. This reduction has an exponential form and can be expressed as

$$\frac{I(x)}{I_0} = \left(\frac{E(x)}{E_0}\right)^2 = \exp\left(-\frac{2k\omega}{c_0}x\right) = \exp\left(-\frac{4\pi k}{\lambda}x\right) = \exp(-\alpha x) \tag{32}$$

where $I(x)$ and I_0 are the irradiance at position x and the initial irradiance at $x = 0$ respectively. This relation is also referred to as the Beer-Lambert law.

Therefore, the flux of photons that is transmitted through the layer to reach the back side is $\phi_{fi}T_d = \phi_{fi}\exp(-\alpha W)$. Adding the reflectivity at the back side R_b and the front side R_f and the transmission for the photons on their way upwards $T_u = T_d = T$, the number of photons leaving the layer after one trajectory is

$$\phi_{esc,1} = \phi_i\big(1 - R_{fe}\big)T^2R_b(1 - R_f) \tag{33}$$

To find the number of photons that escape after subsequent trajectories, the process is continued and results in

$$\phi_{esc,2} = \phi_i\big(1 - R_{fe}\big)T^4R_b^2R_f(1 - R_f) \tag{34}$$

Thus, the number of escaping photons after the v^{th} trajectory is

$$\phi_{esc,v} = \phi_i\big(1 - R_{fe}\big)T^{2v}R_b^vR_f^{v-1}(1 - R_f) \tag{35}$$

From this, the total reflection can be written as

$$\begin{aligned} R_{tot} &= R_{fe} + \frac{\phi_{esc,1}}{\phi_i} + \frac{\phi_{esc,2}}{\phi_i} + \cdots + \frac{\phi_{esc,\infty}}{\phi_i} \\ &= R_{fe} + \big(1 - R_{fe}\big)(1 - R_f)\sum_{v=1}^{\infty} T^{2v}R_b^vR_f^{v-1} \end{aligned} \tag{36}$$

Using the general geometric series form (only valid for $-1 < y < 1$),

$$\sum_{v=0}^{\infty} y^v = \frac{1}{1 - y} \tag{37}$$

the total reflection can be written as

$$R_{tot} = R_{fe} + \big(1 - R_{fe}\big)\big(1 - R_f\big)\frac{TR_b}{1 - T^2R_bR_f} \tag{38}$$

The same procedure can also be used to derive equations for the absorption A, the transmission T, and the generation G. Of course, the approach leading to (38) uses too many simplifications to accurately simulate a real solar cell. Additional aspects such as the angle of incidence need to be added to receive more realistic results. A detailed description of these additional factors will be given in section 3.1.1.

2.4 Semiconductor fundamentals

We generally are interested in how much current a solar cell produces at different working points when it is exposed to light. To describe this behavior, a selection of equations will be used here that are referred to as semiconductor device equations and date back to 1950, when Van Roosbroeck first described them [63, p. 101].

The interactions between these equations are depicted in Fig. 2.8. It schematically shows an arbitrary element of the semiconductor and the processes by which charge carriers are added or deleted from the element. Here G is the profile of charge carriers that are generated inside the element by the absorption of light, U is the recombination of charge carriers and N_{in} and N_{out} are the particle flows into and out of the element.

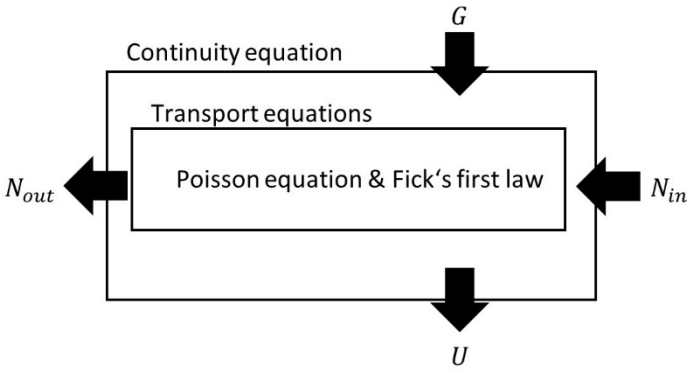

Fig. 2.8: Schematic representation of the physical relations governing the current flow in a semiconductor

Before going into a more detailed explanation of the equations, a general statement is needed to deepen the understanding. It can be said that the transport equations describe the way electrons and holes move inside the semiconductor, while the continuity equation is the bookkeeper of the carriers. It defines how many charge carriers there are for each position and time, including their generation, recombination, and in- and outflows.

The transport equations describe how the movement of the charges (electrons and holes) changes over time and space. There are two different forces acting upon the carriers. One force is caused by the electric fields and produces the so-called drift current, while the other is caused by the gradient of particles that leads to the diffusion current.

The mobility of the electrons μ_n and of the holes μ_p and their corresponding density n_c and p_c are needed to determine the drift current

Drift current:

$$j_n^{drift} = q n_c \mu_n E \tag{39}$$

$$j_p^{drift} = q p_c \mu_p E \tag{40}$$

The determination of the electric fields that lead to the drift current is accomplished with the help of the Poisson equation, which is closely linked to the first of Maxwell's equations (4). It states that the formation of an electric field in a semiconductor depends on the balance between the electron concentration n_c, the hole concentration p_c, the ionized acceptor density N_A^- and the donor atom densities N_D^+.

Poisson equation:

$$\nabla \cdot \vec{\boldsymbol{E}} = -\nabla^2 \varphi = \frac{\rho}{\varepsilon} = \frac{q}{\varepsilon}(p_c - n_c + N_D^+ - N_A^-) \tag{41}$$

Here φ is the electrostatic potential.

The diffusion current is determined by Fick's first law that states that the diffusion current is proportional to the concentration gradient. The corresponding proportionality factor is called the diffusion coefficient D. For the one-dimensional case, electrons and holes are determined thusly:

Diffusion current:

$$j_n^{diff} = qD_n \frac{dn_c}{dx} \tag{42}$$

$$j_p^{diff} = -qD_p \frac{dp_c}{dx} \tag{43}$$

Both the drift and the diffusion current are combined into the transport equation to describe the total current through the device. Assuming that no lateral currents appear, all of the equations can be combined for the case of one dimension, which is the x-dimension here.

Transport equations:

$$j_n = j_n^{drift} + j_n^{diff} = qn\mu_n E + qD_n \frac{dn}{dx} \tag{44}$$

$$j_p = j_p^{drift} + j_p^{diff} = qp\mu_p E - qD_p \frac{dp}{dx} \tag{45}$$

In a solar cell, generation G and recombination U permanently take place in parallel. These two processes may vary over time and along the dimension x as the absorption depth of photons that have different wavelengths varies and likewise the recombination changes, depending on the position. This leads to varying currents that can be described with the help of the continuity equation. In the one-dimensional form, it can be written as

Continuity equation:

$$\frac{dn}{dt} = \frac{1}{q}\frac{dj_n}{dx} - (U - G) \tag{46}$$

$$\frac{dp}{dt} = -\frac{1}{q}\frac{dj_p}{dx} - (U - G) \tag{47}$$

In general, there are two ways to calculate the semiconductor device: Numerically and analytically.

Many physical and engineering problems are so complex that no analytical expression can be obtained. For these cases, numerical simulations are used to describe the behavior of the system. In some cases, the problem can be simplified to the dominant aspects and can then be analytically described. The advantages of such an analytical description are [64]:

- In general, analytical solutions give more insight into the physics of a problem.
- The calculation time is often highly reduced
- The calculations do not suffer from convergence problems

In this thesis, both approaches are used. For the less complex structure of an untextured solar cell, it is possible to determine an analytical expression for the generation profile and the collection of the charge carriers. For cases where textures are involved, which lead to multiple reflections and paths of the photons inside the semiconductor, numerical

simulations are applied to determine the generation profile and to determine the collection properties of the semiconductor. For the latter, the software PC1D is used, which is a numerical semiconductor device simulation tool that is widely used in the photovoltaic research community. The software uses a one-dimensional finite element approach where the semiconductor equations presented above are discretized for every single element and then are numerically solved for certain boundary conditions. A detailed description of this process can be found in [65].

2.4.1 Depletion approximation of a diode in the dark

To describe the approach for an analytical simulation of a solar cell, a simple model is used for the start and then complexity is gradually added to it. The basis for all of the following derivations is the so-called depletion approximation, which helps to reduce the complexity of the simulations significantly by dividing the solar cell into regions with an electric field and those without. In a standard solar cell, the region that has an electric field is the region where the n-doped and the p-doped region of the solar cell come together. Here a p-n-junction is formed, which is also referred to as the depletion region as no free carriers are left due to the recombination of the positive and negative charges in this zone [66]. The regions not included in the depletion region are field free and are referred to as quasi neutral regions (QNR). It is important to note that in reality, especially the emitter, also contains an electric field as the doping is not homogeneous but decreases with the depth due to the application process[5]. However, the depletion approximation gives reasonable results for many analytical investigations.

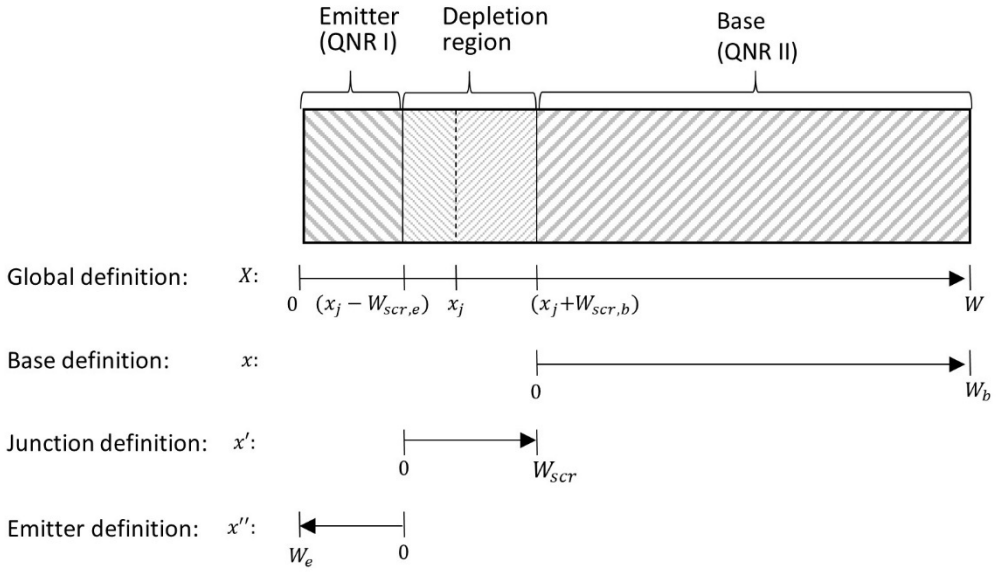

Fig. 2.9: One-dimensional representation of a solar cell and the definition of the different coordinate axes

It is crucial to clearly define the points on the position axis which indicate the separation of the different regions. As the total current is determined by the sum of the individual currents of the three regions (n-region, SCR and p-region), different coordinate systems

[5] The doping profile is often simulated as having a Gaussian profile or an error function profile.

are defined for each of the regions. This extremely simplifies the process of solving for the respective currents. The definitions of the coordinate axis and the position points are given in Fig. 2.9.

The depletion region is separated into an n-side and a p-side region. The corresponding thicknesses $W_{scr,e}$ and $W_{scr,b}$ are dependent on the doping concentrations of donor atoms N_D and the acceptor atoms N_A. The total width of the depletion region W_{scr} is then found by

$$W_{scr} = W_{scr,e} + W_{scr,b} = \sqrt{\frac{2\varepsilon}{q} V_{bi} \left(\frac{1}{N_A} + \frac{1}{N_D} \right)} \tag{48}$$

where ε is the permittivity of the medium (here silicon) and q is the elementary charge. The variable V_{bi} is the built-in voltage, which is the potential difference that arises from the electric field that builds up due to the charges in the depletion region. It can be determined by

$$V_{bi} = \frac{k_B T}{q} \ln \left(\frac{N_A N_D}{n_i^2} \right) \tag{49}$$

where k is the Boltzmann constant, T is the temperature in Kelvin, and n_i is the intrinsic carrier concentration.

When dealing with semiconductor equations, one generally is interested in finding the current voltage characteristics (*I*-*V*-curve or *j*-*V*-curve) of the solar cell, or the equations are used to find the short circuit current I_{sc} or the short circuit current density j_{sc}, where there is no voltage drop over the cell. In both cases, the procedure is comparable even though solving of the equations is always strongly dependent on how the problem is set up and which simplifications are permitted.

The general approach used here is identical to establishing and solving any differential equation. The main steps are illustrated in Fig. 2.10. The approach consists of the identification of the differential equation that describes the problem to be solved. Then, typically the right formulation for the function must be determined that solves the differential equation. To come from the general formulation to this particular one, boundary conditions must be introduced.

To make these steps more clear, the function that describes the electron current collected at the boundary between the base and the depletion region will now be derived. The current that can be collected from the base in the given example is completely driven by diffusion of electrons as these are the minority charge carriers. The holes as majority charge carriers are negligible, as the diffusion current depends on the ratio of newly generated or induced charge carriers to their equilibrium value. As the equilibrium value is very high in a p-doped base, the ratio will always stay very low.

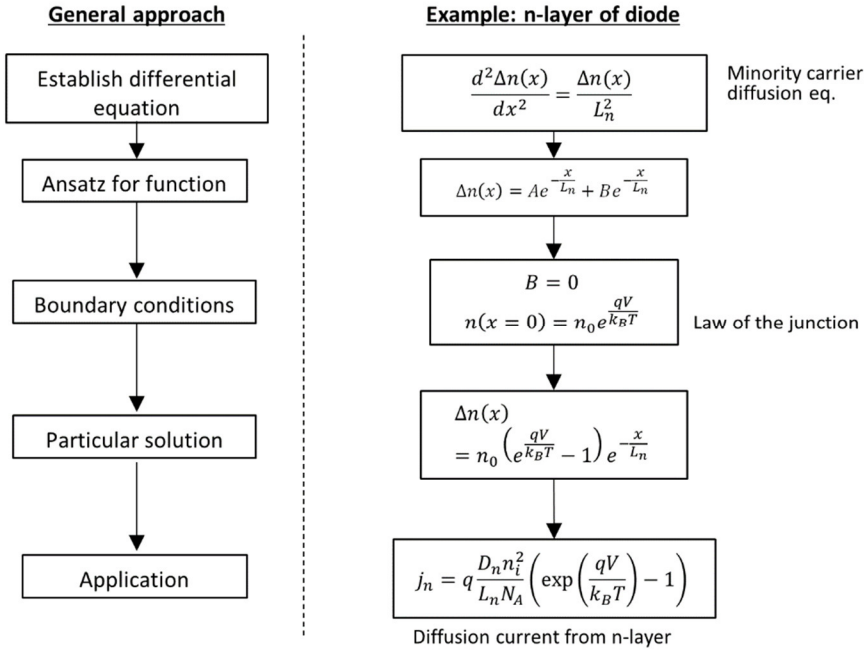

Fig. 2.10: Flow chart for the procedure of setting up and solving a problem that is describable by a differential equation (left: general description, right: exemplary case)

The so-called minority carrier diffusion equation is set up by the combination of the continuity equation (46) and the drift current equation (39). Firstly, the left side of (46) is set to zero as steady state operation is assumed. Secondly, no extra generation process due to light exposure is also assumed. And thirdly, recombination is written in terms of an effective time constant for the electrons τ_n.

$$U_{eff} = \frac{\Delta n}{\tau_n} \tag{50}$$

Then, a new variable L_n is introduced, which is the diffusion length of the electrons inside the n-layer. It is defined as the average distance the minority charge carriers travel before they recombine [57].

$$L_b^2 = D_n \tau_n \tag{51}$$

This leads to a second order differential equation that is referred to as the minority carrier diffusion equation for electrons in the dark. It is important to note that in left hand term of (52) the total carrier concentration $n(x)$ was replaced by the excess carrier concentration $\Delta n(x)$ because of the fact that $n(x) = \Delta n(x) + n_0$ where n_0 is the constant equilibrium carrier concentration and will thus get cancelled out when the derivation of the equation is calculated.

$$\frac{d^2\Delta n(x)}{dx^2} = \frac{\Delta n(x)}{L_b^2} \tag{52}$$

Looking up possible solutions, the following formulation with the constants A and B is found.

$$\Delta n(x) = Ae^{-\frac{x}{L_b}} + Be^{\frac{x}{L_b}} \tag{53}$$

It is evident that B can only be zero as the right hand side would increase to plus or minus infinity for any other constant. To find A, the boundary condition known as the law of the junction is introduced. It provides the carrier concentration at the edge between the base and the depletion region as a function of the applied voltage [67].

$$n(0) = n_0 e^{\frac{qV}{k_B T}} \tag{54}$$

Knowing that $\Delta n(x) = n(x) - n_0$ we can insert (54) into (53) were x is set to 0. Now A can easily be determined. Inserting A back into (53) delivers an expression for Δn that can be tested for correctness by inserting it back into (52).

$$\Delta n(x) = n_0 \left(e^{\frac{qV}{k_B T}} - 1 \right) e^{-\frac{x}{L_b}} \tag{55}$$

This expression can now be used to find the wanted electron current by inserting the term into the diffusion current equation for electrons (42). Evaluating this equation for the coordinate that represents the edge of the depletion region delivers the following expression.

$$j_n = q \frac{D_n n_i^2}{L_b N_A} \left(\exp\left(\frac{qV}{k_B T} \right) - 1 \right) \tag{56}$$

If the same procedure for the derivation of the hole current at the boundary between the emitter and the depletion zone is followed, a similar expression to the one in (56) is obtained. The total current j_{tot} of the diode is then the sum of the hole and the electron current at the depletion zone edges.

$$j_{tot} = j_n + j_p \tag{57}$$

This provides the following expression,

$$j_{tot} = q \left(\frac{D_n n_i^2}{L_b N_A} + \frac{D_p n_i^2}{L_e N_D} \right) \left(\exp\left(\frac{qV}{k_B T} \right) - 1 \right) = j_0 \left(\exp\left(\frac{qV}{k_B T} \right) - 1 \right) \tag{58}$$

where the newly introduced variable j_0 is referred to as the saturation current density [68]. The derived equation describes the characteristic curve of a semiconductor diode (dependency of the current on the voltage) and is therefore called the diode equation. As the detailed description was determined by William B. Shockley, the equation is also referred to as Shockley diode equation [69].

As this simple model of a diode (as well as for a solar cell in the dark) does not fully describe the real performance of such devices, additional factors such as the series resistance R_s, the shunt resistance R_{sh}, and the diode ideality factor m are added to the equation.

For the description of solar cells and photodiodes, an additional term for the generation of charge carriers due to illumination is added to the diode equation, i.e., the j-V-curve in

the dark. The fact that the current in the dark and the current generated by photons (j_{sc}) can be separately treated and subsequently added up is referred to as the superposition principle. Therefore, the equation becomes

$$j_{tot} = j_0 \left(\exp\left(\frac{qV}{k_B T}\right) - 1 \right) + j_{sc} \tag{59}$$

Thus, for the performance of a solar cell, both the light induced current as well as the current voltage characteristics are of high importance.

2.4.2 Short circuit current density of an illuminated solar cell

Using the same procedure as above, the current equations for a solar cell under short circuit conditions will now be derived.

The derivation presented in the following is based on the work of Wen et al. [64], who extended the procedure for the analytical description of the base that was presented by Basore [70] and Brendel et al. [71]. The approach of Wen et al. can easily be transferred to the base leading to a simple analytical description of the solar cell. In section 3.1 a new analytical model is presented that is based on the same approach, however including additional elements such as free carrier absorption (FCA), metallization and diffuse reflection.

A term for the photo generation of charge carriers $G(\lambda, x)$ is now added to the minority carrier diffusion equation derived above (52). This is a function of the light's wavelength and the position x inside the wafer.

$$\frac{d^2 \Delta n(x)}{dx^2} - \frac{\Delta n(x)}{L_b^2} = -\frac{G(\lambda, x)}{D} \tag{60}$$

Before discussing how to calculate a generation profile, another concept for the simplification of the derivation process must be introduced. It is assumed that the principle of superposition holds for this solar cell, i.e., the generation profile can be split into four independent parts for which the current can separately be derived. After determining the four currents, they are simply added up to receive the total current.

Yet the question remains as to why the generation is split into four pieces. The reason is that four different transmission angles are introduced, so that solar cells where the front and the back side are not perfectly parallel can be simulated. The splitting is: 1) First forward pass, 2) First backward pass, 3) All subsequent forward passes, 4.) All subsequent backward passes. The relevant angle definitions are given in Fig. 2.11.

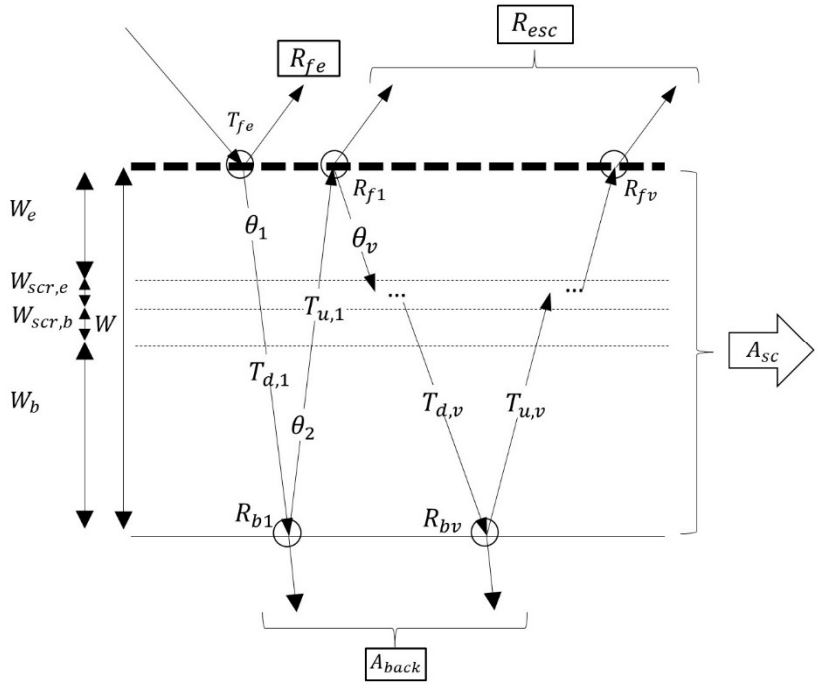

Fig. 2.11: Angle and widths definitions for the simple analytical solar cell model described in this section

The generation is directly linked to the absorption of photons in the semiconductor, as every absorbed photon creates an electron hole pair. Therefore, the Beer-Lambert law (32) is used for the generation profile. To derive it, the absorption at any position x must be calculated. This is nothing else but the change in transmitted photons over the infinitesimal small distance Δx, and thus can be calculated by the derivation of the Beer-Lambert law multiplied by the initial number of photons ϕ_i. For the assumption of an infinitely thick solar cell, the generation can be thusly written as

$$G(\lambda, x) = \phi_i(\lambda)\alpha(\lambda)\exp(-\alpha(\lambda)x) \tag{61}$$

For a more realistic derivation, the fact that the cell has a finite thickness has to be included. Thus, some photons bounce forth and back inside the solar cell.

As mentioned above, the generation is separated into four parts, for which the corresponding current term is separately derived. The generation profile for the first transit of the light through the semiconductor can be written as

$$\begin{aligned} G_{f1,b}(x) &= \phi_i(1 - R_{fe}) \exp\left(-\frac{\alpha\,(W_e + W_{scr})}{cos(\theta_1)}\right) \frac{\alpha}{\cos(\theta_1)} \exp\left(-\frac{\alpha\, x}{\cos(\theta_1)}\right) \\ &= a_b \exp\left(-\frac{\alpha\, x}{\cos(\theta_1)}\right) \end{aligned} \tag{62}$$

where W_e and W_{scr} are the thicknesses of the emitter and the space charge region respectively and a is a variable containing all the constant parameters of the equation, making it much easier to manage the equation in the following derivation steps.

It is worth mentioning that the division through the cosine of the incidence angle can either be interpreted as a correction of the path length or as an adjustment of the absorption coefficient. In the following the second interpretation was chosen, as it combines well with the approach of the one-dimensional semiconductor simulation. Later on, the corrected absorption coefficient will be referred to as the effective absorption coefficient.

$$\alpha'(\theta) = \frac{\alpha}{\cos(\theta)} \tag{63}$$

The generation profile for the first back pass can be written as

$$\begin{aligned} G_{b1,b}(\lambda, x) &= \phi_i\big(1 - R_{fe}\big) T_{d,1} R_{b1} \frac{\alpha}{\cos(\theta_2)} \exp\left(-\frac{\alpha\,(W_b - x)}{\cos(\theta_2)}\right) \\ &= b_b \exp\left(-\frac{\alpha\,(W - x)}{\cos(\theta_2)}\right) \end{aligned} \tag{64}$$

where the transmission of the first forward pass is calculated by $T_{d,1} = \exp(-\alpha'(\theta_1)\, W)$. As this backward generation profile has its highest value at the back side of the solar cell, the depth component in the second exponential term is becoming zero for $x = W_b$, which is the thickness of the base region.

For the derivation of the generation profiles of all subsequent forward passes and backward passes, the same procedure must be applied as was presented in the end of section 2.3. To keep track of the parts that the geometric series consists of, it is helpful to write down the exponents of the elements in form of a table as it was done in Table 2.1 for the forward passes in a solar cell with parallel surfaces.

Table 2.1: List of exponents of the elements of the equations associated to the first and up to the v^{th} forward pass of the photons through the base of a wafer with plane parallel front and rear side.

$G_{fv,b}(\lambda, x) =$	$\phi_{f,b}^{init}$	$T_{d,v}$	$T_{u,v}$	R_{bv}	R_{fv}	$\frac{\alpha}{\cos(\theta_v)} \exp\left(-\frac{\alpha x}{\cos(\theta_v)}\right)$
1. forward pass	1	0	0	0	0	1
2. forward pass	1	1	1	1	1	1
3. forward pass	1	2	2	2	2	1
…						
$(v+1)^{th}$ forward pass	1	v	v	v	v	1

Here $\phi_{f,b}^{init}$ is the initial photon density after the first forward and backward pass, which is easily determined to be

$$\phi_{f,b}^{init} = \phi_i\big(1 - R_{fe}\big) T_{d,1} R_{b1} T_{u,1} R_{f1} \exp\left(\frac{-\alpha\,(W_e + W_{scr})}{\cos(\theta_v)}\right) \tag{65}$$

where the transmission of the first backward pass is calculated by $T_{u,1} = \exp(-\alpha'(\theta_2)\, W)$.

With this, the generation profile of all subsequent forward passes can be written as

$$G_{fv,b}(\lambda,x)=\frac{\phi_{f,b}^{init}\frac{\alpha}{\cos(\theta_v)}\exp\left(-\frac{\alpha x}{\cos(\theta_v)}\right)}{1-T_{d,v}T_{u,v}R_{bv}R_{fv}}=c_b\ \exp\left(-\frac{\alpha x}{\cos(\theta_v)}\right) \tag{66}$$

where the downward transmission $T_{d,v}$ and the upward transmission are identical for this example and can be determined by

$$T_{d,v}=T_{u,v}=\exp(-\alpha'(\theta_v)W) \tag{67}$$

Following the same procedure as before, the generation profile created by all subsequent backward passes can be written as

$$G_{bv,b}(\lambda,x)=\frac{\phi_{b,b}^{init}\frac{\alpha}{\cos(\theta_v)}\exp\left(-\frac{\alpha\,(W_b-x)}{\cos(\theta_v)}\right)}{1-T_{d,v}T_{u,v}R_{bv}R_{fv}}=d_b\ \exp\left(-\frac{\alpha\,(W_b-x)}{\cos(\theta_v)}\right) \tag{68}$$

The corresponding table and the equation for the initial photon density $\phi_{b,b}^{init}$ can be found in Table A.1 of the appendix.

Now the current densities resulting from each of the four generation profiles need to be determined and then the contributions are added up to receive the total current density of the base region. As the procedure is equivalent for all four of them, only the current equation for the first of the four generation terms will be derived.

The starting point for the derivation is the minority carrier diffusion equation (60), which includes the term for the generation profile.

The general solution for the minority carrier function is then

$$\Delta n_{b1}(x)=A\cosh\left(-\frac{x}{L_b}\right)+B\sinh\left(-\frac{x}{L_b}\right)+\frac{a_b\cos(\theta_1)^2\exp\left(-\frac{\alpha\,x}{cos(\theta_1)}\right)L_b^2}{D_n(\cos(\theta_1)^2-\alpha^2L_b^2)} \tag{69}$$

Now two boundary conditions are applied. The first is for the connecting point to the space charge region, where the last time the law of the junction was applied. Since the short circuit current is being solved for and there is no applied voltage over the junction, it can be assumed that all the charge carriers that are created in the junction region are immediately removed from it, leaving no charge carrier behind. This leads to the condition that $\Delta n_{b1}(0)=0$.

The second condition is related to the surface recombination velocity S_n at the back side of the device [72].

$$S_n\Delta n=-D_n\frac{d\Delta n}{dx} \tag{70}$$

With the help of these two boundary conditions, the constants A and B can be determined and the function for the minority charge carriers in the base $\Delta n_{b1}(x)$ can be determined.

To find the current, this equation must be inserted into the diffusion current equation (41), which is then evaluated for the position $x = 0$, which is the edge to the space charge region, where all the charges of the base are collected. This results in the current equation for the generation due to the first forward pass.

$$j_{a,b} = q a_b \frac{L_b}{\alpha'(\theta_1)^2 L_b^2 - 1} \left(\alpha'(\theta_1) L_b - \frac{\sinh\left(\frac{W}{L_b}\right) + \frac{S_n L_b}{D_n} \cosh\left(\frac{W}{L_b}\right) - \left(\frac{S_n L_b}{D_n} - \alpha'(\theta_1) L_b\right) \exp(-\alpha'(\theta_1) W)}{\cosh\left(\frac{W}{L_b}\right) + \frac{S_n L_b}{D_n} \sinh\left(\frac{W}{L_b}\right)} \right) \tag{71}$$

To give this equation more meaning, the fact that the number of absorbed photons can be expressed as

$$f_{a,b} = a_b \frac{1 - \exp(-\alpha'(\theta_1) W_b)}{\alpha'(\theta_1)} \tag{72}$$

is used. Now the current density can be written as the product of the number of absorbed photons $f_{a,b}$ and the probability that the generated charge carriers are collected $\eta_{forward,b}$.

$$j_{a,b} = q\, f_{a,b}\, \eta_{forward,b} \tag{73}$$

From equations (71) to (73) the collection probability is found to be

$$\eta_{forward,b}(\theta_1) = \frac{\alpha'(\theta_1)\, L_b}{(\alpha'(\theta_1)^2 L_b^2 - 1)(1 - \exp(-\alpha'(\theta_1) W_b))} \left(\alpha'(\theta_1) L_b - \frac{\sinh\left(\frac{W_b}{L_b}\right) + \frac{S_n L_b}{D_n} \cosh\left(\frac{W_b}{L_b}\right) - \left(\frac{S_n L_b}{D_n} - \alpha'(\theta_1) L_b\right) \exp(-\alpha'(\theta_1) W_b)}{\cosh\left(\frac{W_b}{L_b}\right) + \frac{S_n L_b}{D_n} \sinh\left(\frac{W_b}{L_b}\right)} \right) \tag{74}$$

For the first and subsequent backward passes, the collection probability will have a slightly different form, as a result of the definition of this coordinate system. The backward collection probability can be written as

$$\eta_{back,b}(\theta_2) = \frac{\alpha'(\theta_2)\, L_b}{(\alpha'(\theta_2)^2 L_b^2 - 1)(1 - \exp(-\alpha'(\theta_2) W_b))} \left(\alpha'(\theta_2) L_b \exp(-\alpha'(\theta_2) W_b) - \frac{\left(\sinh\left(\frac{W_b}{L_b}\right) + \frac{S_n L_b}{D_n} \cosh\left(\frac{W_b}{L_b}\right)\right) \exp(-\alpha'(\theta_2) W_b) - \left(\frac{S_n L_b}{D_n} - \alpha'(\theta_2) L_b\right)}{\cosh\left(\frac{W_b}{L_b}\right) + \frac{S_n L_b}{D_n} \sinh\left(\frac{W_b}{L_b}\right)} \right) \tag{75}$$

Adding up the four separate currents of the base region to the total base current results in the following equation

$$\begin{aligned} j_b = {} & q\, f_{a,b}\, \eta_{forward,b}(\theta_1) \\ & + q\, f_{b,b}\, \eta_{back,b}(\theta_2) \\ & + q\, f_{c,b}\, \eta_{forward,b}(\theta_n) \\ & + q\, f_{d,b}\, \eta_{back,b}(\theta_n) \end{aligned} \tag{76}$$

For the emitter region, the same splitting into four separate currents can be applied. As a different coordinate system was chosen; thus, flipping the direction of the solution, the collection probabilities must also be flipped, resulting in the following equation for the emitter current

$$\begin{aligned} j_e = {} & q\, f_{a,e}\, \eta_{back,e}(\theta_1) \\ & + q\, f_{b,e}\, \eta_{forward,e}(\theta_2) \\ & + q\, f_{c,e}\, \eta_{back,e}(\theta_n) \\ & + q\, f_{d,e}\, \eta_{forward,e}(\theta_n) \end{aligned} \tag{77}$$

The detailed expressions for the number of absorbed photons $f_{a,e}\ to\ f_{d,e}$ can be found in (A.3) to (A.6) in the appendix and the collection probabilities in the emitter $\eta_{back,e}$ and $\eta_{forward,e}$ are given in (A.7)and (A.8).

To derive the current from the space charge region, the assumption was made that all of the created charge carriers are collected due to the strong electric field that accelerates them directly to the contacts. This leads to the following expression

$$\begin{aligned} j_{scr} = {} & q\, f_{a,scr} \\ & + q\, f_{b,scr} \\ & + q\, f_{c,scr} \\ & + q\, f_{d,scr} \end{aligned} \tag{78}$$

The equations for the number of absorbed photons inside the space charge region also can be obtained from (A.9) to (A.12) in the appendix.

2.5 External and internal quantum efficiency

The external quantum efficiency EQE is equivalent to the spectral response SR of the solar cell or module. The SR determines how much current a solar cell produces per area, when one Watt of monochromatic radiation is incident on the same area. This is why the unit of the SR is [A/W] after the area is canceled out.

$$SR = \frac{j_{sc}}{I_i} \tag{79}$$

In contrast, the EQE is the ratio of charge carriers, which can be collected from a specific area, to the number of photons that all have the same wavelength that are incident on the same area. So the only difference is that the current density needs to be transformed in number of charge carriers and the intensity of the light to the number of photons ϕ_i. The number of collected charges includes holes as well as electrons and can be calculated

knowing the generation profile $G(x)$ and the collection probability η_c at all x-positions. The effect of photon recycling is included in the value of η_c [73].

$$EQE = SR\frac{hc_0}{q\lambda} = \frac{j_{sc}}{q\phi_i} = \frac{\int_0^W G(x)\eta_c(x)dx}{\phi_i} \tag{80}$$

In $G(x)$, all of the optical properties of the device are included except for the photon recycling mentioned above. The optical effects are namely the reflection at all interfaces, the transmission through the device, and the absorption inside the device. The absorption can be distinguished into the desired absorption inside the semiconductor and the parasitic absorption that will be described in detail in section 5. The collection probability includes the mechanisms that lead to the recombination of charge carriers. These are the radiative recombination, the Auger recombination, the Shockley-Read-Hall (SRH) recombination and the surface recombination [67].

As the SR as well as the EQE generally refer to short circuit conditions, it is not possible to derive any information about the shunt resistance R_{sh}, the series resistance R_s, or other aspects of the j-V-characteristics from the measurement.

For this thesis, special measurement equipment was used to determine the SR at different incident angles. This setup will be explained in detail in section 4.1.

The internal quantum efficiency IQE was introduced to be able to separate the optical and the electrical effects governing the performance of solar cells. It tells how many of the photons absorbed in the semiconductor are actually collected to serve as current in the external circuit. The theoretical IQE can be determined from the EQE with

$$IQE = \frac{\int_0^W G(x)\eta_c(x)dx}{\phi_i A_{sc}} = \frac{EQE}{A_{sc}} \tag{81}$$

Where A_{sc} is the absorption in the semiconductor. The standard measurement procedure for the determination of the IQE is to measure the reflection of the device R and to subsequently calculate the absorption in the semiconductor by $A = 1 - R$, so the IQE determined by measurements is

$$IQE_{meas} = IQE^* = \frac{EQE}{1-R} = \frac{EQE}{A_{sc} + A_{Pa}} \tag{82}$$

The variable IQE^* was introduced to distinguish the two different theoretical definitions of the IQE. While the first definition (81) is the correct one, the definition in (82) is necessary to be able to compare simulated to measured values. The definitions are different because the denominators of (81) and (82) are different, which can be expressed in the following equation.

$$A_{sc} \neq 1 - R = A_{sc} + A_{Pa} \tag{83}$$

To transform IQE to IQE^*, it is obligatory to know the parasitic absorption. The transformation is than found by equalizing the EQE in equation (81) and (82).

$$IQE^* = IQE \frac{A_{sc}}{A_{sc} + A_{Pa}} \tag{84}$$

If the IQE of a solar cell or module is given several information on its electrical performance can be drawn from it. The effective diffusion length L_{eff} can be determined as described in [70] and with some further investigations the base diffusion length L_b and the rear surface recombination velocity S_r can be found using the approach of Spiegel et al. [74]. But the accuracy of the determination of these parameters is strongly depending on the type of cell under investigation [75].

2.6 Textured surfaces

The surface morphology of all interfaces in a solar module is of particular importance for the optical as well as for the electrical performance of the module. The simplest device consists of parallel interfaces between the different materials that form the solar module. Even though the first solar modules were constructed in this manner, the interfaces in reality are never totally flat. Every surface has a certain share of unevenness and thus a share of Lambertian scattering meaning that some of the reflected and transmitted photons are randomly deviating from their specular path. Thus, for optical simulations it often makes sense to implement a Lambertian share for reflection and transmission at the different surfaces that are involved. Nevertheless, for carefully smoothened surfaces, e.g., those formed by etching and polishing, an ideal flatness can be assumed.

To evaluate the actual flatness of a surface different measurement techniques can be applied. Using an integrating sphere a so called haze factor can be determined that is defined as the ratio of diffuse reflection to the total incident light [76]. Using more elaborated techniques it is possible to additionally evaluate the spectral and angular distribution of the reflected light. The results of such a measurement are referred to as bidirectional reflection distribution function (BRDF) [77].

However, for most of the interfaces, it is not desired for them to be completely flat. At the interfaces there are often textures implemented to reduce the reflection on the one hand and to increase the path length of the photons through the semiconductor for that the absorption probability is increased on the other hand.

Generally, surface morphologies can be separated in three groups, which are rough surfaces, nano textures, and macro textures. A rough surface is defined as a surface which randomizes the path of reflected and transmitted photons. However, randomization does not need to be completely Lambertian, but can in reality be limited to a certain direction. The direction of the dispersion cone often is located around the reflected and the transmitted beam. A common model for the simulation of such a distribution is given by the Phong model [78], which was originally derived for computer graphics to make the diffuse reflection on a surface look more realistic [79]. At this point it it should also be mentioned

that Eli Yablonovich [80] showed that the maximum average pathlength that can be achieved is $4n^2d$ when Lambertian surfaces are applied. But it could also be shown, that this so called Yablonovich-limit can be overcome using dedicated light-trapping schemes [81–83].

Nano texturing is the term for repeating structures that are small in size and spacing as compared to the wavelengths of light. Very low reflection values can be achieved by structures such as "Black silicon" [84, 85], "Moth eye" [86], effective medium approaches [87] and many others [25].

This thesis focuses on macro structures, which are huge compared to the wavelengths of light. Generally these textures can be implemented on the top surface of the encapsulant (glass or transparent synthetic foils) and on the top and bottom surfaces of the semiconductor layer. In standard solar modules, it is common to only apply a texture on the top surface of the solar cell. The purpose of this texturing is mainly to reduce reflection, since a photon that at the first hit does not enter the semiconductor at the phase of the texture and thus is reflected, will at least have one more chance to enter at the neighboring texture. This process is referred to as external light trapping.

The standard process to implement textures in a monocrystalline solar cell was described in section 2.1. But it is also possible to realize regular patterns onto monocrystalline solar cells with more advanced techniques, such as controlled etching with masking, mechanical grooving, or laser applications [88, 89]. However, these techniques require more time, effort, and money and are not compatible with the standard etching process.

Using the same processes that are applied on the front surface, the back side of solar cells can also be textured to increase the optical path length of the light trough the semiconductor.

Texturing the front side encapsulant provides the same external light trapping effect as described above, but an additional effect is relevant. This effect strongly reduces the Fresnel reflection as is depicted in Fig. 2.12. The mechanism of this reduction is explained for a two dimensional structure and thus in a simplified way. On a standard low iron solar glass with a refractive index of 1.5, an angle of incidence of 60° causes a reflection of 8.9 %. When comparing the same light beam at the textured surface, an effective incidence angle in relation to the pyramidal phase of 15° results. At these comparably low angles of incidence, the reflection is reduced to 4 % [23].

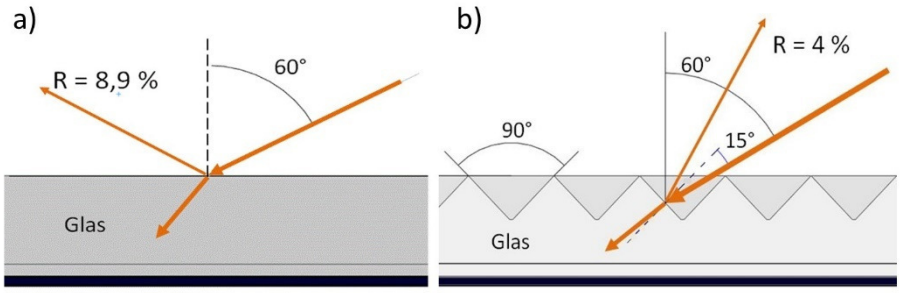

Fig. 2.12: Exemplary comparison of the angle of incidence on a flat glass in a) to the effective angle of incidence on a textured surface in b)

A texture such as the one in Fig. 2.12 *b)* will drastically lower the reflection for angles of incidence > 50° and thus will keep the IAM closer to unity.

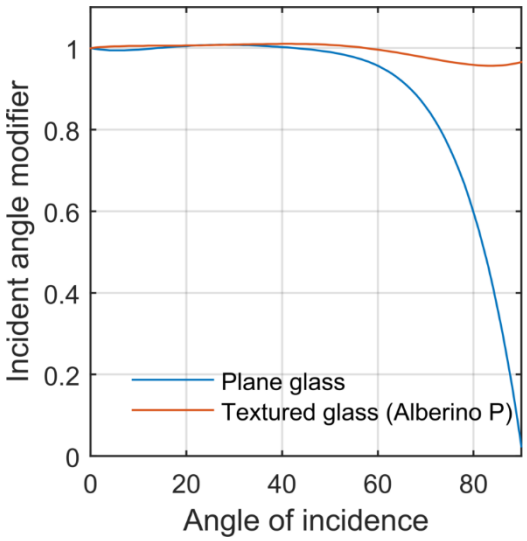

Fig. 2.13: Incidence angle modifiers (IAM) of a planar and a textured surface (Alberino P®)

In Fig. 2.13 the measured IAM functions of a plane glass and a commercially available textured front side glass sheet (Alberino P® produced by Saint Gobain) are presented. The measurements were performed indoors using a solar module flasher and were subsequently fitted using a fifth-degree polynomial function. The texture of Alberino P is best described as inverted and rounded pyramid. This corresponds to texture 4 in the collection of the most important textures that is given in Table 2.2. These texture types were identified within the research project ESOSWA that was conducted at the Cologne University of Applied Sciences [90].

Table 2.2: Overview of textures which can in principle be realized in the front side encapsulant and the front side or the back side of the solar cell

Texture 1	Texture 2	Texture 3	Texture 4
Pyramid 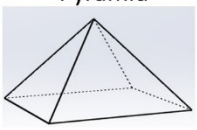	Inverted Pyramid 	Rounded Pyramid 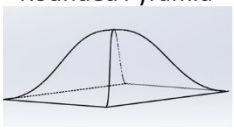	Inv. Rounded Pyramid 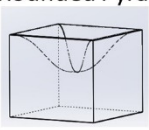

Texture 5	Texture 6	Texture 7	Texture 8
Groove/Shed 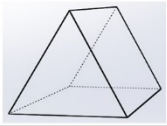	Rounded Groove 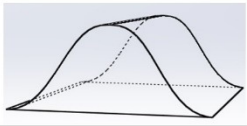	Flat Groove 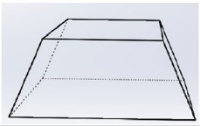	Corner Cubes 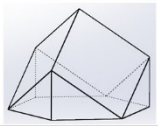

Texture 9	Texture 10	Texture 11
Cylinder 	Inv. Cylinder 	Hemisphere 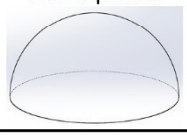

Texture 12	Texture 13	Texture 14
Inv. Hemisphere 	Cone 	Inv. Cone 

Texture 15	Texture 16	Texture 17
Rounded Cone 	Inv. Rounded Cone 	Isotexture 

The impact of implementing textures into the front side encapsulation of a solar module on the energy yield can be huge, depending on the orientation of the module. Using the above described model for the yield prediction, a comparison between a standard module and a module with rounded inverted pyramids (texture 4), which have the IAM depicted in Fig. 2.13, reveals an advantage of the texture for all module orientations. The increase in energy yield can be seen in Fig. 2.14, where the highest values are given for an orientation of the module to the north. Here of course, the total yield is comparably low to the orientation giving the highest yield values, which is a southern orientation and a tilt angle of 45° (+/- 5°). The yield increase due to the textures for this orientation is much less, but is still at about 3.2 %. Orientations to the east or to the west show gains of about 4% to

5% and a facade integrated module (tilt angle 90°) facing to the south has a 4.6 % higher energy yield.

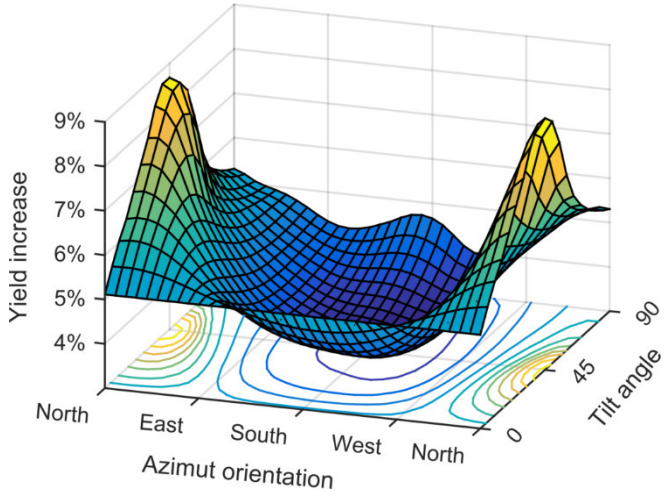

Fig. 2.14: Additional energy yield by the implementation of an inverted rounded pyramid texture in the front side encapsulant (Alberino P®) compared to a planar standard front side encapsulant for different module orientations

Even though these gains caused by the implementation of a texture are of high interest for the photovoltaic community, another aspect of the properties of a front side texturing will be investigated here. This aspect is the change of the transmission angle due to the texture. In Fig. 2.15 an example for a light ray with an incident angle of 45° and a pyramidal groove with a pyramidal base angle of 45° is shown.

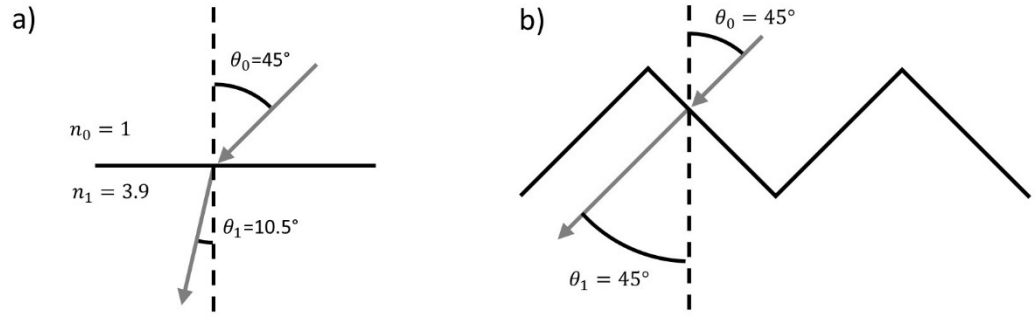

Fig. 2.15: Simplified light propagation at the interface of two media. The first medium has a refractive index of 1 as it is the case for vacuum and the second 3.9, representing a silicon solar cell. Example a) shows a planar surface and b) a groove texture with a base angle of 45°.

In this example, the angle of transmission in (a) is 17° lower than in example (b). This influences the absorption in the encapsulation medium, the reflection on the top of the semiconductor, and the transmission angle inside the semiconductor. These aspects will be investigated in detail to understand their influence on the energy yield and if necessary to propose an optimized anti-reflection coating or pyramid structure on top of the semiconductor.

2.7 The opto-electronic reciprocity relation of photovoltaic devices

The opto-electronic reciprocity relation of photovoltaic devices, was rigorously proven by Uwe Rau in 2007 [91], which is the reason why it is also referred to as Rau's Reciprocity Relation (RRR). It became a powerful tool for researchers in the field of photovoltaic and light emitting diodes (LED). Using the reciprocity relation allowed the development of many specific examination methods such as band-gap imaging [92], photocurrent collection efficiency mapping [93], front surface field determination [94] and others [95–98].

In this thesis the utilization of the reciprocity relation for the determination of angular spectral response curves from electroluminescence measurements is elaborated. For this purpose, the basic principles behind the theory will be outlined in the following.

Many processes can be found in physics where the direction of a process (e.g., energy flow, particle flow) is connected to its inverse process by a reciprocity relation, i.e., both processes are linked by the nature of the system. Thus, knowing the one process and the reciprocity relation, makes it possible to derive the physics of the reverse process. To clarify this, the optical reciprocity will be presented here as an example. It is best concluded in the sentence: "If I can see you, you can see me". This means that if two points A and B in medium 1 and 2 are connected by the same photon path, they will have the same reflectivity at the interface. While these are just two tiny elements of the optical reciprocity relation, the detailed analysis leads to the famous Kirchhoff's radiation law, which states that the directional spectral emissivity ε equals the directional spectral absorptivity α [99].

The proof of Kirchhoff's law and of many other reciprocity relations can be achieved by using the principle of detailed balance. It can be seen as a conservation law on a microscopic scale. Imagine two energy states 1 and 2 and a number of particles moving between them. In thermal equilibrium, they will reach a stadium in which at every state a mean number of particles Z_1 and Z_2 is to be found. There will still be a transition between the states with a certain probability t_{12} and t_{21} with a particle transition rate of r_{12} and r_{21}. For that, the balance between the two states is conserved so that the rates of transition need to compensate each other [100]. This can be expressed as

$$Z_1 t_{12} = r_{12} = r_{21} = Z_2 t_{21} \tag{85}$$

If the number of states is increased, the direct transitions from one state to another is not the only possible path, but many intermediate steps are possible making it increasingly difficult to calculate the transition probabilities and the rates of transition. The principle of detailed balance is the proof that it is not necessary to calculate all possible paths between two states, since these states can be regarded as disconnected to the others. The rate of transition from one state to the other still is completely balanced by its inverse process.

In 1961, William Shockley and Hans J. Queisser also used the detailed balance principle in their famous paper "Detailed Balance Limit of Efficiency of p-n Junction Solar Cells" to derive the maximum conversion efficiency for a one junction silicon solar cell, the so-called Shockley-Queisser-limit (SQ-limit). At the core of the derivation stands the fact that

detailed balance dictates that the solar cell must radiate back to the sun [101]. As this mechanism is fundamental, it cannot be avoided. To find the maximum efficiency, the maximized power output is divided by the total solar power,

$$\eta_{SQ} = \frac{\max\{qV(\phi_i - \phi_{em}(V))\}}{\sigma_{SB} T_S^4} \tag{86}$$

where ϕ_i is the total number of photons that are all absorbed for every photon energy greater than the band gap energy (E_g), and ϕ_{em} is the number of photons that are forced to be radiated back to the sun. The temperature of the sun T_s is about 5758 K[6] and is multiplied by the Stefan-Boltzmann-constant σ_{SB}.

The reciprocity relation derived by Uwe Rau applies the same detailed balance relation that the SQ-theory uses to real solar cells, by adding the aspect of electronic transport to it. For the electronic transport another reciprocity relation was already derived in 1985 by C. Donolato, which is referred to as Donolato's reciprocity theorem. It states that the collection probability η_c at a position x of a semiconductor equals the ratio of the accessible charges Δn at position x to the injected charges at the junction n_{jct}, which is located at $x = 0$ [102]

$$\eta_c(x) = \frac{\Delta n(x)}{n_{jct}} \tag{87}$$

The mathematical derivations of the general Optoelectronic Reciprocity, which were mainly done by Uwe Rau are given in [91, 99, 100, 103, 104]. It is not in the scope of this work to rigorously derive the reciprocity relation, but instead a more intuitive access will be given to the topic.

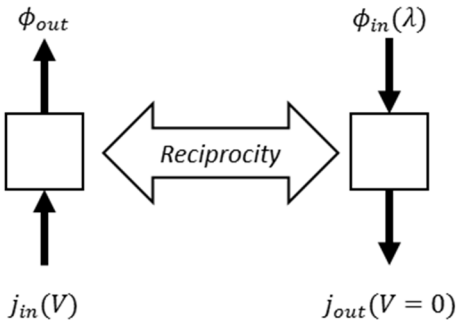

Fig. 2.16: Symbolic representation of the reciprocity relation between the light emission and the light absorption of different current operation points

The link that the reciprocity relation gives is depicted in Fig. 2.16. There is a fundamental connection between the two operations "current at a certain voltage in and photons out" and "photons in and short circuit current out".

For the basic understanding of the reciprocity relation it is helpful to start with the fact that a solar cell is a 'gray body'. This means that the black body spectrum ϕ_{bb} which would

[6] In the original paper, Shockley and Queisser set the sun's temperature to 6000 K.

be emitted by a black body in thermal equilibrium is reduced by the actual spectral emissivity ε_g of the material under investigation. The same is true for the absorption where the spectral absorptivity of the gray body is given by α_g. Using Kirchhoff's law and the fact that the photon fluxes of the emission ϕ_{em} and absorption ϕ_{abs} need to be identical in thermal equilibrium, the following equation is true.

$$\phi_{abs}(x) = \alpha_g(x)\phi_{bb} = \varepsilon_g(x)\phi_{bb} = \phi_{em}(x) \tag{88}$$

The black body radiation ϕ_{bb} can be written as [99].

$$\phi_{bb} = \frac{2\pi \mathrm{E}^2}{h^3 c_0^2} f_{BE} \tag{89}$$

where h is Planck's constant and c is the speed of light. The term in the equation that is containing the fraction describes the density of states in a cavity in which photons can exist, while f_{BE} is the Bose-Einstein distribution function, that describes the distribution of photons as a function of energy. It is given by [57]

$$f_{BE} = \frac{1}{\exp\left(\frac{\mathrm{E}}{k_B T}\right) - 1} \tag{90}$$

When a constant voltage V is applied to the semiconductor it is reaching a steady state condition after a period of time. The spectrum which is emitted then is the black body radiation modified by the splitting of the quasi-Fermi energies of the conduction and the valence band ($E_{FC} - E_{FV}$). This Energy difference is equal to qV which is subtracted from the Energy in the Bose-Einstein distribution function (90). This modification of Planck's law was first proven by Lasher and Stern [105] and later generalized by Würfel [106] and Würfel et al. [107]. If the nominator in the exponential term is much larger than $k_B T$, the Boltzmann approximation can be applied, which leads to a simple exponential factor.

$$\varepsilon_g(x)\phi_{bb}(V) = \varepsilon_g(x)\phi_{bb} \exp\left(\frac{qV}{k_B T}\right) \tag{91}$$

where q is the elementary charge, k equals the Boltzmann constant and T is the temperature of the device under investigation. While the emission is increased by the applied voltage the absorption of the device stays the same as in thermal equilibrium such that the net photon flux $\Delta\phi_{em}$ is the difference between the radiation and the absorption.

$$\Delta\phi_{em}(x) = \varepsilon_g(x)\phi_{bb}(V) - \alpha_g(x)\phi_{bb} = \alpha_g(x)\phi_{bb}\left(\exp\left(\frac{qV}{k_B T}\right) - 1\right) \tag{92}$$

The emissivity $\varepsilon_g(x)$ vanished from the right-hand term of the equation because of Kirchhoff's law, which states $\varepsilon_g(x) = \alpha_g(x)$. It is important to note that (92) is only correct for the case of a semiconductor with no other recombination mechanisms except for radiative recombination. To generalize (92) further the collection probability $\eta_c(x)$ from Onsager's reciprocity relation (87) is multiplied. As the EQE at the location x equals the product of η_c and α_g at the same location, we can write

$$\begin{aligned}\Delta\phi_{em}(V,x) &= \eta_c(x)\alpha_g(x)\phi_{bb}\left(\exp\left(\frac{qV}{k_BT}\right)-1\right)\\ &= EQE(x)\phi_{bb}\left(\exp\left(\frac{qV}{k_BT}\right)-1\right)\end{aligned} \tag{93}$$

As the total emission which is actually measured is the sum the emissions of all locations, we need to define the total EQE as the integrated value of all $EQE(x)$ over all locations x in the device, thus we receive

$$\Delta\phi_{em}(V) = EQE\phi_{bb}\left(\exp\left(\frac{qV}{k_BT}\right)-1\right) \tag{94}$$

which is the form of the reciprocity relation as it is given in [99].

3 Simulating the angle of incidence effects

As described above, there are several effects that determine the transformation of the EQE when the AOI is varied from the normal. To separate the impact of each of these parameters, it is meaningful to simulate the solar cell under changing angles of incidence. Two different approaches were used to simulate the angle dependence of solar cells and modules in this thesis. While the first approach is an analytical model, which is mainly applicable to planar solar cells, the second is a numerical ray tracing model, which is capable of simulating different kinds of textures and material stacked above each other. The two approaches are described in detail in the following.

3.1 Analytical approach

In general, analytical models can have some fundamental advantages compared to purely numerical simulations. When the physical problem is well described, they offer in-depth insight into its properties. The influence of specific contributory factors may thus be separated. Furthermore, the calculation time can often be reduced significantly while the calculations do not suffer from convergence problems [64]. These are some of the reasons why a new analytical model was developed for this thesis.

3.1.1 Analytical model for the optical performance of a planar solar cell

At the end of section 2.3, the mathematical procedure was presented to set up infinite converging sums and to subsequently find a simplified form. In section 2.4.2, the same procedure was applied to derive the four generation profiles for the first down- and upward pass and all subsequent down- and upward passes of the light. The optical model that was used for this derivation is similar to an approach that was presented in 1993 by Paul Basore [70]. It is still widely used in the PV community and is also implemented in the semiconductor simulation tool PC1D [78]. The model of Basore was then extended by Rolf Brendel for an advanced IQE analysis procedure [71]. Many other researchers chose a similar approach to derive the generation profile, which was subsequently used to solve the semiconductor equations that were presented in section 2.4 [64, 71, 108–110].

These optical models essentially all use similar basic simplifications. One of which is the assumption that the light is either completely direct or diffuse on its path through the cell. A common strategy is to assume a specular light pass for the first forward and backward trajectory through the slab and to assume for all the subsequent passes fully diffuse light [64, 70, 111]. For the direct light, the reflection and refraction paths are assumed to be fully specular while the implementation for the diffuse light is done by assuming a mean angle of 60° for the trajectory, which was derived by Campbell et al. [112].

Another basic assumption is that there is one specific back surface reflection value for direct and diffuse light. This value is regularly used to evaluate the quality of a back surface reflector without differing between the direct and the diffuse share of the reflection [78, 113]. However, it should always be kept in mind that the back surface reflection value used

by the model is a fitting parameter without concrete physical meaning. Especially the angular behavior of the internal reflection is not appropriately represented by this assumption. Thus, a good measurement fitting at perpendicular incidences might be given, whereas the simulation for low angles of incidence might not fit the measured values.

This is the reason why a novel optical model was developed in this thesis that includes the fact that at every surface intersection only a certain share of light is scattered and transformed into diffuse light. This aspect of the model will be explained in detail in this section. Yet, first some other aspects of the model will be clarified. The equations (B.1) to (B.40) in the appendix provide all relevant calculations steps for the model.

The optical performance of a solar cell is influenced by many different factors. To obtain an analytical description, the selection of the most important of these factors is required. Regarding most of the solar cells, which are currently sold on the marked, the texturing of the cell's surface is one of the most important factors concerning their optical performance. At the same time, the complexity, which is added due to the fact that the light is split up into multiple refracted light passes at every intersection that has a textured surface, is overwhelming. This is also the reason why no geometrical model that is capable of analytically describing the pathways created by a surface of regular pyramids had been developed up to now, not to mention more complex textures as the ones given in Table 2.2.

To keep the complexity manageable and to investigate the optical factors apart from textured surfaces, a solar cell with planar interfaces was chosen for the derivation of the optical model. Nonetheless it should be mentioned that the simulation of a textured solar cell can be emulated afterwards by the introduction of effective angles and by the modification of reflection parameters. The adaption of the analytical model of a planar cell to textured surfaces has been shown by several authors [64, 71, 114].

To derive the optical model used in this thesis, three different layers with infinite width and parallel surfaces that are stacked above each other can be imagined. Each of these layers consists of a certain material whose optical properties are given by the complex refractive index. In comparison to the Basore model, some novel core elements were added. These are listed below and subsequently described in detail.

- Reflection and absorption by contact grid
- Application of a thin coating on the surfaces
- Free carrier absorption
- Diffuse light reflection and transmission

In principle, the contact grid consists of contact fingers, busbars, pads, and ribbons. For the case of a standard solar cell, it is sufficient to model the fingers and the busbars. If the measurements at the cell under investigation are performed with a light spot that is located between the busbars, these can be neglected in the simulation.

When the grid is laminated into an encapsulation material such as glass, the reflection properties of the ribbons and the fingers can have a significant impact on the performance of the solar module [27, 115]. As the analytical model does not take encapsulation into account; only the geometrical share of the metallization is considered. For the contact fingers, this share is calculated by

$$M_{fi} = \frac{p_{bb} \cdot w_{fi}}{\left((p_{bb} + w_{bb})(p_{fi} + w_{fi})\right)} \tag{95}$$

where w_{fi} and w_{bb} are the widths of the contact fingers and the busbars respectively and p_{fi} and p_{bb} are the pitches between these. These respective values can be determined by reflected light microscope imaging. The widths of the fingers and busbars can be exemplarily seen in Fig. 3.1.

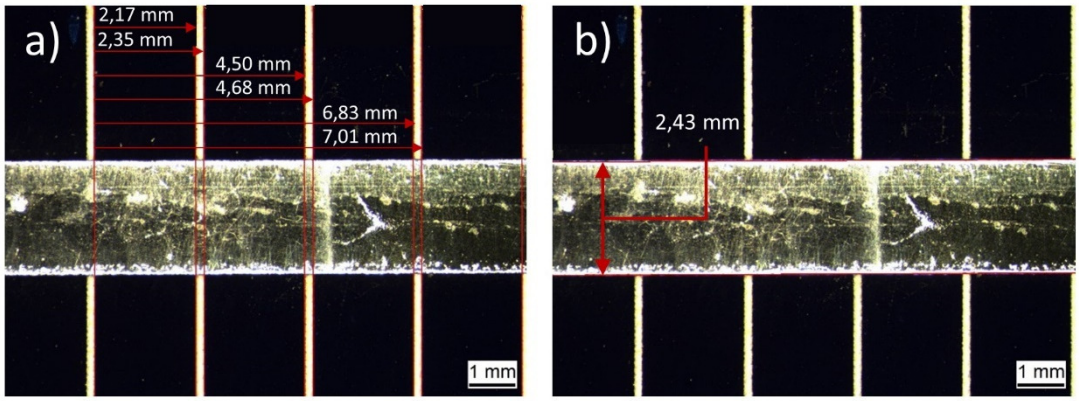

Fig. 3.1: Width determination of the contact fingers and busbars with the help of a calibrated reflected light microscope. The values given in a) are indicating the distance between the red lines resulting in a finger width of 180 µm. In b) the width of the corresponding busbar is displayed.

The share of the busbar area can be determined by

$$M_{bb} = \frac{w_{bb}}{w_{bb} + p_{bb}}. \tag{96}$$

Thus, the share of the cell area is

$$M_{cell} = 1 - M_{bb} - M_{fi}. \tag{97}$$

These shares are subsequently used in the determination of the surface reflection and transmission.

The theoretical background for the determination of the physics of an anti-reflection coating was given in section 2.3. The most commonly used anti-reflection coating on top of a silicon solar cell is silicon nitride (SiN_x) as it has good surface passivation properties and a complex refractive index which is controllable by the composition of the two elements [116]. The film is mainly deposited by means of plasma enhanced chemical vapor deposition (PECVD) and its thickness is optimized for a wavelength of 600 nm, which is where

the maximum of the $AM1.5$ solar spectrum lies, and for the case of encapsulation in embedding material such as glass and EVA [25].

When the exact composition and thickness of the SiN_x layer is not known as it was the case for the planar cell under investigation, it is necessary to have the material data of different material compositions to find the best fit for the conducted reflection measurements. The optical parameters of many different SiN_x compositions and all the other materials used in this thesis were taken from the PV Lighthouse Refractive Index Library [117] where the corresponding authors who made the data available are indicated as well.

Another physical aspect, which was added to make the optical model more realistic, is the free carrier absorption (FCA). The absorption coefficient of silicon does not include the effect of free carrier absorption, which refers to an excitation of electrons inside the conduction band or holes inside the valence band and a subsequent transformation of this additional energy to heat [118]. The parametric equation proposed by Baker-Finch et al. was used [119] to determine the absorption coefficients for the free carrier absorption in the different regions of the solar cell.

$$\alpha_{FCA} = C \cdot N_x \cdot \lambda^{\gamma} \tag{98}$$

Here N_x is the concentration of free carriers generally equal to the acceptor doping concentration N_A or the donor doping concentration N_D. For the carrier concentrations in the depletion region $N_{D,scr}$, the average value of the carrier concentrations in emitter $N_{D,e}$ and the intrinsic carrier concentration n_i was chosen.

$$N_{D,scr} = (N_{D,e} + n_i)/2 \tag{99}$$

The parameters C and γ are given by the values in Table 3.1.

Table 3.1: Parameters for the determination of the free carrier absorption coefficient in the n- and p-region [119].

	***p*-Si**	***n*-Si**
$\boldsymbol{C}$	$(1.8 \pm 0.83) \cdot 10^{-9}$	$(1.68 \pm 0.62) \cdot 10^{-6}$
$\boldsymbol{\gamma}$	2.18 ± 0.01	2.88 ± 0.08
$\boldsymbol{\lambda}$ $[\boldsymbol{nm}]$	$1000 - 1500$	

To find the total absorption inside a material, the absorption coefficients may be added up and can then be inserted into the Beer-Lambert-Law (32); thus, the absorption of light traversing a silicon solar cell can be written as

$$A_{tot} = 1 - \exp\left(-\frac{(\alpha + \alpha_{FCA,e})W_e}{cos(\theta_1)}\right)\exp\left(-\frac{(\alpha + \alpha_{FCA,scr})W_{scr}}{cos(\theta_1)}\right)\exp\left(-\frac{(\alpha + \alpha_{FCA,b})W_b}{cos(\theta_1)}\right) \tag{100}$$

To find the number of absorbed photons inside the semiconductor without the FCA we need to determine the corresponding share p_{sc}.

$$\phi_{abs,sc} = \frac{A_{sc}}{A_{tot}} \phi_{abs,tot} = p_{sc} \phi_{abs,tot} \tag{101}$$

where $\phi_{abs,tot}$ is the total number of absorbed photons. Writing down the exact equation for p_{sc} we find

$$p_{sc} = \frac{1 - \exp\left(-\frac{\alpha \mathrm{W}}{cos(\theta_1)}\right)}{1 - \exp\left(-\frac{\left(\alpha + \alpha_{FCA,e}\right)W_e}{cos(\theta_1)}\right) \exp\left(-\frac{\left(\alpha + \alpha_{FCA,scr}\right)W_{scr}}{cos(\theta_1)}\right) \exp\left(-\frac{\left(\alpha + \alpha_{FCA,b}\right)W_b}{cos(\theta_1)}\right)} \tag{102}$$

The exponentials can be transformed using the series expansion of the form [120, p. 115]

$$\exp(x) = \sum_{l=0}^{\infty} \frac{x^l}{l!} = 1 + x + \frac{x^2}{2!} + \frac{x^3}{3!} + \cdots \tag{103}$$

As for the wavelengths > 1000nm the product αW is small it is sufficient to use the first two terms of (103). With some further simplifications the share of absorption in the semiconductor p_{sc} can be written as follows

$$p_{sc} \approx \frac{\alpha W}{\left(\alpha + \alpha_{FCA,e}\right)W_e + \left(\alpha + \alpha_{FCA,scr}\right)W_{scr} + \left(\alpha + \alpha_{FCA,b}\right)W_b} \tag{104}$$

A similar expression can be derived for the share of free carrier absorption p_{FCA} and is presented in the appendix (B.12).

Another element, which was included to improve the optical model, is the effect of light scattering. If only specular reflection is assumed, a strong overestimation of the escape reflection results even for planar slabs of solar cells. This is due to the fact that it is virtually impossible to create a perfectly planar surface. There is always a share of photons that are scattered in a direction that deviates from the specular one. This diffuse reflection, which is also denoted as the haze factor, is described in more detail in section 2.6.

A central element of the optical model is the new approach concerning the diffuse share of light inside the solar cell. As described above, most of the commonly used optical models assume the radiation either to be completely direct or totally diffuse. To receive a physically more realistic model, the specular and the diffuse radiation were separated. While the share of direct radiation follows the simple rules of specular reflection, for the diffuse radiation a new procedure had to be developed.

For the derivation of the diffuse light equations, a double series of sums is needed where the outer sum determines the maximum of the inner sum.

$$\sum_{l=0}^{\infty} \sum_{v=0}^{l} x^v y^l = \frac{1}{(y-1)(xy-1)} \tag{105}$$

Such double sum converges if the elements x and y are smaller than one [120, p. 118]. The necessity of the double series comes from the fact that the diffuse light may be specular for many bounces before becoming diffuse, so that all the intersections need to be

considered as a source of diffuse light. Another important aspect for this series is that light, which is diffuse once will stay so forever.

The detailed derivation of the optical model can be found in appendix B. To keep track of the exponents involved these are written down in a tabulated form making it much easier to oversee the corresponding derivations. The resulting equations for the direct and diffuse reflection ($R_{esc,dir}, R_{esc,diff}$), absorption ($A_{dir}, A_{diff}$), and transmission ($T_{tot,dir}, T_{tot,diff}$) are

Reflection:

$$R_{esc,dir} = \frac{T_{fe}(1-h_f)(1-h_b)T^2R_bT_f}{1-(1-h_f)(1-h_b)T^2R_bR_f} \tag{106}$$

$$R_{esc,diff} = \frac{T_{fe}(h_fT_{diff}^2R_{b,d} + h_b(1-h_f)T_{diff}TR_b)T_{f,d}}{(T_{diff}^2R_{b,d}R_{f,d}-1)\left((1-h_b)(1-h_f)T^2R_bR_f-1\right)} \tag{107}$$

Absorption:

$$A_{dir} = \frac{T_{fe}(1-h_f)(1+(1-h_b)TR_b)(1-T)}{1-(1-h_f)(1-h_b)T^2R_bR_f} \tag{108}$$

$$A_{diff} = \frac{T_{fe}\left(h_f + h_b(1-h_f)T_{diff}TR_{f,d}R_b + h_fT_{diff}R_{b,d} + h_b(1-h_f)TR_b\right)(1-T_{diff})}{(T_{diff}^2R_{b,d}R_{f,d}-1)\left((1-h_f)(1-h_b)T^2R_bR_f-1\right)} \tag{109}$$

Transmission:

$$T_{tot,dir} = \frac{T_{fe}(1-h_f)T(1-R_b)}{1-(1-h_f)(1-h_b)T^2R_bR_f} \tag{110}$$

$$T_{tot,diff} = \frac{T_{fe}(h_fT_{diff} + h_b(1-h_f)T_{diff}^2TR_{f,d}R_b)(1-R_{b,d})}{(T_{diff}^2R_{b,d}R_{f,d}-1)\left((1-h_b)(1-h_f)T^2R_bR_f-1\right)} \tag{111}$$

where the parameters h_f and h_b are the haze factors of the front and the back surface which are 0 for complete specular reflection and unity for complete diffuse reflection. R_f and R_b are the reflection values for the specular light at the inner front and back surface while $R_{f,d}$ and $R_{b,d}$ are the corresponding values for the diffuse radiation. The parameters T_{fn} and $T_{fn,d}$ are the transmissivities of the front surface for specular and diffuse light. The parameters are schematically depicted in Fig. 3.2. The parameters T and T_{diff} are the transmission values for the specular and the diffuse light respectively and are defined as follows.

$$T = \exp\left(-(\alpha' + \alpha'_{FCA,e})W_e\right)\exp\left(-(\alpha' + \alpha'_{FCA,scr})W_{scr}\right)\exp\left(-(\alpha' + \alpha'_{FCA,b})W_b\right) \tag{112}$$

$$T_{diff} = \exp\left(-(2\alpha + 2\alpha_{FCA,e})W_e\right)\exp\left(-(2\alpha + 2\alpha_{FCA,scr})W_{scr}\right)\exp\left(-(2\alpha + 2\alpha_{FCA,b})W_b\right) \tag{113}$$

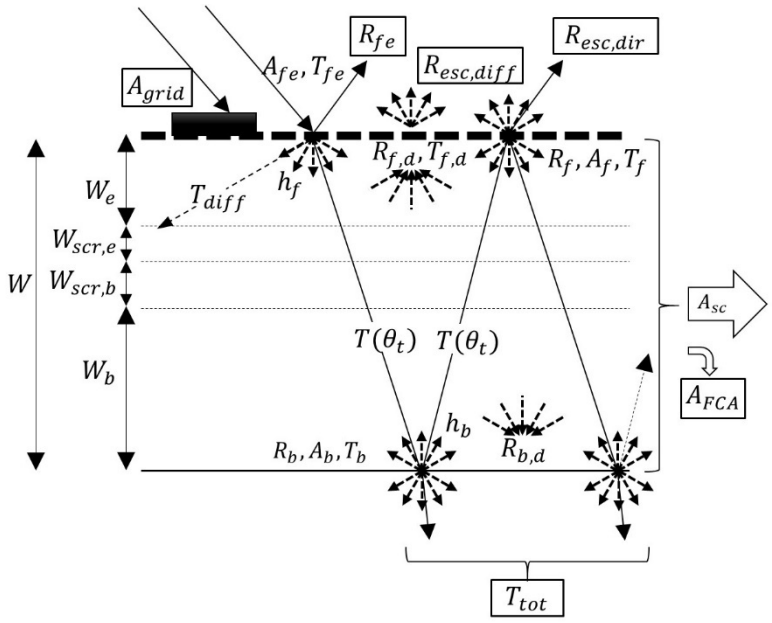

Fig. 3.2: Schematic representation of the optical model separating the diffuse and the direct light passes.

This optical model has the great advantage that it directly reflects the physical mechanisms of reflection inside a slab with the only assumption that diffuse scattering processes are completely Lambertian. To fit a measured reflection curve, 15 different parameters need to be determined (4 x grid size, 4 x material parameter, 2 x thicknesses, angle of incidence, $R_{b,d}$, $R_{f,d}$, h_b, and h_f). The parameters for the grid, the material, the thicknesses and the angle of incidence are found quite easily, so that only the four last parameters need to be determined.

The diffuse reflectivity at the rear and the front side is assumed to be the integral of the reflectivity values at all possible incident angles. The corresponding numerical method to evaluate this integral is given in Appendix C. Knowing the diffuse reflectivity values only two free parameters are left, which are the haze factors of the back and the front side h_b and h_f.

3.1.2 Analytical model for the generation profile and the current

To determine the spectral response of a solar cell, the number of electron-hole-pairs that are created by the absorption of photons need to be known for every position inside the solar cell. This so-called generation profile is completely determined by the optical performance of the solar cell and it is directly linked to the absorption inside the cell.

To determine the generation profile for all semiconductor regions (emitter, space charge region and base) in just one equation, it is helpful to define four cumulative emission spectra, which can be interpreted as the sum of all photons emitted from one surface at a time. These spectra are the cumulative direct forward emission $\hat{\phi}_a$, the cumulative direct backward emission $\hat{\phi}_b$, the cumulative diffuse forward emission $\hat{\phi}_c$, and the cumulative

diffuse backward emission $\hat{\phi}_d$. The equations for these four cumulative emission spectra can be derived by rearranging (B.45), (B.46), (B.50) and (B.53) in the appendix.

$$\hat{\phi}_a = \phi_i \frac{T_{fe}(1-h_f)}{\left(1-\left(1-h_f\right)(1-h_b)T^2R_bR_f\right)} \tag{114}$$

$$\hat{\phi}_b = \phi_i \frac{T_{fe}\left(1-h_f\right)(1-h_b)TR_b}{\left(1-\left(1-h_f\right)(1-h_b)T^2R_bR_f\right)} \tag{115}$$

$$\hat{\phi}_c = \phi_i \frac{T_{fe}\left(h_f+h_b\left(1-h_f\right)T_{diff}TR_{f,d}R_b\right)}{\left(T_{diff}^2R_{b,d}R_{f,d}-1\right)\left(\left(1-h_f\right)(1-h_b)T^2R_bR_f-1\right)} \tag{116}$$

$$\hat{\phi}_d = \phi_i \frac{T_{fe}\left(h_fT_{diff}R_{b,d}+d_{rel,b}\left(1-h_f\right)TR_b\right)}{\left(T_{diff}^2R_{b,d}R_{f,d}-1\right)\left(\left(1-h_f\right)(1-h_b)T^2R_bR_f-1\right)} \tag{117}$$

The generation profile for the entire cell thickness W can now be calculated as the sum of the direct and the diffuse generation using the standard generation formula given in (61) and the depth X from the coordinate definition in *Fig. 2.9*,

$$\begin{aligned} G(\lambda,x) = {} & \alpha' \cdot \left(\hat{\phi}_a \cdot \exp(\alpha' X) + \hat{\phi}_b \cdot \exp(\alpha'(W-X))\right) \\ & + 2\alpha \cdot \left(\hat{\phi}_c \cdot \exp(2\alpha X) + \hat{\phi}_d \cdot \exp\left(2\alpha(W-X)\right)\right) \end{aligned} \tag{118}$$

where α' is the effective absorption coefficient (63) and the factor 2 in front of α stems from the fact that $1/\cos(60°) = 2$, which describes the diffuse path of the photons through the material.

For the calculation of the short circuit current density contribution of every region in the cell, this generation profile needs to be split up into the individual components for every region. Furthermore, an additional factor is needed that takes care of the transmission before the photons reach the dedicated region. This transmission factor is indicated with the symbol T and a superscript of + or – indicating the forward and backward direction.

Using the coordinate definition of the different regions (*Fig. 2.9*), the following generation profiles are obtained,

$$\begin{aligned} G_e = {} & \hat{\phi}_a \cdot T_{e,s}^{+} \cdot \alpha' \exp\left(-\alpha'(W_e - x'')\right) \\ & + \hat{\phi}_b \cdot T_{e,s}^{-} \cdot \alpha' \exp(-\alpha' x'') \\ & + \hat{\phi}_c \cdot T_{e,d}^{+} \cdot 2\alpha \exp(-2\alpha(W_e - x'')) \\ & + \hat{\phi}_d \cdot T_{e,d}^{-} \cdot 2\alpha \exp(-2\alpha x'') \end{aligned} \tag{119}$$

$$\begin{aligned} G_{scr} = {} & \hat{\phi}_a \cdot T_{scr,s}^{+} \cdot \alpha' \exp(-\alpha' x') \\ & + \hat{\phi}_b \cdot T_{scr,s}^{-} \cdot \alpha' \exp(-\alpha'(W_{scr} - x')) \\ & + \hat{\phi}_c \cdot T_{scr,d}^{+} \cdot 2\alpha \exp(-2\alpha x') \\ & + \hat{\phi}_d \cdot T_{scr,d}^{-} \cdot 2\alpha \exp(-2\alpha(W_{scr} - x')) \end{aligned} \tag{120}$$

$$\begin{aligned} G_b = {} & \hat{\phi}_a \cdot T_{b,s}^{+} \cdot \alpha' \exp(-\alpha' x) \\ & + \hat{\phi}_b \cdot T_{b,s}^{-} \cdot \alpha' \exp(-\alpha'(W_b - x)) \\ & + \hat{\phi}_c \cdot T_{b,d}^{+} \cdot 2\alpha \exp(-2\alpha x) \\ & + \hat{\phi}_d \cdot T_{b,d}^{-} \cdot 2\alpha \exp(-2\alpha(W_b - x)) \end{aligned} \tag{121}$$

with the related transmission factors.

$$T_{e,s}^{+} = 1 \tag{122}$$
$$T_{e,s}^{-} = \exp\left(-\left(\alpha' + \alpha'_{FCA,b}\right)W_b\right)\exp\left(-\left(\alpha' + \alpha'_{FCA,scr}\right)W_{scr}\right) \tag{123}$$
$$T_{e,d}^{+} = 1 \tag{124}$$
$$T_{e,d}^{-} = \exp\left(-\left(2\alpha + 2\alpha_{FCA,b}\right)W_b\right)\exp\left(-\left(2\alpha + 2\alpha_{FCA,scr}\right)W_{scr}\right) \tag{125}$$

$$T_{scr,s}^{+} = \exp\left(-\left(\alpha' + \alpha'_{FCA,e}\right)W_e\right) \tag{126}$$
$$T_{scr,s}^{-} = \exp\left(-\left(\alpha' + \alpha'_{FCA,b}\right)W_b\right) \tag{127}$$
$$T_{scr,d}^{+} = \exp\left(-\left(2\alpha + 2\alpha_{FCA,e}\right)W_e\right) \tag{128}$$
$$T_{scr,d}^{-} = \exp\left(-\left(2\alpha + 2\alpha_{FCA,b}\right)W_b\right) \tag{129}$$

$$T_{b,s}^{+} = \exp\left(-\left(\alpha' + \alpha'_{FCA,e}\right)W_e\right)\exp\left(-\left(\alpha' + \alpha'_{FCA,scr}\right)W_{scr}\right) \tag{130}$$
$$T_{b,s}^{-} = 1 \tag{131}$$
$$T_{b,d}^{+} = \exp\left(-\left(2\alpha + 2\alpha_{FCA,e}\right)W_e\right)\exp\left(-\left(2\alpha + 2\alpha_{FCA,scr}\right)W_{scr}\right) \tag{132}$$
$$T_{b,d}^{-} = 1 \tag{133}$$

Now the same approach was applied for the electrical model, that is presented in detail in section 2.4.2. Even though the model for the generation profiles is different now, the procedure to set up and solve the differential equations is the same, as only the constants change their values. Thus, for the current contribution of the different regions, the following can be written

$$\begin{aligned} j_e = {} & p_{sc} q \\ & \cdot \left(\hat{\phi}_a T_{e,s}^{+}(1 - \exp(-\alpha' W_e))\eta_{back,e}(\theta)\right. \\ & + \hat{\phi}_b T_{e,s}^{-}\left(1 - \exp(-\alpha' W_e)\right)\eta_{forward,e}(\theta) \\ & + \hat{\phi}_c T_{e,d}^{+}(1 - \exp(-2\alpha W_e))\eta_{back,e}(60°) \\ & \left. + \hat{\phi}_d T_{e,d}^{-}\left(1 - \exp(-2\alpha W_e)\right)\eta_{forward,e}\left(60°\right)\right) \end{aligned} \tag{134}$$

$$\begin{aligned} j_{scr} = {} & p_{Sc} q \\ & \cdot \left(\hat{\phi}_a T_{scr,s}^{+}(1 - \exp(-\alpha' W_{scr}))\right. \\ & + \hat{\phi}_b T_{scr,s}^{-}(1 - \exp(-\alpha' W_{scr})) \\ & + \hat{\phi}_c T_{scr,d}^{+}(1 - \exp(-\alpha' W_{scr})) \\ & \left. + \hat{\phi}_d T_{scr,d}^{-}(1 - \exp(-\alpha' W_{scr}))\right) \end{aligned} \tag{135}$$

$$\begin{aligned} j_b = {} & p_{sc} q \\ & \cdot \left(\hat{\phi}_a T_{b,s}^{+}\left(1 - \exp(-\alpha' W_b)\right)\eta_{forward,b}(\theta)\right. \\ & + \hat{\phi}_b T_{b,s}^{-}\left(1 - \exp(-\alpha' W_b)\right)\eta_{back,b}(\theta) \\ & + \hat{\phi}_c T_{b,d}^{+}\left(1 - \exp(-2\alpha W_b)\right)\eta_{forward,b}(60°) \\ & \left. + \hat{\phi}_d T_{b,d}^{-}\left(1 - \exp(-2\alpha W_b)\right)\eta_{back,b}\left(60°\right)\right) \end{aligned} \tag{136}$$

3.1.3 Testing the analytical model

To check the internal consistency of the optical model, all individual processes need to be summed up to see if it results in unity.

$$R_{ext} + R_{esc} + A_{met} + A_{AR} + A_{si} + A_{FCA} + A_{back} = 1 \tag{137}$$

If this is not the case, the scripting of the formulas need to be checked. Plotting all the processes over the wavelength leads to a good overview of the individual contributions involved in the optical behavior of the solar cell (Fig. 3.3).

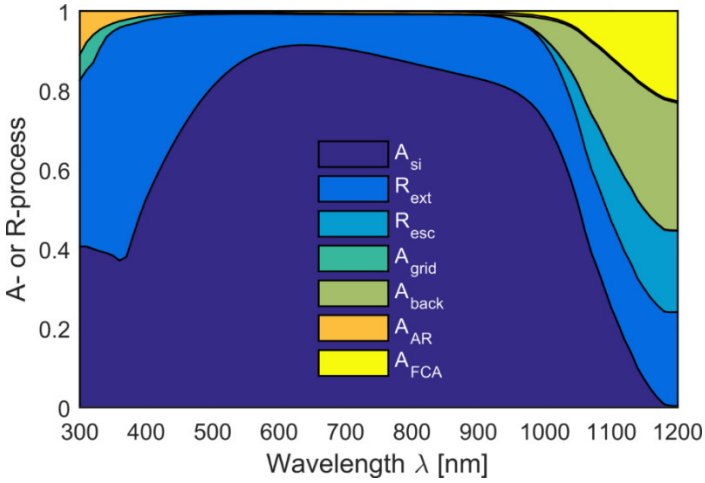

Fig. 3.3: Reflection and absorption processes of a planar silicon solar cell determined by the analytical model presented in this section.

To evaluate the correctness of the analytical model, the total reflection curves at two different angles (8° and 70°) are compared to the curves found with the help of the ray tracing tool SMARTI, which was also developed in the frame of this thesis and which will be presented in detail in the next section.

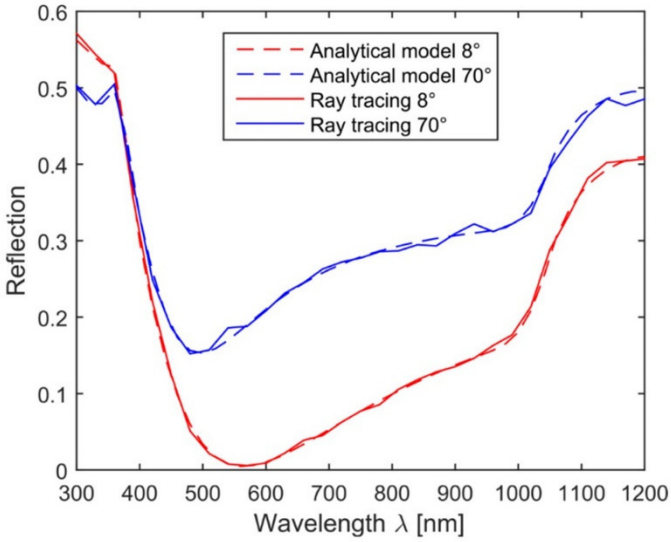

Fig. 3.4: Comparing results for the reflection on a planar solar cell of the analytical model to the results of a ray tracing simulation (5000 rays/wavelength) for the incident angles of 8° and 70°

A comparison of the two approaches is shown in Fig. 3.4. It can be seen that the course of the analytical model fits very well with the course of the values simulated with the ray tracing tool.

To evaluate the electrical model, which was described above, the EQE determined with the analytical model was compared to the one found with the software tool PC1D. For this, a generation profile for the specific wavelength was created with the optical model described above, which is subsequently imported into PC1D to determine the short circuit current for this wavelength leading to the spectral response curve.

PC1D is a simulation tool commonly used in the photovoltaic community. It was written by Paul A. Basore and Donald A. Clugston [121] and is available under the GNU general public license. Additional functionality such as the inclusion of Fermi-Dirac statistics [122] has been added in the meantime and additional software such as a batch generator [123] and a command line version of the software are available. The software uses a one-dimensional Finite-Element Method (FEM) approach in which the cell is discretized in a number of elements for each of which the differential equations are solved in a coupled manner until the conditions at the boundaries of the cell are fulfilled. A detailed description of the math behind the FEM can be found in [65].

In Fig. 3.5, the IQE curves that were determined by the analytical as well as with the numerical tool PC1D are presented for the incident angles of 8° and 70°. The curves found by the different methods are almost identical.

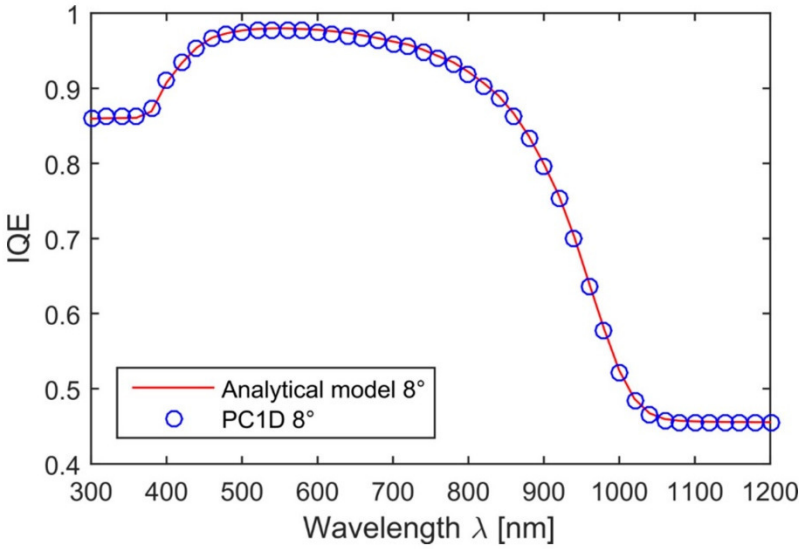

Fig. 3.5: Comparison of the IQE curves generated by the analytical model and by PC1D using the same generation profiles

3.2 Numerical approach

The analytical model described above has a low time consumption. Therefore, it is possible to run many batches where specific parameters are gradually modified, so that optimization procedures can be performed on these parameters. The disadvantage of the analytical

model is that it is developed for planar surfaces and it is thus not suitable for the simulation of textured surfaces. As basically all solar cells that are sold on the market today have textured surfaces, it is crucial to correctly simulate these.

To illustrate the complexity that needs to be handled when textured surfaces are involved, it is very instructive to investigate the possible light passes that may occur when a random pyramidal texture with a base angle of 54.74° is applied to the surface of a solar cell. The possible light passes for the reflected rays were simulated by OPAL 2 [124] and are listed in Table 3.2.

Table 3.2: Light paths on a cell surface of random upright pyramids simulated with OPAL 2 [124]. The numbers in the second row are indicating the intersection numbers 1 to 5. Four different facets are existing for the pyramidal texture.

Path	**Facet**					**Angle of intersection (°)**					**Exit**
Fraction	**1**	**2**	**3**	**4**	**5**	**1**	**2**	**3**	**4**	**5**	**Angle**
0.6834	1	3				54.7	15.8				38.9
0.186	1	2	3			54.7	78.9	33.5			31.6
0.0583	1	2	4	3		54.7	78.9	71.3	51.7		12.8
0.0374	1	2	4			54.7	78.9	71.3			75
0.0324	1	3	1			54.7	15.8	86.3			31.6
0.0014	1	2	4	2	3	54.7	78.9	71.3	88.8	52.7	10.4
0.001	1	2	4	2		54.7	78.9	71.3	88.8		73.5

Knowing that every angle of intersection that is unique results in one refraction path, nine transmission paths are found in total for this example. If the cell has a planar back side, the next intersection will be one with the textured surface from inside after one pass through the cell. Here each of the nine transmission paths will again be split into many different paths. The number of paths is dependent on the angle of incidence on the now inverted pyramids. If a mean number of eight new transmission paths is assumed, a total number of $9 \cdot 8 = 72$ transmission paths is resulting after the first internal front side reflection. After three complete passes, which is very common for photons with wavelengths greater than 1040 nm, a total number of $9 * 8^3 = 4608$ different transition paths is reached. However, despite this large number, this does not necessarily mean that we find all angles equally distributed as would be the case for Lambertian scattering. The number of light paths involved will be even higher, if more than surface is textured or the base of texture is not a square but another geometric form.

The common approach to meet this complexity is to use a ray tracing algorithm, which is based on the creation of random numbers. Many different ray tracing tools are available for the simulation of solar cells. But most of them are restricted in use by one or multiple constraints. Most of the tools that can be bought on the market are very costly and they are often restricted in the choice of input or output parameters. Other tools are known from scientific publications, but they are property of specific research institutes and thus not freely available [125, 126]. Some of the most common ray tracing tools in the PV research community are listed in Table B.8 in the appendix.

Mainly driven by the need for transparency and flexibility in choice of input and output parameter, a ray tracing software was developed in the course of this thesis. The software was developed using the programming language MATLAB® (Matrix Laboratory), which is sold and supported by the company MathWorks[7]. This ray tracing software will be referred to as SMARTI (Simple MATLAB Ray Tracing Implementation) in the following. The central elements of the software are described in the following section.

3.2.1 Monte Carlo Ray tracing

Ray tracing algorithms are of particular interest for engineers and scientists working on realistic image processing. Rendering static images or moving scenes is mainly done by ray tracing because no other computational technic leads to a more realistic appearance [127]. Even though for image processing some additional features are applied (rasterization, shading, anti-aliasing …) and the starting as well as the detection objects differ (in computer graphics, rays generally leave from every pixel leading to the light sources, which is referred to as backward ray tracing) [128], the basic principles that are used in computer graphics also apply to photovoltaic ray tracing.

In the Monte Carlo method, a numerical approach is defined that uses a random number generator for the determination of a physical process, which itself is determined by random processes or is of such high complexity that analytical procedures are not feasible [129]. The method of Monte Carlo modeling is widely used in many research fields and is, e.g., an essential component of experimental particle physics at CERN (European Organization for Nuclear Research) [130].

In the case of ray tracing, the application of the Monte Carlo method is also referred to as Monte-Carlo particle tracing [129], where many rays that represent photons are individually traced until they interact with a surface. Here, depending on the number that is calculated by the random number generator, a decision is made as to what is happening to the ray. In solar cell ray tracing tools, the decision will generally be if it is absorbed, reflected, or transmitted. Additional decisions such as if the reflection will be specular or diffuse can be taken using the same random number or by the creation of another one.

It would be computationally very costly to create a model involving all the pyramidal structures of a solar cell and subsequently perform a ray tracing study on the model, which is why a so-called unit cell approach is mainly used for the simulation. The unit cell is a cuboid (or any other volume element that can be laterally ordered without a gap) that incorporates all the structures that repeat periodically. If a ray hits the side of the unit cell, it will receive a new starting point which is situated to the opposite of where the side was intersected. The direction of the ray is conserved. Like this, by using symmetry, an infinite array of pyramids can be modeled with little effort. In Fig. 3.6 an example is plotted for a

[7] It is worth mentioning that Octave and Scilab are two software packages under the GNU General Public License that are based on a language similar to the MATLAB programming language; thus, in most cases, MATLAB code can be executed with these software packages.

SMARTI simulation of a solar module with textured front side encapsulant and a textured solar cell (layer thicknesses are not to scale).

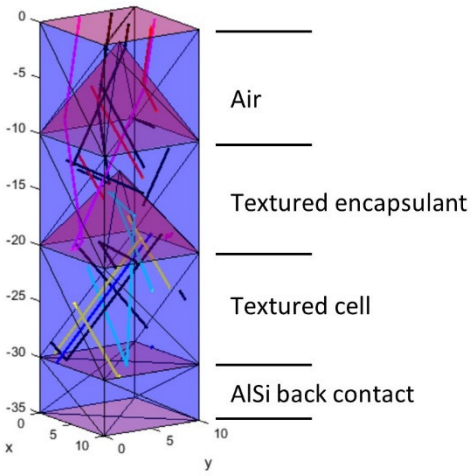

Fig. 3.6: Unit cell of a solar module simulated in SMARTI consisting of 4 layers (air, encapsulant, Si, AlSi). A pyramidal texture is added to the top of the second and the third layer. The heights of the individual layers are not to scale.

The central element of the software is a function representing any layer that can be implemented in a solar module. The function input consists of a number of input parameters, which define the properties of the layer. These parameters are

- The position of the layer in the layer stack
- The material and thickness of the AR coating if one is applied
- The geometry of the layer including its size and the texture on its bottom
- The material the layer is consisting of
- The grid consisting of contact fingers and busbars if one is applied
- The number of maximum bounces the rays may perform inside the layer
- Plotting parameters for a graphical representation of the rays inside the stack of layers

Apart from this of course, the numbers of rays that enter the layer from the top and from the bottom with their starting point and their orientation are a central input element for the function. The outputs of the function are then a list of rays leaving the slab from the top and from the bottom including their position and their orientation and a list of rays that were absorbed inside the slab with the position of absorption. Additional output parameters are if any ray was lost as no intersection point could be found or if the calculations were interrupted because of the maximum number of bounces. A schematic representation of the function is given in Fig. 3.7.

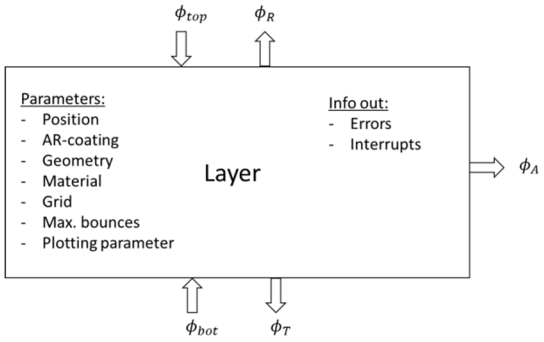

Fig. 3.7: Schematic representation of the Layer function in the SMARTI ray tracer

Having clearly defined the layer-function, the desired number of layers can be stacked on top of each other. Then, using a while loop, one layer after the other starting from the top is calculated using the output rays of the adjacent layers as input rays for the calculation. When the calculation of the last layer in the stack is performed, the while loop restarts with the first layer until all the rays are either transmitted through the stack, absorbed inside the layers, or reflected back out of the top layer. This process is depicted in Fig. 3.8.

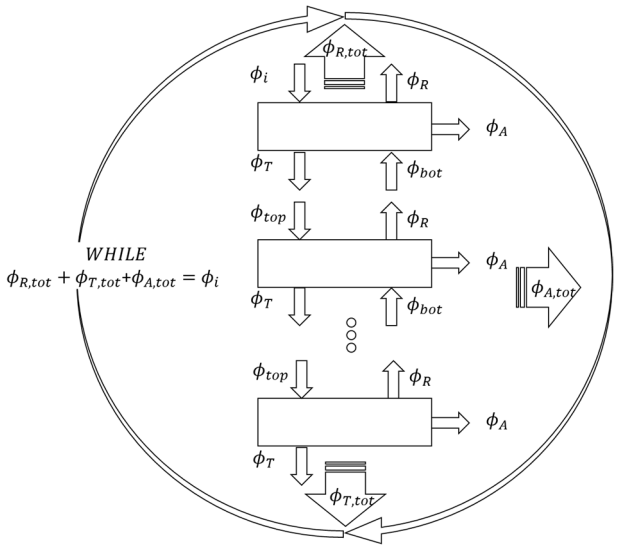

Fig. 3.8: Schematic representation of the ray tracing algorithm that is implemented in the SMARTI ray tracer

Inside the layer function, a mathematical algorithm is implemented that calculates the intersection points of the rays with the infinite planes that are formed by the geometry. After the determination of the intersection point, it is tested if the point lies within one of the triangles defining the geometrical structures.

To execute these two steps, it is necessary to give a mathematical definition for the rays and for the triangles that are involved in the calculation. There are multiple options to proceed concerning these definitions. The one chosen here gives a parametric definition for any point either on the ray or on the surface.

The parametric definition defines any point A on a line by the vector $\vec{A}$ that starts in the origin of the coordinate system. It is given by

$$\vec{A} = \vec{p}_1 + t \cdot \vec{P} \tag{138}$$

where $\vec{P}$ is a unit vector indicating the direction in which the ray is travelling and t is the distance between the starting point $\vec{p}_1$.

Each of the triangles, which together form the geometry of the layer, can be described by three 3 x 1 vectors. The first one is the position vector $\vec{p}_2$ indicating one corner of the triangle. The two other vectors $\vec{v}_1$ and $\vec{v}_2$ define two sides of the triangle and thus implicitly also the third side. It is important to note that the top of the surface is also defined by the order of these two vectors. The cross product of the two vectors results in a vector that indicates the direction in which the surface points and thus can be hit by a ray. Now any point on the whole plane that is defined by the triangle can be written in parametric form as

$$\vec{A} = \vec{p}_2 + r \cdot \vec{v}_1 + s \cdot \vec{v}_2 \tag{139}$$

At this point it is important to realize that this forms a coordinate system, which has its origin at $\vec{p}_2$ and the direction of its two axis are formed by the vectors $\vec{v}_1$ and $\vec{v}_2$. The variables r and s are the indicators of how many steps of the units with length $|\vec{v}_1|$ and $|\vec{v}_2|$ to be followed to come to point $\vec{A}$. To realize this is crucial to understand the steps that are needed for the decision if the intersection is inside or outside of the triangle. Coordinate systems that are defined in such a way are called *barycentric coordinate systems* [79].

The definition of the vectors can be seen in Fig. 3.9.

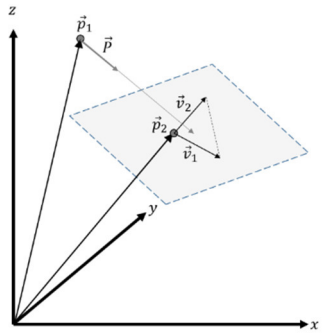

Fig. 3.9: Definition of the position and the direction vectors describing the ray and the geometry of the object

To find the intersection of the ray with the plane, the two parametric equations are set equal so that the following is received.

$$\vec{p}_1 + t \cdot \vec{P} = \vec{p}_2 + r \cdot \vec{v}_1 + s \cdot \vec{v}_2 \tag{140}$$

Rearranging this term gives

$$r \cdot \vec{v}_1 + s \cdot \vec{v}_2 - t \cdot \vec{P} = \vec{p}_1 - \vec{p}_2 \tag{141}$$

In coordinate representation, this is written as:

$$\begin{bmatrix} v_{1,x} & v_{2,x} & -P_x \\ v_{1,y} & v_{2,y} & -P_y \\ v_{1,z} & v_{2,z} & -P_z \end{bmatrix} \begin{bmatrix} r \\ s \\ t \end{bmatrix} = \begin{bmatrix} p_{1,x} - p_{2,x} \\ p_{1,y} - p_{2,y} \\ p_{1,z} - p_{2,z} \end{bmatrix} \tag{142}$$

Solving this simple system of linear equations is a very crucial step for every ray tracing software, as it consumes a very high share of the total simulation time. Even though many software tools such as MATLAB are capable of solving such a system in one step, it is often reasonable to manually program this step as the time consumption can be reduced.

A significant reduction of run-time could be achieved by the implementation of Cramer's rule [131]. This standard method for solving systems of linear equations can be tuned to increase the solving speed as the results of individual mathematical operations can be reused in different parts of the calculation procedure. The detailed description of the method can be found in [79].

When the variables r, s and t are found, the next step is to decide whether the intersection point of the ray with the surface is inside or outside of the triangle. As described above, the parameters r and s can be seen as linear factors describing any point in a coordinate system, which is built up by the basis vectors v_1 and v_2. The triangle of interest is the one formed by $1 \cdot v_1$ and $1 \cdot v_2$. Thus, the first thing that has to be determined is whether r and s are greater than 0. Another condition that needs to be fulfilled to be sure that the intersection point is inside the triangle is that the sum of r and s needs to be smaller than unity [79].

It could also be that the intersection point lies behind the starting point of the ray, which would result in a negative value for t. This would also be a reason to reject the intersection with the triangle. The final test for the correct determination of the intersection algorithm is that exactly one triangle may be hit during each run If more or fewer triangles are hit, an error is displayed.

When the right intersection point is found, a random number between zero and one is generated n_{rdm} and the reflectivity r, transmissivity t, and absorptivity a for the given angle of incidence and the given material parameter are calculated. If $n_{rdm} < r$, then the ray will be reflected and if $n_{rdm} > r + t$, the ray will be absorbed. In all other cases, the ray will be transmitted.

The ray tracing software includes many additional features, such as grid implementation, Lambertian scattering, a speed boost function, and isotropic irradiation, which are explained in detail in the corresponding use manual [132].

3.2.2 Short circuit current determination with PC1D

If a textured surface is selected in PC1D, a procedure is applied that approximates the three-dimensional surface for the one-dimensional FEM solution. This "quasi-one-dimensional" solution changes the cross-sectional area as a function of the solution dimension

x. For the case of a pyramid with the base angle β, the cross-sectional area at $x = 0$ is larger by the factor $1/\cos(\beta)$ compared to $x = W$, with W being the thickness of the cell. The reduction of the area proceeds with a Gaussian shape, where the standard deviation depth constant is 1/6 of the height of the pyramid d. This procedure can also be interpreted as a bending of the solution dimension x as can be seen in Fig. 3.10. However, care needs to be taken not to think that the solution dimension x is larger than W, as the figure suggests. The width W stays the same as if it were an untextured cell.

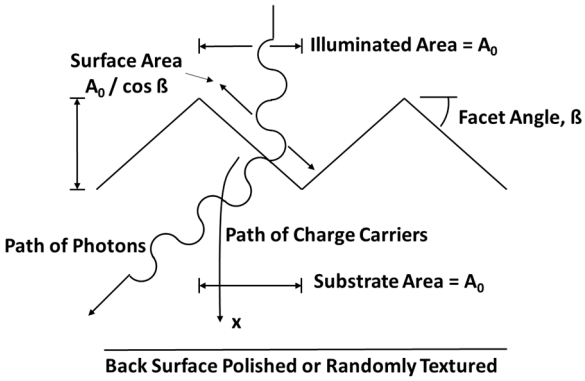

Fig. 3.10: Schematic representation of the solution dimension x and its derivation [25]

The whole procedure is done because it incorporates the increasing surface recombination velocity near a textured surface, which is a direct result of the increased surface area. Additionally to this procedure the generation profile is modified by assuming a modified angle of transmission close to the front surface (one-sixth of the facet depth). From there an abrupt change to the perpendicular transmission is assumed.

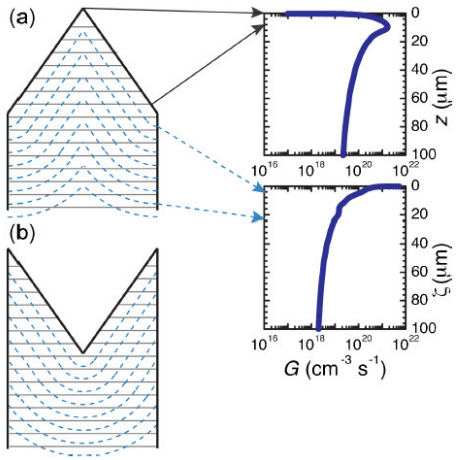

Fig. 3.11: Description of the difference between the one dimensional photogeneration profile for the dimensions z and ζ [59]

When a generation profile is imported into PC1D this "quasi-one-dimensional" solution also needs to be taken into account. A study by Baker-Finch and McIntosh [133] concerning this topic reveals the importance of choosing the right dimension for the generation profile created under a textured surface. For the one-dimensional profile, if the depth z is chosen as the coordinate axis starting from the highest point of the texture down to the

bottom of the cell, a characteristic kink occurs as can be seen in Fig. 3.11 (horizontal black lines). The authors propose a solution dimension ζ that is defined by the shortest distance in a three-dimensional space and the front surface. This approach is much more compatible with a one-dimensional semiconductor device simulator like PC1D as the thickness of the generation profile and the thickness of the FEM algorithm in PC1D are the same.

A generation profile is created for every wavelength and is subsequently imported into PC1D to determine the specific short circuit current. The process of importing the generation profiles is automated with MATLAB from which the command line version of PC1D is controlled.

The type of generation profiles that are required by PC1D are accumulative generation profiles starting at the depth coordinate $x = 0$ with the generation value of 0. For the creation of adequate generation profiles, two facts need to be taken into account. The first is that the values of the x coordinate have to be chosen with care. Especially for the depth values close to the surface, a higher resolution needs to be chosen because of the strong correlation between surface recombination and carrier density close to the surface. The second fact is that the absorption of photons in the long wavelength regime with values of $\lambda > 1050\,nm$ becomes very low, so that the absorption is evenly distributed over the whole cell. To still receive meaningful values, especially for the surface, it is mandatory to trace enough rays.

Two programmatic approaches were followed to handle these topics. First the number of rays that are traced can be set to different values for the regimes larger and smaller than $950\,nm$. Secondly the discretization of the depth coordinate x is different for the values larger and smaller than $950\,nm$. The exact procedure for the discretization of the two regimes can be found in the SMARTI user manual [132].

It was decided to switch off the texture function in PC1D because in the case of an external generation profile only the increased surface recombination due to the texture is applied and the same effect can be achieved by setting the front surface recombination velocity to an appropriate value.

3.2.3 Testing the numerical model

The SMARTI ray tracer was tested in comparison to the software Wafer Ray Tracer (WRT) [134], which is freely available in a restricted version. The WRT is able to simulate solar cells with different front and back side textures as well as with thin coatings on both sides. However, it is not capable of simulating a whole module including encapsulation material and the contact grid.

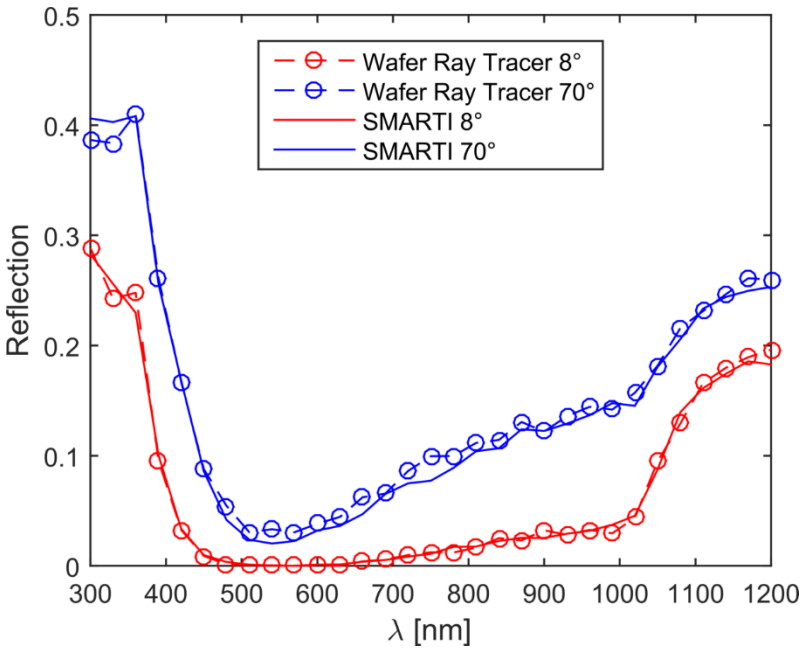

Fig. 3.12: Regular upright pyramids, back side reflectance 0.5 and Lambertian share 0.5

In Fig. 3.12 the simulated reflection curves for incidence angles of 8° and 70° can be seen for the WRT and the SMARTI ray tracer. The curves for 8° have almost the same results while the slight deviation for 70° is caused by the fact that the freeware version of the WRT only supports a limited number of rays for the simulation, which lead to observable random variations in the reflection curve.

As the simulation speed is a limiting aspect of each ray tracing software, the times needed for the simulation of three different configurations were recorded for 1000, 2000, and 5000 rays per wavelength with wavelengths ranging from 300 nm to 1200 nm in steps of 30 nm. The results are plotted in Fig. 3.13.

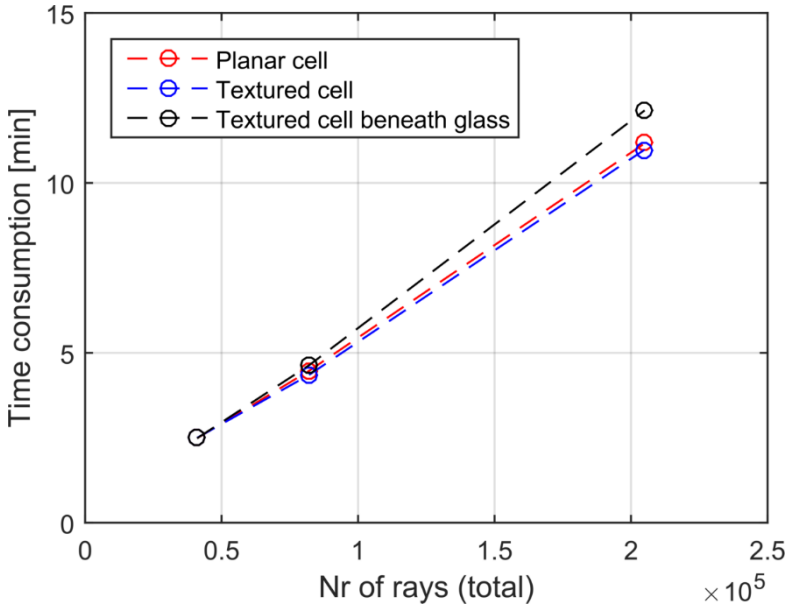

Fig. 3.13: Time consumption of simulation over total number of simulated rays

This benchmark test for the software is of course strongly dependent on the computer that is used to execute the program and the processes that run in parallel. The processor is a Pentium® i7 with 2.9 Ghz, 4 CPU cores, and 16 GB RAM. The number of rays that is needed for accurate simulation of the results depends strongly on the purpose of the simulation. If for example, the IQE curves at two different angles of incidence should be compared to each other in high accuracy, the generation profiles for all wavelengths need to be produced. Especially in the long wavelength regime > 960 nm where the absorption becomes low, many rays need to be traced. To receive suitable results, 100,000 rays were traced per wavelength for wavelength steps of 30 nm in the range from 300 nm to 1200nm leading to simulation periods of about 5 hours per simulated batch. Using parallel computing on different CPU or GPU it is possible to enormously accelerate the computing speed.

4 Measurement approach

It is not straightforward to separately measure all the mechanisms that are relevant concerning the angular behavior of a solar cell. This thesis focuses on the measurement of the angular spectral response $SR(\lambda,\theta)$ and the angular spectral reflection $R(\lambda,\theta)$. Combining both allows determining the angular internal quantum efficiency $IQE(\lambda,\theta)$.

In addition to these measurements, the electroluminescence spectra at different angles of incidence $EL(\lambda,\theta)$ were determined. This was done to evaluate if $SR(\lambda,\theta)$ can be derived directly from $EL(\lambda,\theta)$ with the help of the reciprocity relation described in section 2.7.

The methods used for measuring $SR(\lambda,\theta)$, $R(\lambda,\theta)$ and $EL(\lambda,\theta)$ are described in detail in the following sections.

4.1 Angular spectral response measurements

While the measurement of the spectral response at perpendicular incidence $SR(\lambda)$ is a standard measurement procedure for research and industry, the angular measurement $SR(\lambda,\theta)$ is not yet very common.

Just recently, the Fraunhofer ISE [21] and the Physikalisch Technische Bundesanstalt (PTB) [22] presented their methodology and results for the determination of the angular spectral response.

The approach used in this thesis has some similarities to this approach and will be described in the following.

4.1.1 Measurement setup

For the measurement of the SR, monochromatic light is needed, which is directed onto a measuring table where solar cells and mini solar modules can be fixed for measurement.

A reference module with a known SR-Curve $SR_{rc}(\lambda)$ is used for calibration. The measurement procedure is the following. First the short circuit current $I_{sc,rc}(\lambda)$ of a reference cell with cell area A_{rc} is measured. Then, the short circuit current $I_{sc,tc}(\lambda)$ of the test cell with cell area A_{tc} is determined.

Now the spectral response $SR_{tc}(\lambda)$ of the test cell can be determined by

$$SR_{tc}(\lambda) = \frac{SR_{rc}(\lambda)}{I_{sc,rc}(\lambda)A_{tc}} A_{rc} I_{sc,tc}(\lambda) \tag{143}$$

There are different measuring instruments available on the market, which mainly differ in their method to produce monochromatic light. This can be done by using light emitting diodes (LED) with different light colors, which can be individually modulated with a specific frequency to subsequently demodulate the current signal caused by the LED. Using this approach, measurements of the whole spectral response curve can be performed in 1 to 10 seconds [135, 136]. The monochromatic light can also be provided by a laser system

such as a tunable mode-locked Titan:Sapphire laser combined with different nonlinear optics as employed by the PTB [22].

Another possibility to generate monochromatic radiation is to use a single or double grating monochromator. White light, which is incident on the grating, is reflected with a different angle depending on its wavelength. Using a second grating helps suppress stray light. As the gratings are commonly small in size, the monochromatic light spot that is generated is small in size and will in general be smaller than the solar cell under investigation.

An alternative method to produce monochromatic light is by guiding white light through one or several filters consisting of coated glass which block all colors except for the desired one. Such a filter monochromator consisting of 40 colors (338.7 nm to 1188.1 nm) is used in the spectral response setup that was used for this thesis.

The original system, which was constructed by the company Aescusoft, was adapted to measure angles of incidence resolved spectral response curves. The water cooled Xenon short-arc lamp (1000 W electric consumption) was retained as well as the two filter wheels containing the 40 filters. Moreover the equipment to measure the voltage drop over the selected shunt resistance was kept. Here the light is modulated with the help of a chopper wheel creating a corresponding current signal. This signal can be tracked and demodulated with the help of a lock-in amplifier from Signal Recovery (Model 7265) increasing significantly the signal to noise ratio. An additional measurement of the voltage drop over the cabling (4 wire measurement) allows the compensation of this drop with the help of a regulated power supply (Toellner TOE 7610).

For the adaption to AOI measurements, the mirror directing the light onto the measuring table was removed. The table itself was modified so that it can be rotated around the y-axis so that the temperature control could be used. It consists of a cooled water stream and a series of Peltier elements beneath the copper plate where the cell is located. A technical drawing of the measuring table and a photograph of the measurement configuration at an AOI of about 60° are shown in Fig. 4.1.

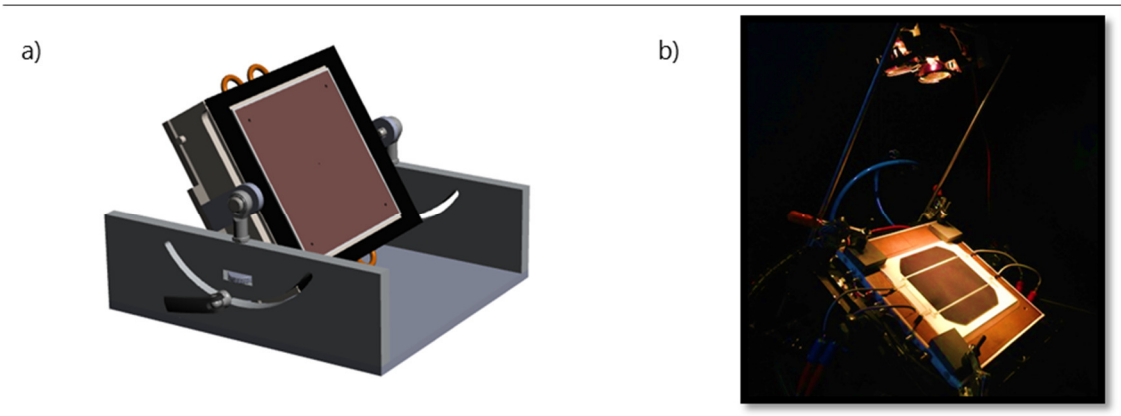

Fig. 4.1: Modified measuring table for AOI spectral response measurements. a) Technical drawing, b) Photo of an example measurement situation with a monocrystalline solar module at a AOI of 60°

The reproducibility of the positioning of the sample is ensured by the indication of the horizontal and vertical middle lines on the measuring table as well as on the sample itself. The fixing is done at three edges by means of clamping.

When measuring the angular spectral response, a central decision needs to be made is if the measurement should be done over the entire area of the cell (referred to as 'global' in the following) or for a specific spot on the cell (referred to as 'local'). While for the first case the light field needs to larger than the solar cell, a small light spot of any shape (generally circular or squared) can be used for the local measurement case. Both have advantages and disadvantages, which need to be considered in the decision. While the global measurement gives no information about the spatial inhomogeneity of the spectral response, the local measurement provides high resolution information about one small area of the cell. The inhomogeneity of the spectral response can be significant, depending on the cell technology and the quality of the production steps involved. Thus, it can be meaningful to perform a spatial mapping of the whole solar cell [137]. As this was not feasible for this thesis, it needed to be accepted that spatial information is lost either by the integration of all spectral responses using the global approach or by not measuring all spots of the cell.

As for the global approach, the homogeneity of the light field is crucial, a spatial mapping of the light field in the y-z-plane was performed using an xy-stage in the upright orientation. A technical drawing and a photograph can be seen in Fig. 4.2.

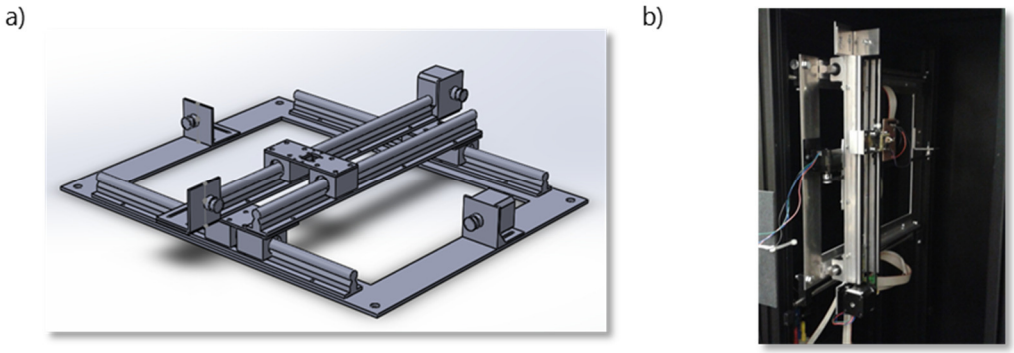

Fig. 4.2: Measurement setup for the light field measurement of the different filters of the filter monochromator

The measurement was performed with a silicon photodiode (Osram BPX61), which was short circuited over a measurement shunt. The shunt voltage was subsequently amplified using an operational amplifier in the inverting circuit configuration.

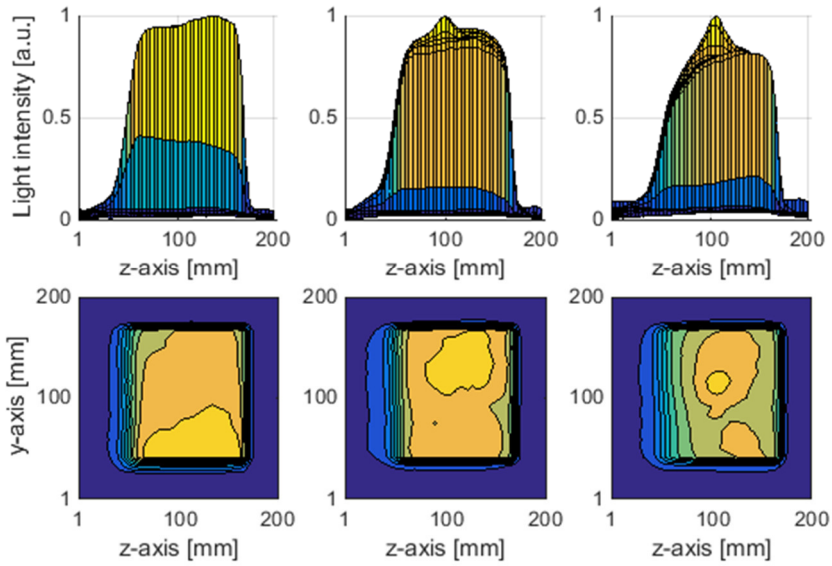

Fig. 4.3: Light field distribution for three different filters (884 nm, 938 nm, 979 nm)

It was found that the filter inhomogeneity is tremendous for some of the filters employed in the filter monochromator. Three examples for these intensity deviations caused by the filter inhomogeneities are presented in Fig. 4.3. While the filter at $884\,nm$ has a slope of decreasing intensity, the filters for $938\,nm$ and $979\,nm$ show peaks of higher intensity. These variations lead to significant errors when the rotational stage is moved to a higher AOI as the specific light intensity per area changes. A mismatch correction for every filter and angle of incidence would in principle be possible, but the effort would be high and an additional source of error would originate from such a correction procedure.

This was one of the reasons why a pinhole aperture was inserted into the light field, so that only a small round light spot is incident on the solar cell. The spot size was chosen to be roughly $15\,mm$ in diameter so that it is small enough that when the AOI is set to 70°, the light is still in between the two busbars of the planar cell under investigation ($60.07\,mm$). It was not chosen to be smaller as the signal strength should be kept as high as possible.

Another reason for the choice of the local measurement approach was that the angle dependent reflection measurement, which is presented below, is by its construction only applicable in the local configuration. To be able to calculate the IQE from the SR and the reflection measurements, the size of the light spots on the solar cell was adjusted to be comparable.

A bias light was fixed to the rotational measurement table to ensure a constant bias illumination for all AOI. A representation of the whole measurement setup can be seen in Fig. 4.4.

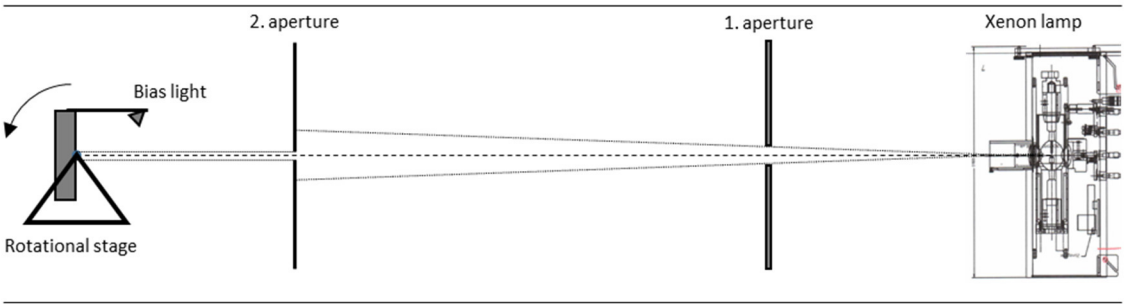

Fig. 4.4: Schematic representation of the measure

4.1.2 Error determination

In principle, measurement errors can be divided into two different types: systematic error and random error [138]. Systematic errors cause a constant deviation from the real measurement value, which will always be the same when the measurement is repeated. So, if the magnitude of this error is known, then the measurement results can be corrected to receive the actual measurement result. To avoid systematic errors, it is crucial to know all the factors that can influence the measurement results and to build up the measurement setup in a way to exclude or to correct as many of these influences as possible.

Random errors are statistical deviations from the "true value"; the measured, i.e., observed, value may vary from one measurement to another. They mainly occur when the equipment, which is used in the measurement setup, is not fully controllable because of technical limitations or fundamental limits to the measurement accuracy.

For the case of the angular spectral response measurement system, the following systematic errors could be identified. As already mentioned above, the light field is not completely uniform due to inhomogeneous filters. This effect could be reduced strongly as the local approach was chosen for the measurement. There is still an inhomogeneity of the light field in the small light spot, but as the radiation remains on the surface of the cell, the influence will not be significant.

But this gives rise to the second systematic error, which is due to the fact that the light spot increases with the increasing angle of incidence due to the cosine effect. This leads to an inclusion of cell area, which was not irradiated before, and a simultaneous decrease of the specific irradiance [W/cm^2]. The error that is caused by this effect is thus strongly dependent on the type of cell or module under investigation.

Another systematic error could be caused by the fact that the reflection increases due to increasing AOI and thus more light is reflected back from the walls of the enclosure to the cell on the measuring table. To evaluate the possible influence of this effect, a light absorbing material was placed at the wall where most of the back reflection would take place. A comparison with the measurements from before did not show a significant change in the results.

The thickness of the module samples can cause a systematic error as the light spot possibly does not stay centered and in the case of a thick glass encapsulation, the light might be directed onto the busbars or even over the edges of the solar cell. This is the reason why only very thin transparent encapsulation layers made from PVDF (Polyvinylidene fluoride) where employed in this thesis; thus, keeping the module as thin as possible.

The area, which is covered by the light spot, increases along the direction of the contact fingers so that the fraction the fingers covered stays constant. But a systematic error could be introduced by the fact that at low angles, the light spot becomes closer to the busbar, which could influence the optics close to the busbar. Photons could either be reflected from the busbar or they cannot escape from the cell as they hit the busbar from inside. As the distance to the busbar is still quite large, even at low AOI values, this effect is assumed to be marginal. However, the correct positioning of the solar cell is of high importance and since it can slightly vary from sample to sample, this effect will be addressed as a random error below.

The polarization of light significantly influences the optical performance of the solar cells and modules as was described in section 2.3. As the polarization of the light produced by the Xenon short arc lamp was not measured, the systematic error, which potentially is introduced if the light was not linearly polarized, cannot be estimated. Since no further information was available on the polarization state of such a lamp, a linear polarization was assumed.

As already mentioned above, the change in AOI causes the irradiance to decrease for steeper angles of incidence. As some effects in a solar cell are injection dependent [139], this could lead to a change of the electrical performance of the solar cell. As the bias illumination keeps the solar cell in an excited state, the effect is assumed to be negligible.

The effects that could lead to a systematic error are summarized below:

- Light field inhomogeneity
- Light spot is spread over larger area
- Back reflection from the walls of the measurement enclosure
- Thickness of the samples
- Increasing influence of fingers and busbars
- Polarization
- Irradiance non-linearity

For the estimation of the occurring random errors, only the values at wavelength of 1121 nm and for the angles of incidence of 8° and 70° were analyzed. These points of operation were chosen because the absorbance of the silicon detector becomes too low for higher wavelengths and it is expected that if the measurement values at this wavelength are trustworthy, they can also be trusted at lower wavelengths. Using this approach is a fast and reliable strategy to estimate the error of the IQE measurement without taking into account complex dependencies of some random errors on wavelength and AOI.

If the true value to be measured is M_{true}, the measured value M_{meas} will be

$$M_{meas} = M_{true} \prod_i \delta_i \tag{144}$$

where δ_i is the relative random error which is produced by the process i.

The first random error is the variation of the lamp's intensity δ_l, which is assumed to be in the range of 0.2 %, independent of AOI. This value was determined by a time series measurement of the white light. At these intensities, the error of the voltmeter was assumed to be negligible. However, it should be mentioned that the Xenon lamp has three characteristic peaks at about $820\ nm$, $880\ nm$, and $940\ nm$, which may vary a little bit stronger than the intensities at other wavelengths and thus exceed the 0.2 %.

The correct positioning of the solar cell cannot be completely assured as the mark on the cell or module needs to be adjusted and fixed manually. The introduced error δ_p, which is caused by an imperfect positioning, is assumed to be 0.1 % for 8° and 0.2 % for 70°.

The angle is also set manually for every measurement. The angle is controlled with a digital level, which has a high accuracy. The error δ_a which is caused by the angle uncertainty, is assumed to be 0.1 % for 8° and 0.2 % for 70°.

The temperature of the cell is well regulated. And as the short circuit current is measured, which is not strongly temperature dependent, the error δ_T for the temperature variation of the solar cell or module is assumed to be only 0.1 % for both angles.

Another relatively high random error is introduced by the lock-in measurement setup including the chopper wheel, the shunt resistance temperature variation, and the voltage compensation of the 4-wire measurement. It is strongly wavelength dependent as the signal in the near infrared region $> 1000\ nm$ becomes very low. For the current determination, N_s individual measurements are recorded and averaged. The measurement is stopped when the standard error of the mean (SEM) drops below a determined value. The SEM is here referred to as $S_{\bar{M}}$ and is calculated by

$$S_{\bar{M}} = \frac{s}{\sqrt{N_s}} \tag{145}$$

where s is the sample standard deviation [140]. By this method, the random error δ_m introduced by the measurement can be reduced to 0.2 % at 8° and 0.3 % at 70°.

The random error processes are listed in Table 4.1 along with the corresponding error values.

Table 4.1: Random errors of the angular spectral response measurement setup

Random error process	Error introduced by process	
	AOI=8°	AOI=70°
Lamp flickering and variation	$\delta_l(8°) = 1 \pm 0.002$	$\delta_l(70°) = 1 \pm 0.002$
Positioning of the sample	$\delta_p(8°) = 1 \pm 0.001$	$\delta_p(70°) = 1 \pm 0.002$
Angle setting accuracy	$\delta_a(8°) = 1 \pm 0.001$	$\delta_a(70°) = 1 \pm 0.002$
Temperature	$\delta_T(8°) = 1 \pm 0.001$	$\delta_T(70°) = 1 \pm 0.001$
Lock-In amplification	$\delta_m(8°) = 1 \pm 0.002$	$\delta_m(70°) = 1 \pm 0.003$

The total error that is introduced by the different random processes is most probably not the maximum possible error but as the impact of the different errors randomly increase and decrease a statistical evaluation is necessary. This can be done by means of the Monte Carlo method by performing measurement results that are randomly weighted by the errors presented above [141]. This analysis leads to the result that the total error with a confidence interval of 95 % is 0.49 %, i.e., 95 % of all measurements will be in the range of $M_{EQE} \cdot (1 \pm 0.049)$. Repeated measurements of the angular spectral response confirm this value. It should not be forgotten that the calibration process also introduces errors into the determination of the EQE. But as in this thesis, the measured quantity at any AOI is always compared to the quantity at perpendicular AOI, the calibration factors cancel out and do not influence the error of the comparison result.

4.2 Angular reflection measurements

The measurement of the hemispherical spectral reflectance $R(\lambda, \theta)$ of a solar cell or module is a common approach in the photovoltaic science community and industry to evaluate the optical properties of the sample under investigation.

In general, the measurement is performed with the help of an integrating sphere at an incident angle of 8°, as a measurement at 0° would cause the direct reflected light to leave the sphere through the port from which it entered.

There are also some common measurements, which evaluate the optical properties at angles other than 8°. Spectroscopic ellipsometry, for example, is a standard method for the determination of the optical properties of thin films and substrates such as thickness and the complex refractive index N [142]. For some scientific or industrial purposes it is interesting to know the directional information of the reflected light. This information is included in the so-called bidirectional scattering distribution function ($BSDF$), which is also a measure for the roughness of a surface between totally planar and completely Lambertian [143]. The $BSDF$ is generally determined by goniometric instruments [77]. As these instruments have to track the entire or a semi-sphere around the illuminated sample, the measurement procedure is relatively time consuming. This is also the reason why usually only one or a few different wavelengths are investigated. As the goniometer detector that rotates around the sample is also a potential source of back reflection of light onto the sample, the distance between the detector and the sample should be as large as possible.

Another angular measurement procedure using reflection data is referred to as variable angle spectroscopy (VAS) [142], which only detects the direct share of the reflected light. It is also used for the determination of optical properties of thin films and can also be used for the $BSDF$ determination. It is also used to analyze the random pyramidal structures implemented in monocrystalline solar cells [30].

An advantage of some of the products on the market is the integration into measurements systems, which were originally built for perpendicular measurements only [144].

As a standard solar cell has dimensions of 156 x 156 mm, it will not be possible to entirely place it into a state of the art VAS measurement system. That is why Parretta et al. proposed three different methods to determine the angular reflectance of full size wafers or even modules. To measure modules, the back side port of an integrating sphere is placed directly on top of the solar module or cell being studied. The incident light can then be placed at one of the ports having a fixed angle in relation to the back side port where the sample is positioned [145]. The second proposal also includes a number of fixed ports for each AOI, but the solar cell or mini module is placed in the center of the integrating sphere [146]. The third setup is the one that was used in this thesis. The sample is placed in the middle of an integrating sphere on a rotational stage, so that there is only one port for the incident light and another for the detector [147].

The detailed setup description and measurement procedure are explained in the following section.

4.2.1 Measurement setup

The heart of the angular reflection measurement setup is an integrating sphere with a 500 mm diameter that was manufactured by Doser Messtechnik. The inner coating consists of barium sulfate ($BaSO_4$), which in general features reflectivity values above 95 % for the wavelength range $300\ nm$ to $1200\ nm$ [148]. The integrating sphere has an entrance port of 30 mm diameter for the light in-coupling and two measurement ports that are shaded by baffles against the first direct reflection coming from the sample.

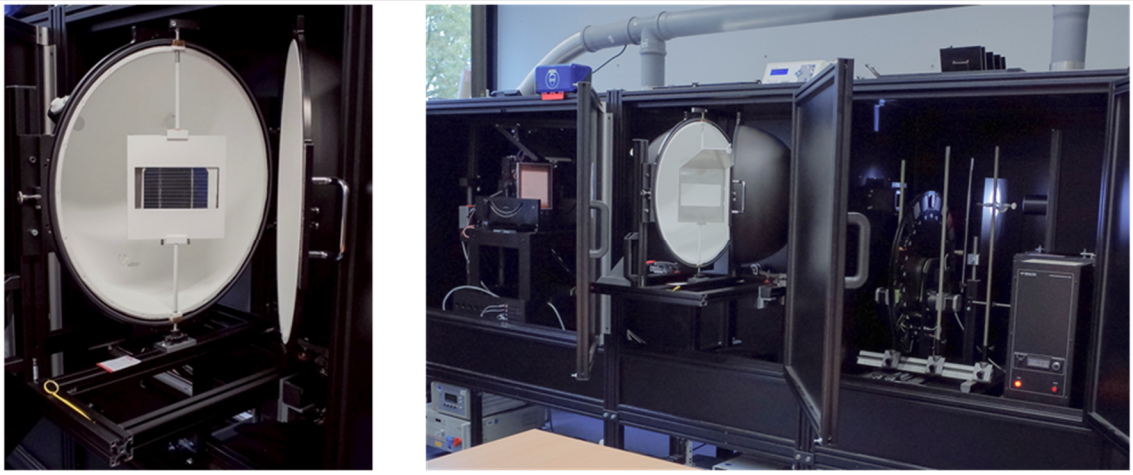

Fig. 4.5: Left: Sample holder inside the integrating sphere from the front side; Right: Integration of the integrating sphere inside the spectral response measurement system.

The sample holder was produced in house to match the requirements for the different cells and modules being studied. Its rotational axis is located vertically in the middle of the integrating sphere. The rotational angle is indicated by an angle disc beneath the sphere. The sample is placed into the holder from behind, where a flap can be opened upwards. After testing the mechanical functionality of the sample holder, it was coated with $BaSO_4$ by an external company. The integrating sphere including the sample holder can be seen in Fig. 4.5.

The integrating sphere with the sample holder inside is mounted to an aluminum frame. This platform is mobile and can be positioned inside the housing of the spectral response measurement system as it can be seen in Fig. 4.5 (right). Inside the housing, the integrating sphere can be accurately positioned and subsequently clamped to keep its position. If the sample must be changed, the integrating sphere can be pulled out up to a certain position; thus, allowing it to be opened.

Using the same setup as the spectral response measurement system has the advantage that the same illumination source including the two filter wheels can be used. However, a silicon photodiode is used for the signal detection, which is amplified by an optometer (P 2000 by Gigaherz-Optik). The measurement control software was programmed using Lab-VIEW. Three separate measurements need to be performed for every reflection value. The first is measured with the entrance port closed, so that the dark current of the sensor can be determined. The measured value M_{dark} is not dependent on the wavelength. The second measurement is performed on the $BaSO_4$ back side of the sample holder, which sets the sensor to the value M_{ref}, which will subsequently be used as the reference for full reflection. The third measurement is performed on the front side of the test sample and is referred to as M_{ts}. All of the measured values are computed as the statistical mean of many individual measurements using a SEM threshold value as described above for the SR measurement.

Using the three separate measurement results, the reflectance is then calculated by

$$R(\lambda,\theta) = \frac{M_{ts}(\lambda,\theta) - M_{dark}}{M_{ref}(\lambda,\theta) - M_{dark}} \tag{146}$$

To fully understand this measurement principle and to determine its potential error, the theory of the integrating sphere needs to be known. The inner surface of the integrating sphere is assumed to be a perfect Lambertian reflector. If photons are incident on an infinitesimal small area of this surface, they are reflected so that every other surface element receives the same amount of photons. Each of these elements itself can then also be regarded as a Lambertian source of light. From here it can be demonstrated that the radiance of the entire sphere wall L_{sp} can be calculated by setting up an infinite sum of all reflections taking place in the sphere [149].

$$L_{sp} = \frac{\phi_{in}}{\pi A_{sp}} \cdot \frac{R_{sp}}{1 - R_{sp}\left(1 - f_{sp}\right)} = \frac{\phi_{in}}{\pi A_{sp}} SM_{sp} \tag{147}$$

Here ϕ_{in} is the initial flux coming from the light source, A_{sp} is the inner surface area of the sphere, and R_{sp} is the reflectivity of the $BaSO_4$ coating. The parameter f_{sp} is the port fraction. The term SM_{sp} is referred to as the sphere multiplier. It is generally larger than 1 and realistic values for integrating spheres are in the range between 10 and 30 [150], which means that the flux inside the sphere is much higher than the initial flux coming from the light source.

The value of the sphere multiplier should be high so that a uniform distribution of the light over the whole sphere surface can be achieved and that the measurement is less prone to spatial non-uniformities in the sphere caused by baffles, shadows and ports. Also the rotational stage in this setup needs to be partly considered as a baffle for the radiation inside the sphere.

4.2.2 Error determination

Distinguishing between systematic and random errors is also reasonable for the angular reflection measurements. Some of the systematic errors are similar to the ones described in the angular spectral response setup. The light spot on the cell or module is of a similar size and thus expands when the angle of incidence is changed; thus, new regions are included, which potentially have differing reflection properties. The plane of measurement in this setup is determined as the sample is placed to the sample holder from behind. This reduces the error compared the spectral response setup, where the thickness of the cell or module influenced the position where the first intersection with the sample took place. Nonetheless, a significant error can arise if modules with thick glass encapsulations are measured, because the light can escape through the edges of the sample. Furthermore, in this setup, the influence of the busbars on the measurement can increase at oblique light measurements just the same as in the case of the SR determination. And also, the polarization properties of the lamp can systematically influence the measurement.

Concerning the systematic errors, which can be caused due to the measurement principle of the integrating sphere, there are mainly two aspects that can systematically influence the measurements. The first is the influence of the port fraction on the sphere multiplier. In general, the port fraction should not exceed 5% of the total internal sphere area [150], which is not the case for the reflection setup if only the visible part of the sample area is considered as the port fraction and the rest of the sample holder is not viewed as a disturbance for the process of uniformly distributing the light inside the sphere. Another potential systematic error, which is related to the port openings, is that at low angles of incidence a share of the light that is reflected inside a cone surrounding the beam of direct reflection escapes the integrating sphere through the port it entered. This effect could be reduced by reducing the port opening from 50 mm diameter to 30 mm.

The random errors, which occur during the measurements, are also similar to the ones that were described for the spectral response setup. However, one basic difference between the measurements is that there are three individual measurements involved (M_{dark}, M_{ref} and M_{ts}), all of which carry their own random error, in the reflection measurement. All of the random errors for the individual measurements are presented in Table 4.2.

Table 4.2: Random error processes for the reflection measurements

Random error process	Error introduced by process	
	AOI=8°	AOI=70°
Lamp flickering and variation	$\delta_l(8°) = 1 \pm 0.002$	$\delta_l(70°) = 1 \pm 0.002$
Positioning of the sample	$\delta_p(8°) = 1 \pm 0.001$	$\delta_p(70°) = 1 \pm 0.002$
Angle setting accuracy	$\delta_a(8°) = 1 \pm 0.001$	$\delta_a(70°) = 1 \pm 0.002$
Optometer measurement, test sample	$\delta_{m,ts}(8°) = 1 \pm 0.002$	$\delta_{m,ts}(70°) = 1 \pm 0.003$
Optometer measurement, reference	$\delta_{m,ref}(8°) = 1 \pm 0.003$	$\delta_{m,ref}(70°) = 1 \pm 0.003$
Optometer measurement, dark	$\delta_{m,dark}(8°) = 1 \pm 0.03$	$\delta_{m,dark}(70°) = 1 \pm 0.03$

While the measurement error of the reference measurement and the dark measurement do not depend on the AOI, the measurement of the test sample has a higher error value at 8° compared to the measurement at 70°. Using the Monte Carlo approach, the random error for the test sample measurement $\delta_{m,ts}$ for 8° and for 70° could be determined as well as the random error for the reference measurement $\delta_{m,ref}$ and the dark measurement $\delta_{m,dark}$.

To determine the total random error of the reflection measurement it is not possible to simply multiply the individual errors of the measurements. Because of the mathematical manipulation that needs to be performed to determine the reflection value, the random errors are treated identically. Thus, the total error of the reflection measurement at the AOI θ_i (here 8° and 70°) are determined by

$$\delta_R(\theta_i) = \frac{\frac{M_{ts}(\theta_i)\delta_{m,ts}(\theta_i) - M_{dark}\delta_{m,dark}}{M_{ref}\delta_{m,ref} - M_{dark}\delta_{m,dark}}}{\frac{M_{ts}(\theta_i) - M_{dark}}{M_{ref} - M_{dark}}} \tag{148}$$

It is obvious that the total random error is also dependent on the result of the measurement. The actual results of a planar non encapsulated solar cell and the ones of a standard solar module where used to solve the equation. The results were quite similar, which is the reason why here only the results of the standard module are presented.

To determine the range of the error for the case of this measurement, it is meaningful to calculate the maximum error that can occur by combining the individual errors of the measurement. After numerically checking all possible combinations, the total error for the reflection measurement $\delta_R(8°)$ was found to be 0.97 % and for $\delta_R(70°)$ the result was 1.22 %.

4.3 Measurement error of the angular *IQE* factor

As the determination of the IQE from the measured values of EQE and R requires the mathematical manipulation $IQE = EQE/(1-R)$, the same numerical procedure was applied, which was presented in the preceding section. As this thesis mainly focuses on the change of IQE with a change in AOI, the error of the f_{IQE} determination is presented in the following.

The error $\delta_{f,IQE}$ can be found by

$$\begin{aligned}\delta_{f,IQE} &= \frac{IQE(70°)\cdot\delta_{IQE}(70°)}{IQE(8°)\cdot\delta_{IQE}(8°)} \Big/ \frac{IQE(70°)}{IQE(8°)} \\ &= \frac{\frac{EQE(70°)\cdot\delta_{EQE}(70°)}{EQE(8°)\cdot\delta_{EQE}(8°)} \cdot \frac{\big(1-R(8°)\cdot\delta_R(8°)\big)}{\big(1-R(70°)\cdot\delta_R(70°)\big)}}{\frac{EQE(70°)}{EQE(8°)} \cdot \frac{\big(1-R(8°)\big)}{\big(1-R(70°)\big)}}\end{aligned} \tag{149}$$

Here again measured values (in this case EQE and R) are needed to determine the error. But as the measured values of the EQE cancel out, only the measured values for the reflection on a standard module at the incidence angles of 8° and 70° are thus inserted. After numerically inserting the different combinations for the corresponding error values the maximum random error value for the f_{IQE} determination was found to be $\delta_{f,IQE} = (1 \pm 0.0156)$, corresponding to a maximum error of 1.56 %.

4.4 Angular electroluminescence measurements

The reciprocity relation of solar cells and modules that was introduced in section 2.7 allows determining the EQE from the measurement of the electroluminescence (EL) spectrum. in principle the theory also allows determining of the EQE at an arbitrary AOI [104]. However, in the literature, such a measurement approach has not yet been presented. Thus, in

this thesis, two different approaches to measure the angular EL will be explored and the feasibility of the determination of the EQE from such measurements will be evaluated.

There are two reasons why this alternative measurement of the angular EQE is a promising approach. It is potentially much faster than the determination of the EQE with a filter monochromator, depending on the integration time, which is set for the measurement of the EL spectrum. Furthermore, the spectral resolution of the EL measurement is much higher than the one of the filter monochromator.

In any case, it provides a second measurement for the determination of the angular EQE und thus a confirmation of the standard measurement.

In the following, the two measurement approaches for the angular EL measurement will be described.

As previously described for the measurement principles of the SR, one can also distinguish between a local and a global measurement approach of the angular EL measurement. While the EL spectrum of a specific region of the sample is measured for the local measurement, the global approach detects the EL spectrum of the entire solar cell or module.

A multi-mode optical fiber was used to guide the photons to the detector array of the spectrometer for both approaches. The glass fiber has a numerical aperture (NA) of 0.1 and a corresponding acceptance angle of 5.74°. Thus, the total angle of the acceptance cone is 11.48°.

For the local approach, the opening of the fiber core is located 10 mm above the sample and fixed to a mechanical mount that can be rotated around an axis, which is aligned with the top plane of the sample being studied. A picture of the setup and a schematic illustration can be seen in Fig. 4.6.

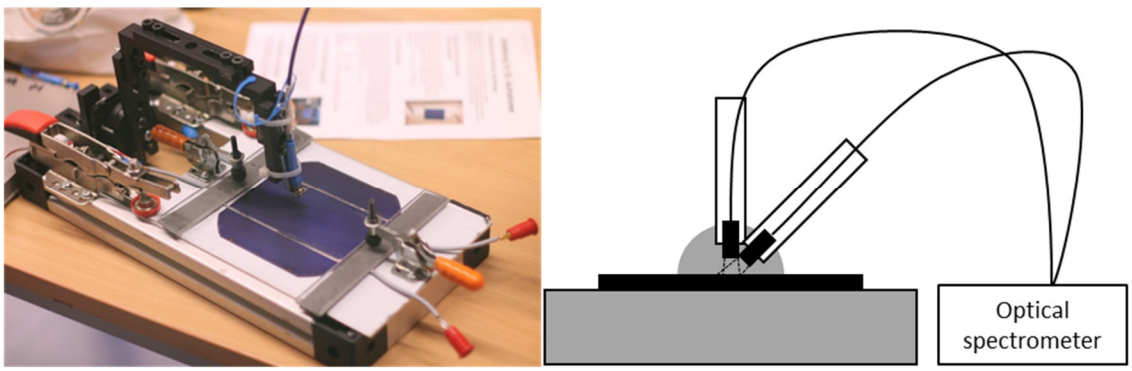

Fig. 4.6: Photograph and schematic illustration of the local measurement approach for the angular EL determiantion

The applied voltage for the forward bias was set to be approximately the open circuit voltage V_{oc} of the sample under STC. The resulting current is then in the range of the short circuit current I_{sc} under STC. The voltage applied to the cell is measured at two additional terminals at the samples junctions. Even though the voltage is important for the exact

determination of the EQE from the EL using the reciprocity relation, in the case of comparing the EQE curves at different AOI, the voltage is the same and thus cancels out.

Despite the promising results, the local approach was rejected because of potential systematic errors caused by the setup. The back reflection of photons from the parts that are close to the surface of the sample can have a significant impact on the results. Furthermore, there was no temperature control available in the setup so that the cell sample could not be held at a constant operating temperature.

The second approach tested for the angular EL measurement was a global setup. It used the same optical fiber, which now however was located in front of the rotational measurement table, which is also used for the angular SR measurement. The sample is set to a constant temperature by the integrated temperature regulation system. The distance between the sample and the opening of the optical fiber is approximately 3 m. The setup principle is illustrated in Fig. 4.7.

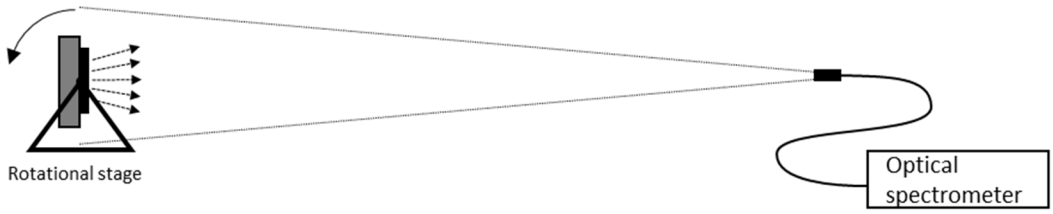

Fig. 4.7: Schematic illustration of the global setup for the determination of the angular EL

The light emitted by the cell and that subsequently entered the optical fiber is relatively parallel because of the distance to the sample. The maximum AOI of photons coming from the top or the bottom of the sample is about 1.5°. This makes the EQE determination by this setup comparable to the EQE setup using the filter monochromator and no aperture (global measurement configuration).

The EL measurement at each AOI consists of a dark measurement with no voltage applied to the sample and a measurement with voltage applied. The dark measurement was then subtracted from the one with voltage applied, so that the result is the spectrum that is caused by the current flow through the device. The spectrum is in arbitrary units as long as it is not calibrated. For this thesis, it is sufficient to compare the arbitrary unit spectra at different AOI because any calibration factor will anyhow become canceled out.

The photo spectrometer that was used for the detection was an Ocean Optics NIRQuest 512. The detector array is an Indium Gallium Arsenide (InGaAs) array produced by Hamamatsu and is thermo-electrically cooled for thermal noise reduction. Unfortunately, the temperature control generates sudden temperature changes, which caused problems with the evaluation of the spectral data. Even though useful results could be recorded, a spectrometer with a better cooling system is needed to ensure the reproducibility of the measurements for future investigations. The results of the measurements will be presented in the next section.

5 Explaining the angular effects on the quantum efficiency

In this section, a detailed description of the results is given that were determined by the simulation methods and the measurements presented above. After giving a general overview on the different effects that are caused by a variation in AOI and a subsequent definition of the angular correction factors, three different sample types are analyzed. The first sample is a planar mono c-Si solar cell, the second is a standard c-Si solar module, and the third one is a solar module with a textured encapsulation layer. In the end of this section the influence of the different angle dependent effects on the energy yield prediction of a standard solar module is given.

5.1 Overview of all of the angular effects on the *QE*

The simulations and measurements that were carried out for this thesis reveal a strong dependency of the EQE on the AOI. Even though most of the angular effects are reduced when the solar cells are encapsulated in glass or other encapsulation materials, they can still have a significant influence on the annual energy yield of the solar module.

Although similar results have been previously presented by other research institutes [21], a detailed analysis of all the effects that cause the angular dependency of the EQE is still not available. To effectively reduce angular loss mechanisms and to utilize effects which boost the performance at lower angles of incidence it is crucial to effectively separate the different mechanisms which play a role when the AOI is varied.

The most important angular effects, which were identified in this thesis, are presented in Table 5.1. These effects are similar to loss mechanisms, which have been systemically described in the literature [151, 152], but the main difference is that the effects described here are relative effects with respect to the case of perpendicular incidence. Most of these processes cause a reduction of the module's short circuit current density j_{sc}, but some also increase the j_{sc} with a variation in AOI, which is why they are intentionally referred to as effects and not as losses.

Table 5.1: Angular effects that influence the energy yield of a solar module

Effect 1	Geometrical cosine loss
Effect 2	Changing reflectance at the intersection of two media
Effect 3	Changing external light trapping of pyramidal structures
Effect 4	Changing internal light trapping inside one layer
Effect 5	Change in parasitic absorption
Effect 6	Changing generation profile inside the cell

In general, the effects can be grouped in optical and electrical effects, however only effect 6 belongs to the second group. It cannot be ruled out that the shape of the IV-characteristic is also influenced by a variation of the AOI, which would then also be part of the electrical effect. However, since only the QE and thus the short circuit current of the solar cells and modules were examined in this thesis, the effect on the voltage was neglected.

Due to the geometrical cosine effect, the incoming light is spread over a larger area; thus, the irradiance decreases by a factor of $cos(\theta_i)$, where θ_i is the angle of incidence. The cosine loss is a very strong effect, as might be realized by the fact that the irradiance is reduced by half at an incidence angle of 60°. The cosine loss can only be reduced by changing the orientation of the module relative to the sun (tracking) or by adding additional components such as mirrors to the photovoltaic system.

The second effect is the change of reflectance at the boundary of two materials. If an anti-reflective coating is applied between the media, the change of incidence angle not only changes the amplitude of the reflectance, but it is also causes a deviation in its spectral behavior [72].

Effect 3 describes the fact that photons, which are incident on a textured surface, will often intersect with the texture more than once. The number of intersections between the faces of the applied structures is generally dependent on the geometry of the textures and on the AOI. The process that involves multiple intersections in a texture is referred to as external light trapping here.

In contrast, effect 4 involves internal light trapping, which describes the trajectory of photons through the whole cell before they either escape or are absorbed. Here a distinction needs to be made between the light trapping inside electrically inactive layers (such as the glass cover) and the active semiconductor layer. While for the case of the non-active layers, light trapping is only preferred if the photons are subsequently led to the semiconductor layer. For the active layer a high light trapping performance is explicitly desired because it increases the probability of long wavelength photons to be absorbed in the semiconductor. This effect can be described with the help of the path length enhancement factor Z [133], which is however not taking into account the location of the absorption inside the semiconductor.

Parasitic absorption A_{Pa} (effect 5) refers to any mechanism in which an absorbed photon does not lead to the generation of an electron-hole pair [78]. These are the absorption in the module layers A_l except for the semiconductor (glass, EVA, back contact, back sheet), the absorption in the contact fingers and busbars A_{grid}, the free carrier absorption A_{FCA}, and the absorption in the anti-reflective coatings A_{AR}.

$$A_{Pa} = A_l + A_{grid} + A_{FCA} + A_{AR} \tag{150}$$

For the case of a solar cell without encapsulation, the variable A_l changes to A_{back} as the back contact is the only layer causing parasitic absorption.

The electrical process described by effect 6 is due to the changing trajectory of the photons through the semiconductor with the variation of AOI. The path variation of the photons is translated into a modification of the generation profile. As the IQE is a function of the generation profile, it will also be influenced by the variation of the incidence angle.

5.2 Defining angular correction factors

In the following sections, different angular correction factors are introduced that are used to describe the angular effects presented above. These angular correction factors are defined as the ratio of a reflection or absorption process X at a certain wavelength and AOI and the corresponding process at the same wavelength and perpendicular incidence. Thus, the general form for the angular correction factors is given by

$$f_X(\lambda, \theta_i) = X(\lambda, \theta_i)/X_0(\lambda) \tag{151}$$

At this point, only the angular correction factor for the EQE is presented as an example

$$f_{EQE}(\lambda, \theta_i) = EQE(\lambda, \theta_i)/EQE_0(\lambda) \tag{152}$$

where θ_i is the AOI on the modules or cells surface and the parameters with a zero in the subscript are the values for perpendicular incidence, which is equal to 8° here because of the fact that the reflection measurements cannot be performed at lower angles of incidence.

The angular correction factors are in particular used for two purposes.

1) Subtracting 1 from such an angular corrections factor gives the relative change of the corresponding effect that is caused by the variation of the AOI.
2) Using the angular correction factor, it is possible to correct the spectral curve of the corresponding process from the perpendicular case to the one at the AOI the factor was determined at.

Nevertheless, there are some limitations of the angular correction factors that need to be taken into account. As they are a function of the wavelength, they are strictly speaking not a correction factor, but a correction function.

If the accuracy of the angular correction factor needs to be high in terms of wavelength and AOI, the time consumption for the determination by means of ray tracing or measurement increases strongly.

Care needs to be taken in interpreting angular correction factors. Subtracting one gives a percentile deviation caused by the change of AOI, which might be high even though the absolute value of current change can be very small.

5.3 Angle dependent *EQE* and *IQE* of planar mono c-Si solar cells

To be able to effectively separate different processes from each other, it is meaningful to first choose a sample that has a simple structure. This is the reason why the angular effects are first investigated on a planar solar cell sample without encapsulation. In cases like this, the number of light paths is strongly reduced compared to randomly textured solar cells, which makes it possible to describe the processes by means of the analytical model that was presented in section 3.1. The results determined for the simple planar sample can subsequently be used to obtain a deeper understanding of the standard solar module.

The sample solar cell, which was investigated, was a planar solar cell that was provided by the Fraunhofer ISE-Freiburg. The solar cells were dedicated as "damage etched" meaning that the surface roughness caused by the wafer sawing was removed by means of a KOH etching procedure. The parameters characterizing the solar cell are presented in Table 5.2.

Table 5.2: Cell parameters of the planar solar cell under investigation

Parameter description	Symbol	Units	Values
Total cell area	A_c	cm²	150
Short circuit current density	j_{sc}	mA/cm²	33.65
Open circuit voltage	V_{oc}	mV	605
Fill factor	FF	%	68.37
Efficiency	η	%	13.9
Thickness of AR-coating	d_{AR}	nm	86
Emitter and base minority diffusion length	L_e/L_b	µm	12/200
Surface recombination velocity (front/ rear)	S_f/S_r	cm/s	1e4/800
Total cell thickness	W	µm	200
Emitter thickness	W_e	µm	0.3
Donor and acceptor concentration	$N_D/\ N_A$	1/cm³	1e17/1e20
Area share of busbars, fingers and cell	$M_{bb}/M_{fi}/M_c$	%	0/6.47/93.53
			Sources:
AR-coating material (n and k)	$SiNx$		[153]
Semiconductor material (n and k)	Si		[154]
Back contact material (n and k)	$AlSi$		[116]
Finger material (n and k)	Ag		[155]
Glass (low-iron Starphire) (n and k)	$Glass$		[156]

While some of the parameters were provided by the institute from which the cells were sponsored (W, N_D, N_A), the material parameters were taken from the literature as indicated in Table 5.2. Other values taken from the literature were L_e and W_e [67]. Using these two values, the value of S_f was determined by a fitting procedure of the EQE curve. The parameters L_b and S_r were determined using the measured perpendicular IQE curve and the procedure described in [74].

The values of the total cell area and the shares of busbars, fingers and the solar cell were determined by reflected light microscope imaging using equations (95) to (97).

The thickness of the anti-reflective coating d_{AR} was determined by a fitting procedure of the measured reflection curves. The best fit for the reflection curves at five different AOI can be seen in Fig. 5.1. It is important to note that the choice of the material parameter of the AR-coating is very crucial for the determination of the coating thickness. The parameters n and k of SiN_X can be tuned by the composition of its two elements [157]. Since this composition could not be determined for the sample under investigation, one was chosen which provides typical values [116]. Once the material parameters are selected, the subsequent fitting procedure is relatively straightforward and leads to a thickness value of 86 nm for the AR-coating of the sample.

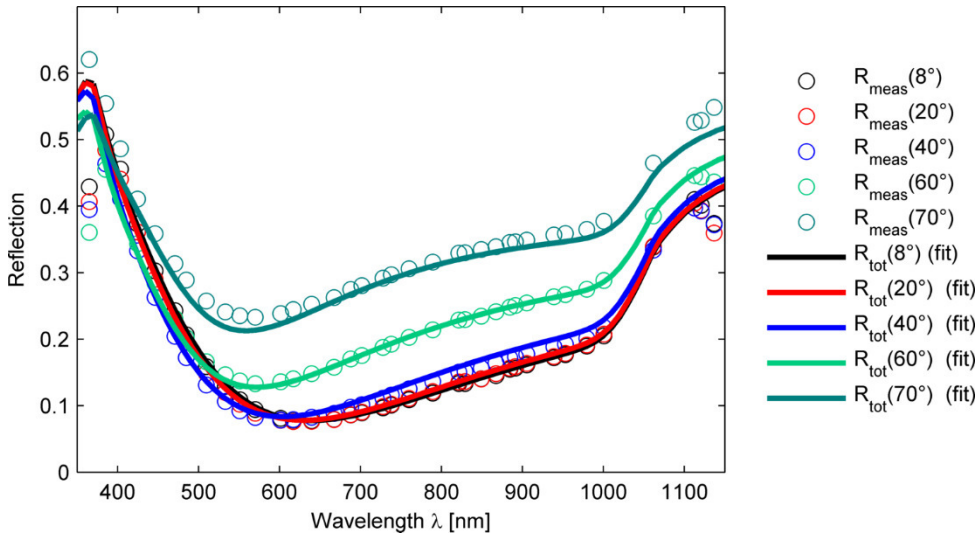

Fig. 5.1: Measured reflection curves (circles) and fitted functions using the analytical model (lines) of a planar c-Si solar cell

The reflection curve has two regimes, namely the external R_{ext} and the escape reflection R_{esc}. The escape reflection increases the reflection curve at values > 1000 nm for the investigated cell. The characteristic of the escape reflection is determined by the cell thickness and the reflection properties of the front and rear side of the solar cell. The reflection properties are described by the reflectivity of the direct light, the share of light that is randomly reflected (haze factors h_f and h_b) and the reflectivity of diffuse light on the surface ($R_{b,d}$ and $R_{f,d}$). While the reflection of the direct light is entirely determined by the Fresnel equations, the parameters for the haze and the reflectivity of diffuse light can be determined by a two step procedure.

First the reflectivity of diffuse light on the solar cells internal surfaces is determined. A numerical approach, which was derived for this thesis, was used to determine the diffuse reflectivity. The derivation can be found in Appendix C. These values are inserted into the analytical reflection model of section 3.1 so that the values of the haze parameter at the front and the back side can be found by fitting the simulated curve to the measured.

For the back side of the planar solar cell under investigation, which consists of an eutectic layer of silicon and aluminum (AlSi), a diffuse reflectivity $R_{b,d} = 0.81$ was determined by the method in Appendix C. For the front side, which consists of a stack of the three materials Si, SiN_x, and air, a diffuse reflectivity of $R_{f,d} = 0.97$ was determined. This high value resulted because the escape cone for photons is narrow, which led to a high share of total internal reflection.

After the subsequent fitting procedure, the two haze values $h_f = 0.1$ and $h_b = 0.5$ were determined and found to be adequate values.

In graph a) of Fig. 5.2, the current that is lost due to reflection at five different AOI (8°, 20°, 40°, 60°, 70°) for a standard AM 1.5 spectrum (global radiation) is plotted. While for the angles of 20°, 40° and 60° an absolute reduction of the current loss compared to the reflection loss at 8° can be seen at wavelengths < 520 nm, the loss current is higher for all wavelengths >600 nm. Very high losses due to the angular variation can be observed for the case of 70° AOI for nearly all wavelengths.

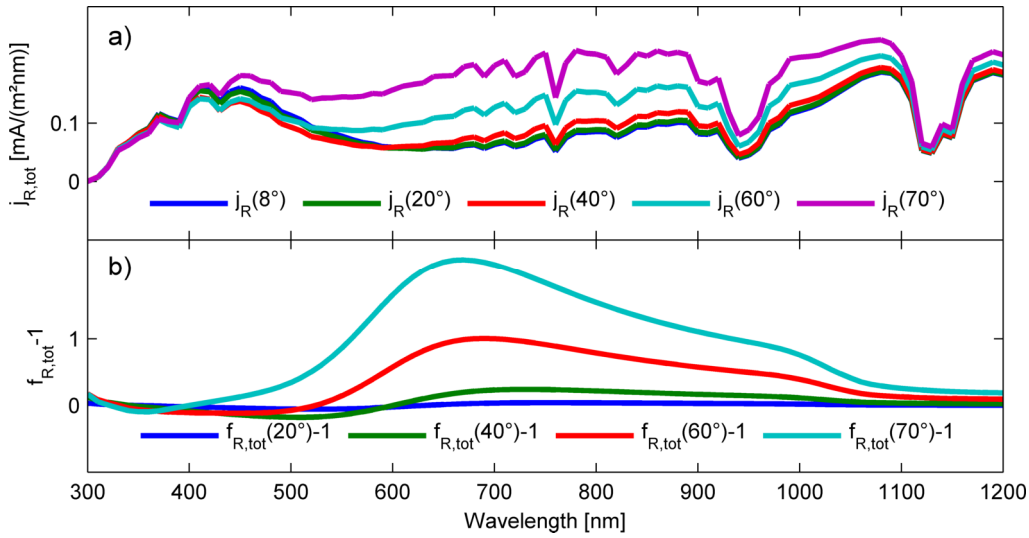

Fig. 5.2: Simulated loss of current density due to reflection on a planar c-Si solar cell (a), and corresponding angular correction factors (b)

The comparison can also be done using the corresponding angular correction factor subtracted by one ($f_{R,tot} - 1$). The results can be seen in graph b) of Fig. 5.2. A strong relative increase of reflection, which reaches more than 240% relative at a wavelength of 670 nm, can be observed. On the other hand, there is a decrease in reflectivity in the low wavelength region for all angles of incidence. In the NIR-region, a slight increase in reflection (1.6 % for 70° AOI at 1200 nm).

The factor $f_{R,tot}$ reveals the strong angular dependence of the SiN_x AR-coating applied to the surface of the solar cell. Of course, this effect will strongly change when the cell is encapsulated beneath, e.g., glass and EVA, but the effect still is relevant, as will be seen below.

The angular effect on the reflectivity strongly influences the EQE of the solar cell. The simulated and the measured $f_{EQE} - 1$ curves for several AOI are plotted in Fig. 5.3.

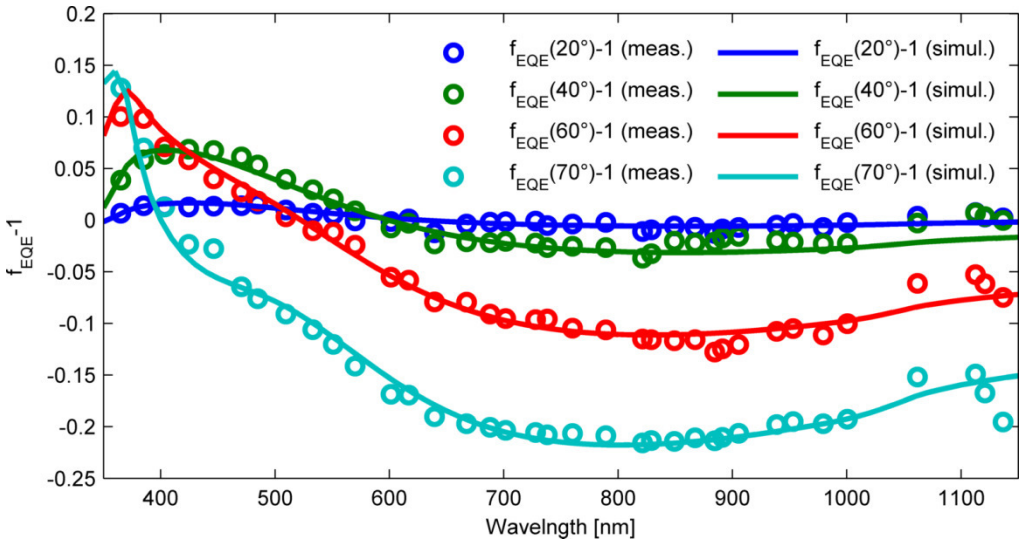

Fig. 5.3: Measured and simulated curves of $f_{EQE} - 1$ for a planar mono c-Si solar cell sample

A very good fit can be observed for all wavelengths up to 1000 nm. For the measurement point at 1062 nm the simulation is underestimating the f_{EQE} for all wavelengths. And for even longer wavelengths the measurement is showing a kink in that is not reproduced by the simulations. However, the comparison verifies the principle validity of the analytical model. Now the different absorption mechanisms incorporated into the EQE will be analyzed in greater detail.

5.3.1 Angle dependence of parasitic absorption processes

Even though there is a strong influence of the reflectivity on the f_{EQE} curves, it is not the only relevant effect. The simulation reveals the influence of the different parasitic absorption processes. The loss currents due to the four parasitic absorption processes for 8° and 70° are plotted in the upper four graphs (a to d) of Fig. 5.4. These are the absorption by the AR-coating, by the contact grid, by the back side layer and by free carriers respectively. The four graphs in the middle (line e to h) show the same processes in terms of absorption. The lower graphs (i to l) show the corresponding correction factors reduced by one.

For the parasitic absorption by the AR-coating, a relatively low loss current can be observed. When the AOI is changed from 8° to 70°, the absorption in the low wavelength range increases, while it decreases in the wavelength region between 450 nm and 1100 nm. The absorption by the grid (here only the contact fingers are included) is also relatively low concerning the loss current. But there is a clear angular effect that decreases the absorption at wavelengths < 500 nm whereas it increases for higher wavelengths.

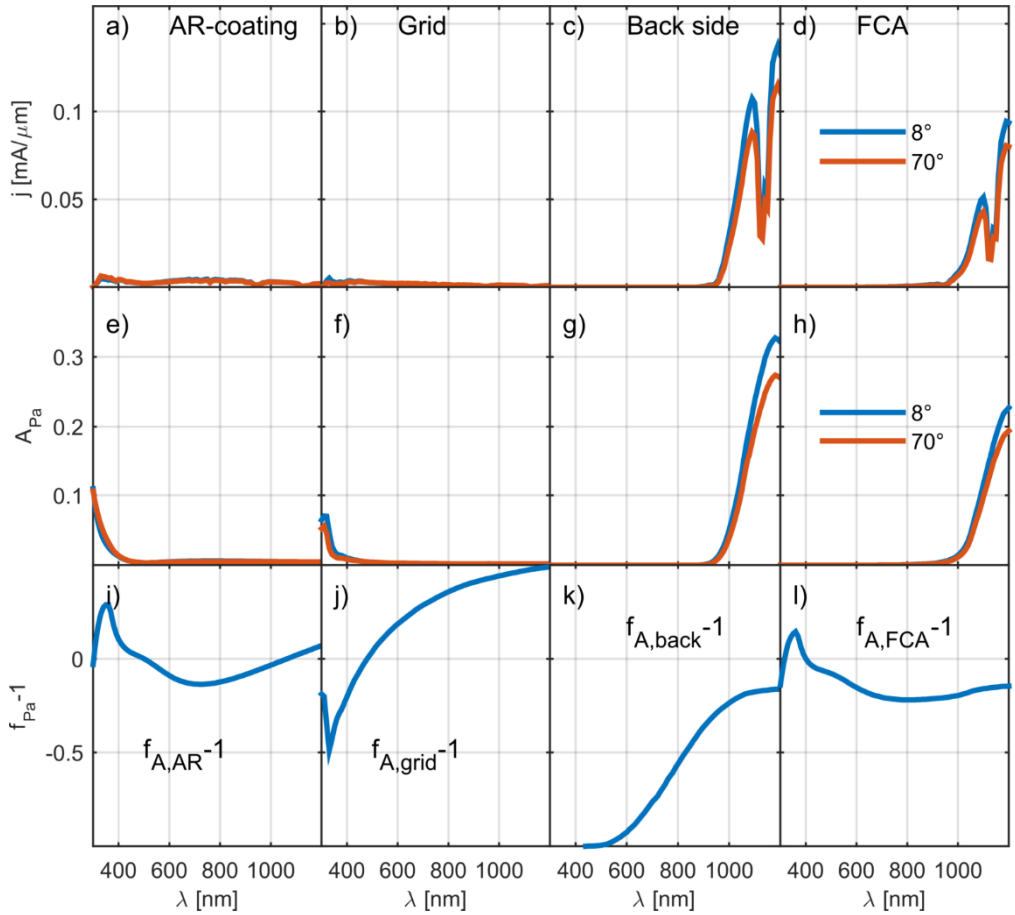

Fig. 5.4: Four different parasitic absorption processes. a) to d) current densities of absorption processes at AOI of 8° and 70° using AM 1.5 spectrum. e) to h) Absorption due to the four parasitic absorption processes at 8° and 70°. i) to j) corresponding angular correction factors subtracted by one

The parasitic absorption of photons by the back side contact layer is an important loss mechanism in absolute and relative terms, as can be seen in graphs c) and g). At the same time, the process is strongly angle dependent. The parasitic absorption decreases with increasing AOI as the reflection on the back side simultaneously increases. However, this graph of the angular correction factor $f_{A,back} - 1$ needs to be analyzed with care, as it gives very high negative values for low wavelengths, even though there are barely photons with these wavelengths reaching the back side of the cell.

The parasitic absorption, which is caused by free carriers also causes a significant loss of current as can be seen in d) and h) of Fig. 5.4. Changing the AOI from 8° to 70° results in a relative increase of absorption for wavelengths < 400 nm, which however does not result in significant current losses. The reduction of absorption in the wavelength region > 1000 nm in contrast leads to a reduction of current loss due to FCA. This reduction can be explained by the fact that due to the longer light path of long wavelength photons less of these photons experience multiple intersections with the emitter, where the main free carrier absorption takes place because of the high doping concentration.

5.3.2 Analyzing the angle dependence of the *IQE*

A central purpose of this thesis is to answer the question to which extent the IQE of a solar cell or module changes with the variation of AOI. The planar mono-crystalline Si solar cell investigated in this section is very suitable for answering this question because the application of a texture generally introduces many additional photon paths through the cell which makes it more difficult to clearly distinguish the different effects involved.

First of all, it is important to recall the different definitions of the IQE that were presented in section 2.5. The definition given by (81) is the one that purely includes the electrical effects and thus will be used for the following analysis. The angular correction factors $f_{IQE} - 1$ are plotted for 20°, 40°, 60° and 70° in Fig. 5.5. The curves have a global minimum at a wavelength of 420 nm and a global maximum at around 950 nm.

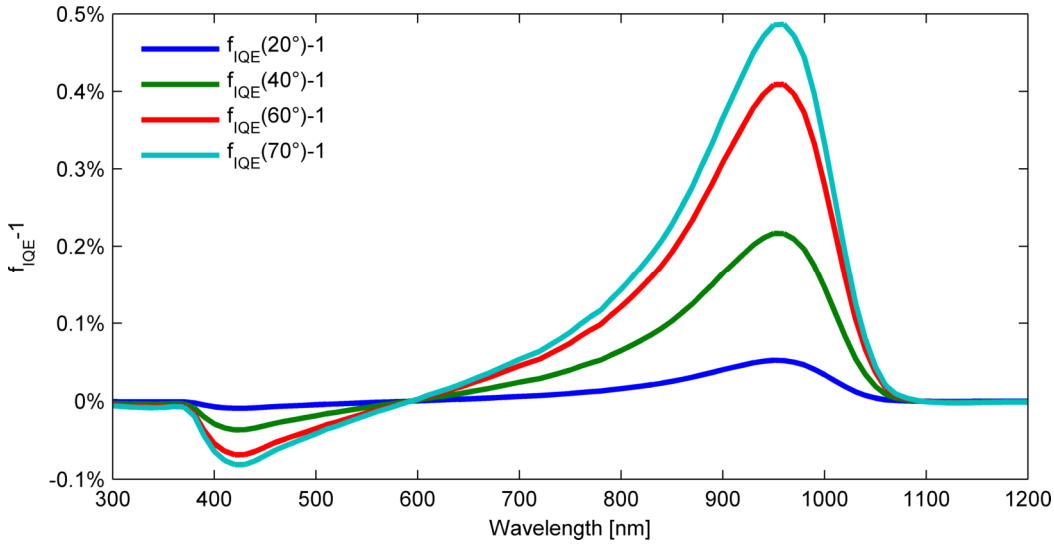

Fig. 5.5: Simulated curves of $f_{IQE} - 1$ for a planar c-Si solar cell

The shape of the minimum is mainly determined by the thickness of the emitter W_e, its diffusion length L_e, and the front side recombination velocity S_f. The maximum is determined by the total thickness of the cell W, the diffusion length of the base L_b, and the rear surface recombination velocity S_r. The following analysis focuses on the effect of the maximum as it is more pronounced. Reducing the total thickness of the cell makes the graph shift to lower wavelengths and simultaneously reduces the maximum value of the function. In contrast, the influence of L_b and S_r is strongly interdependent. This can be demonstrated plotting the maximum value of $f_{IQE}(70°) - 1$ as a function of L_b and S_r in a contour plot (Fig. 5.6).

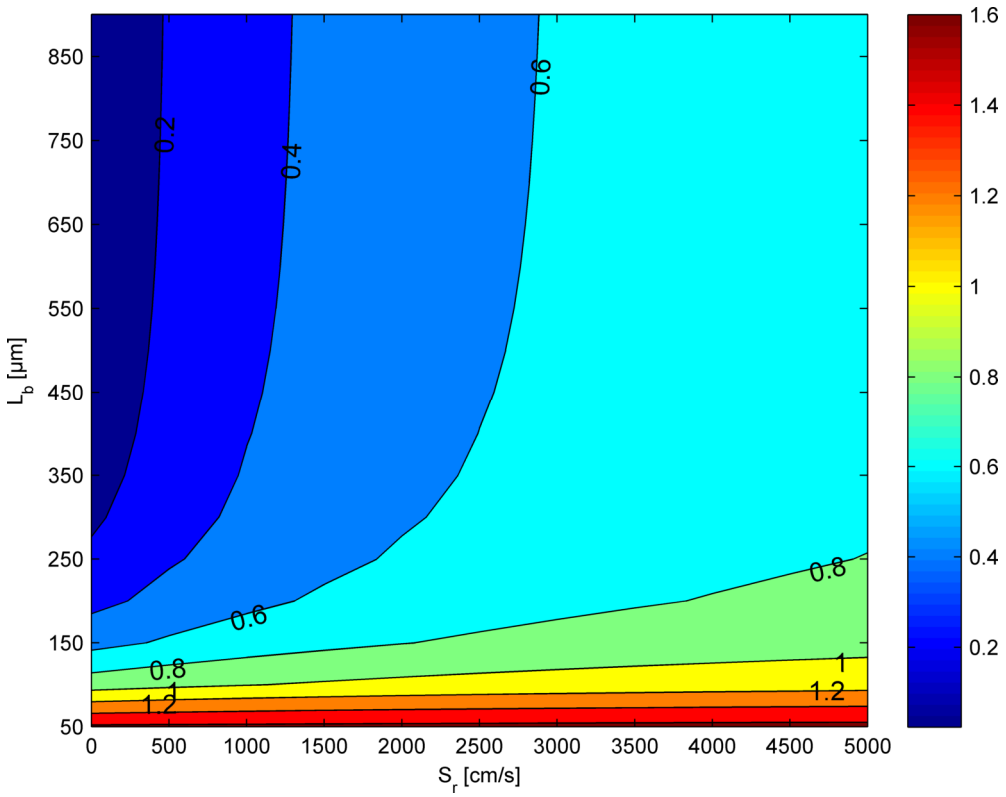

Fig. 5.6: Maximum value of $f_{IQE}(70°) - 1$ as a function of base minority carrier diffusion length L_b and rear surface recombination velocity S_r

It can be seen that for very low diffusion lengths < 100 μm, the effect is nearly independent of the rear surface recombination velocity. For very high diffusion lengths > 450 μm, the effect is not dependent on the diffusion length but is dominated by S_r.

To fully understand the effect of the angular dependence of the IQE, it is meaningful to illustrate the photon path at perpendicular incidence and at a higher AOI as in Fig. 5.7. The diffusion length of the base L_b and the rear surface recombination velocity S_r are indicated schematically. Looking at case a) in the figure it becomes apparent that the absorption of the photon that is indicated by the black arrow took place closer to the surface in the case of the high AOI and is now within reach of the diffusion length. At the same time, the generation of the electron-hole pair occurred further away from the back side and hence the impact of S_r is reduced. However, for the case b) when the photon is reflected from the back side, the effect can be turned around as now the absorption charge carriers are created closer to the rear surface and further away from the collecting junction.

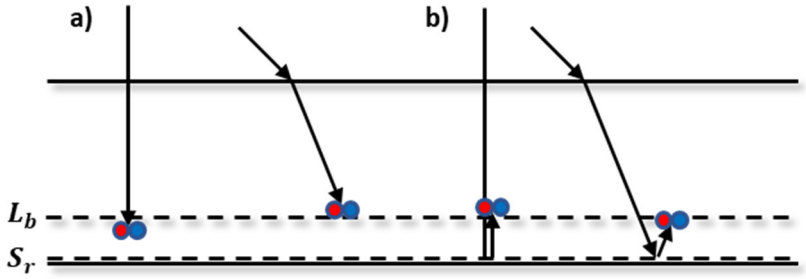

Fig. 5.7: Illustration of the variation of AOI and its influence on the position where the electron-hole pair is created. a) Generation closer to the top surface due to angle variation and thus potentially within the diffusion length of the base. b) Generation further away from the top surface.

However, even though the effect described in case b) in Fig. 5.7 counterbalances the angular effect in a certain wavelength regime, it does not explain why the graph of $f_{IQE} - 1$ drops to zero for wavelengths > 1100 nm. This reduction is caused by the fact that due to the low absorption, the long wavelength photons traverse the cell multiple times; thus, the location of their absorption is entirely randomized over the depth of the cell. Hence a variation of the AOI does not have any influence on the generation profile.

Process a) in Fig. 5.7 can be modeled assuming a solar cell with infinite thickness or $W \gg L_b$. For this assumption, it was shown by Paul Basore [70] that the IQE can be written as

$$\frac{1}{IQE(\theta)} = 1 + \frac{\cos(\theta)}{\alpha \cdot L_{eff}(\theta)} \tag{153}$$

where the effective diffusion length L_{eff} incorporates L_b, S_r and the width of the base region W_b.

$$L_{eff}(\theta) = L_b \cdot \frac{1 + \frac{S_r L_b}{D_n} \tanh\left(\frac{W_b}{L_b}\right)}{\frac{S_r L_b}{D_n} + \tanh\left(\frac{W_b}{L_b}\right)} \tag{154}$$

For the infinite base model of f_{IQE} developed here it was found that the base width needs to be additionally corrected by the cosine of the AOI.

$$L_{eff}(\theta) = L_b \cdot \frac{1 + \frac{S_r L_b}{D_n} \tanh\left(\frac{W_b/\cos(\theta)}{L_b}\right)}{\frac{S_r L_b}{D_n} + \tanh\left(\frac{W_b/\cos(\theta)}{L_b}\right)} \tag{155}$$

Using (153) the angular correction factor $f_{IQE} - 1$ can be determined for the case of an infinite base.

$$f_{IQE}(\theta) = \left(1 + \frac{\cos(8°)}{\alpha \cdot L_{eff}(8°)}\right) / \left(1 + \frac{\cos(\theta)}{\alpha \cdot L_{eff}(\theta)}\right) \tag{156}$$

This function is plotted in comparison to the $f_{IQE} - 1$ of the full analytical model for three different diffusion lengths in Fig. 5.8. The fitting function fits the full analytical model up to the point where the inflection point of the letter is located. It is worth mentioning that

the intersection point of function (156) is found by making α approach zero. The resulting equation is given by

$$\lim_{\alpha\to 0}\left(1+\frac{\cos(8°)}{\alpha\cdot L_{eff}(8°)}\right)/\left(1+\frac{\cos(\theta)}{\alpha\cdot L_{eff}(\theta)}\right)=\frac{\cos(8°)\cdot L_{eff}(\theta)}{\cos(\theta)\cdot L_{eff}(8°)} \tag{157}$$

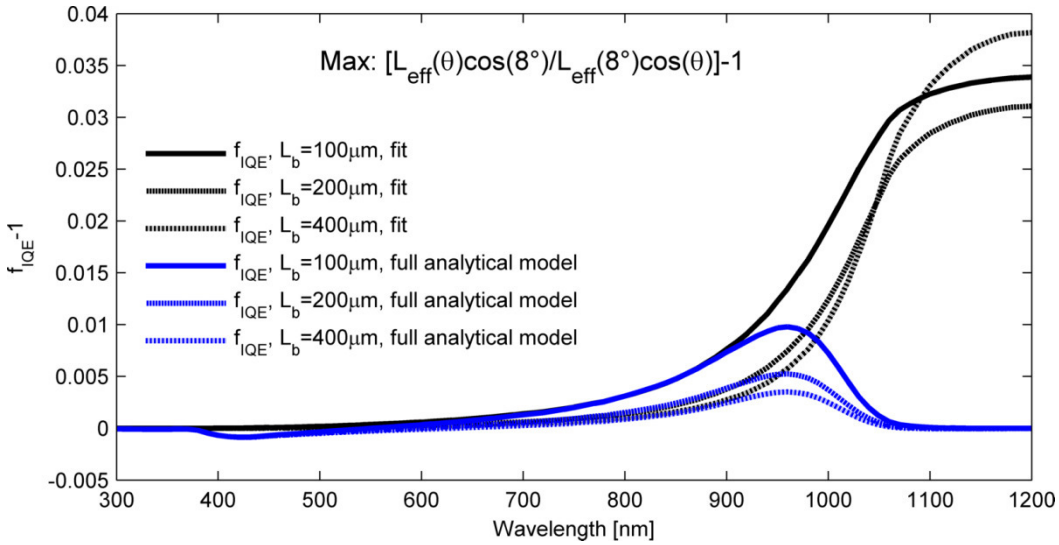

Fig. 5.8: Comparison of the $f_{IQE}-1$ determined by the analytical model and the one for the infinite base which is given by equation (156)

It was not possible in the scope of this thesis to derive a simple analytical equation for the descending part of $f_{IQE}-1$ as effect b) of Fig. 5.7 and the randomization of the absorption location simultaneously act on the IQE. However, using (156) the upper boundary of the f_{IQE} can easily be determined for different values of L_b, S_r and W_b.

The measurement of the angle dependence of the IQE involves angular measurements of the EQE as well as the angular hemispherical reflectance. As the parasitic absorption processes in the solar cell cannot be distinguished from the desired absorption in the semiconductor, another definition of the IQE needs to be used for the comparison of the measurements and the simulations. The corresponding definition is given by equation (82), where the measured IQE is refered to as IQE_{meas} and the simulated one as IQE^*.

The results of the measurements and the simulations are presented in Fig. 5.9. It can be seen that there are strong similarities concerning the shape of the simulation and the measurements. However, the measurement values are higher by a factor 4 concerning regarding the wavelength regions of interest. As the measurements are reproduceable there are only three possible reasons for the higher measurement values compared to the simulation. Either a systematic measurement error is occurring, the measurements are deviating due to non-ideal cell parameters (rough surfaces, deviating optical parameters etc.) or the lack of a physical effect in the simulation is the reason for the discrepancy. Because despite intense investigations, none of these factors could be identified, the measurement results shell be analyzed qualitatively here.

The simulations show an increase of the IQE at wavelengths > 850 nm. The measurements also show a comparable increase for the curves of $f_{IQE,meas} - 1$ for the AOI 20°, 60° and 70°, while the one for 40° increases up to 900 nm and subsequently decreases for higher wavelengths.

The simulation reveals a decrease in the IQE in the wavelength range from 420 nm to 820 nm that can be attributed to the increasing absorption in the AR-coating at higher AOI. This effect cannot be clearly identified in the measurements.

The simulated as well as the measured curves for the incidence angles of 60° and 70° show a local maximum in the wavelength region of 950 nm to 970 nm, which might be related to the increasing collection of charge carriers due to the closer absorption to the collecting junction.

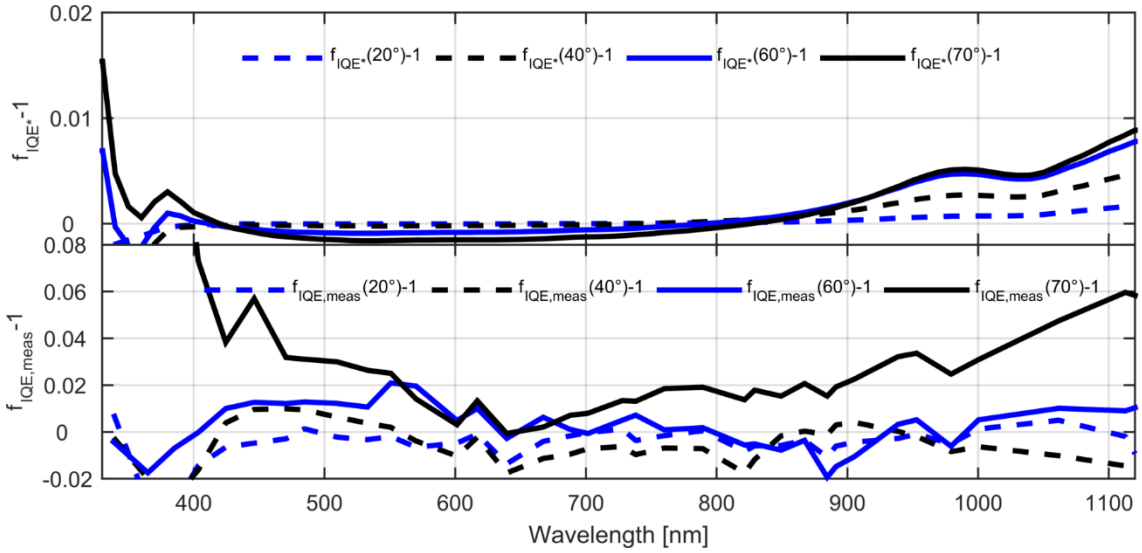

Fig. 5.9: Simulated values of $f_{IQE^*} - 1$ (upper graph) in comparison to the measured curves of $f_{IQE,meas} - 1$ (bottom graph)

The simulations also show an increase of the IQE in the wavelength range < 400 nm for the incidence angle of 70°. The measurements show an increase as well, which however is much more intense and includes all wavelengths < 600 nm.

It can be summarized that the simulations reveal an increase of the IQE as a function of incidence angle for planar mono-c-Si solar cells. This effect is also strongly depending on the factors W_b, S_r and L_b but for planar solar cells generally does not surpass a peak value of 1%. The measurements did show similarities to the simulations, but these could not be reliably attributed to the described physical effects.

5.4 Angle dependent *EQE* and *IQE* of a standard c-Si solar module

To identify the different mechanisms that affect the performance of a solar cell when the AOI is varied, it is useful to perform simulations and measurements on a planar solar cell, which was done in the section above. But as virtually all solar cells that are sold on the

market have a textured front surface, it is necessary to include the effect of textured surfaces into the discussion of angular dependence of solar cells and modules.

5.4.1 Emulation of the *IQE* beneath a textured surface

In the section above, it was explained that the variation of the AOI leads to an absorption closer to the collecting junction, which increases the overall collection efficiency and thus the IQE of the light in a certain a wavelength range. If a texture is implemented on the top surface of the solar cell, this effect can be even higher as can be shown for the simple case of a texture consisting of pyramidal grooves with a base angle of 45°. The paths of perpendicular and 45° light incidence are schematically shown in Fig. 5.10 for the case of a planar surface and the 45° pyramidal texture groove. For both cases, the angle variation inside the semiconductor is equal to about 10.5° if a refractive index of 3.9 (silicon) in an ambient medium with refractive index of 1 (air) is chosen. However, regarding the reduction of absorption depth Δz, a huge difference can be observed.

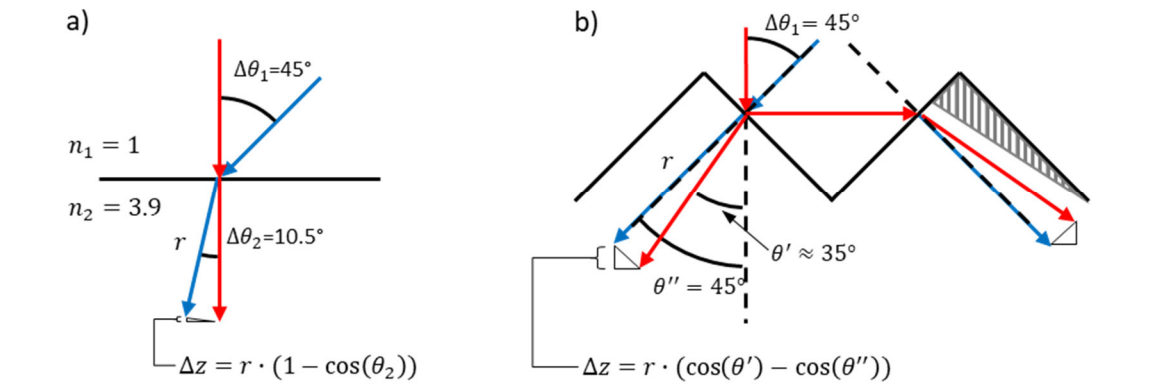

Fig. 5.10: Illustration of the lightpaths in a solar cell with a) a planar cell surface and b) a textured surface consisting of 45° base angle grooves. The AOI is varied between 0° and 45°. The variable Δz is giving the shift of absorption in direction to the collecting junction.

The equations to determine Δz for both of the cases are also given in Fig. 5.10. While for the planar cell $\Delta z = 0.017$ for an arbitrary path length of $r = 1$, for the case of the textured surface $\Delta z = 0.112$ and thus is much higher for the latter.

The pyramidal structure is chosen so that for the case an incidence angle of 45°, the photons are all transmitted through the semiconductor with an angle of 45°. For the case of perpendicular incidence, two transmission angles need to be taken into account, which are 35° and 55° as can be seen in graph b) of Fig. 5.10. Using the simple Fresnel equation (22), it is found that 1/3 of all incident photons on the face of the pyramid are reflected to the face of the neighboring pyramid. Considering the photons that are then transmitted into the semiconductor on finds that 82% of these have a transmission angle of 55°, and 18% of them are internally reflected to the angle of 35° (this region is indicated with gray lines in Fig. 5.10).

An effective transmission angle θ_{eff} is defined as the mean angle of all photons being transmitted through the semiconductor

$$\theta_{eff} = p_1 \cdot \theta_1 + p_2 \cdot \theta_2 + \cdots = \sum_{v=1}^{N} p_v \cdot \theta_v \tag{158}$$

where p_v is the share of photons transmitting through the semiconductor with a specific angle and N is the total number of different photon paths. It is important to note that using the effective angle is just an approximation concerning the absorption and transmission inside the semiconductor. This approximation is given by

$$\begin{aligned} &\exp\left(-\alpha \cdot \frac{W}{cos(\theta_{Eff})}\right) \approx p_1 \cdot \exp\left(-\alpha \cdot \frac{W}{cos(\theta_1)}\right) \\ &+ p_2 \cdot \exp\left(-\alpha \cdot \frac{W}{cos(\theta_2)}\right) \\ &+ \cdots + p_N \cdot \exp\left(-\alpha \cdot \frac{W}{cos(\theta_N)}\right) \end{aligned} \tag{159}$$

Using this definition, an effective angle of $\theta_{eff} = (2/3 \cdot 35° + 1/3 \cdot 2/3 \cdot 0.82 \cdot 55° + 1/3 \cdot 2/3 \cdot 0.18 \cdot 35°)/0.89 = 39.1°$ is found for the 45° pyramidal groove structure at perpendicular incidence. The effective angle for 45° AOI is of course 45°.

These effective angles can now be used to determine the angular correction factor $f_{IQE} - 1$ using the analytical model which was employed for the simulations of the planar solar cell in the section above. All values are kept identical to the ones that were derived and presented for the planar cell except for the internal front side reflection, which was set to zero to only allow one transmission through the wafer.

The results of the texture emulation are plotted in Fig. 5.11. The angular effect on the IQE excluding parasitic absorption is 1.4 % at its maximum at a wavelength of 970 nm, which is much higher than the effect that was simulated for the planar solar cell (Fig. 5.5). If the parasitic absorption is included a strong increase of the IQE^* at long wavelengths can be observed when the angle of incidence is changed from 0° to 45°.

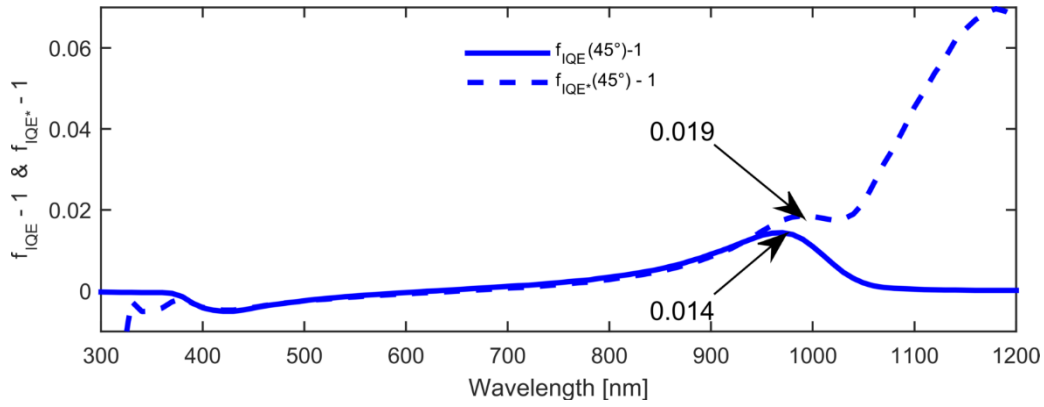

Fig. 5.11: Emulated curves for $f_{IQE} - 1$ and $f_{IQE^*} - 1$ for a textured solar cell with 45° base angle grooves.

This example was presented to clearly demonstrate in which way the implementation of a texture boosts the angular dependency of the IQE. In the following, the effects of the AOI variation will be investigated for a standard solar module.

5.4.2 Angular dependence of the *EQE* of a standard silicon solar module

The sample type that is investigated in the following consists of a randomly textured c-Si cell, which has equivalent electrical properties to the ones of the planar solar cell investigated above Table 5.2. The sample type will be referred to as 'standard module' even though the front side encapsulation does not consist of a glass layer but of a 100 μm thick transparent PVDF polymeric film. This choice was made because systematic measurement errors caused by the thickness of the encapsulation material can be reduced by replacing a thick glass cover with a thin polymeric film. These are for example the entrance of light from the side of the sample at low AOI and the displacement of the light spot with the variation of the AOI. A source of error would also be the fact that for the EQE measurements, the sample is positioned on top of the measurement stage and for the angular reflection measurements, it is placed into the sample holder from the back side. For a thick glass cover, this would lead to difficulties in the determination of the IQE because the same measurement spot on the cell could hardly be adjusted. Unfortunately, no optical data was available for the encapsulation film, which is why the optical parameters of a low iron Sodalime glass cover [156] were chosen instead for the simulations. This might have led to an underestimation of the absorption in the UV-region of the spectrum.

The back side of the module consists of a standard Tedlar® back sheet, beneath which a stabilizing plate of aluminum is located.

Investigating the angle dependence of the EQE of a standard solar module, the choice of the measurement setup crucial. Significant differences can be seen if the sample is measured under a light field that is larger than the sample compared to a measurement setup in which only a small light spot is incident on the solar cell or module.

For the case of a large light field, the surrounding of the solar cell such as the back sheet can significantly influence the measured current at the AOI under investigation. This is also the main reason for the difference in the results for a standard solar module which were presented by Geisemeyer et al. [21] and Plag et al. [22]. While the latter presents an increase of the f_{EQE} and thus a relative super-cosine response for the infrared region at angles below 65°, this effect does not occur in the measurements given by Geisemeyer et al.

For this thesis, most of the measurements were performed in the configuration using a small light spot because of the fact that for the determination of the angular IQE, the angular reflectivity measurements needed to be performed, which are only feasible in the small spot configuration.

However, the standard solar module was also measured in the large light field configuration to compare it to the angular EL measurement. The latter had to be determined from a larger distance as explained in section 4.4.

The comparison between the $f_{EQE} - 1$ determined by the angular spectral response measurement (filter monochromator setup) and the angular EL measurement (spectrometer setup as described in 4.4) for the angle of 60° can be seen in Fig. 5.12 b).

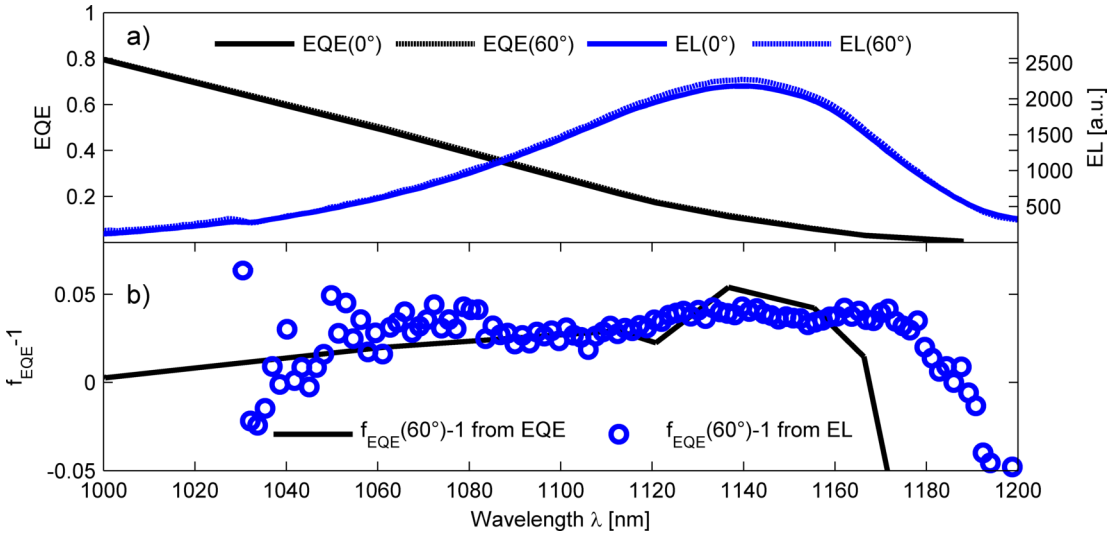

Fig. 5.12: a) EQE and EL curves of a standard solar module for the incidence angles of 0° and 60°. b) Comparison of the $f_{EQE}(60°) - 1$ curves determined by EQE and EL measurements.

The measurement shows a good agreement of the two measurement techniques for the wavelength range between 1080 nm and 1160 nm. For lower wavelengths, the measurement accuracy of the EL measurement is decreasing such that the measurement values are not reliable anymore. For the wavelength region > 1160 nm the $f_{EQE} - 1$ curves are strongly diverging. Because of the stronger signal of the EL measurement it probable that these values are more reliable than the ones that were measured with the help of the filter monochromator setup. The reason for the results being >0 could not be identified in this thesis. It is assumed that it is caused by either a boost in photon collection by the back sheet or due to the entering of light at the edge of the module.

For the case of the $f_{EQE} - 1$ determination using the configuration with a small light spot, the values are all smaller than 0 as can be seen in Fig. 5.13. Even though the spectral dependence is not as pronounced as it was the case for the planar solar cell without encapsulation, the effect is still significant. The value of $f_{EQE}(60°) - 1$ at 821 nm is -8.6% and at 1062 nm it is -5.2% making a difference of 3.4% between these two spectral points.

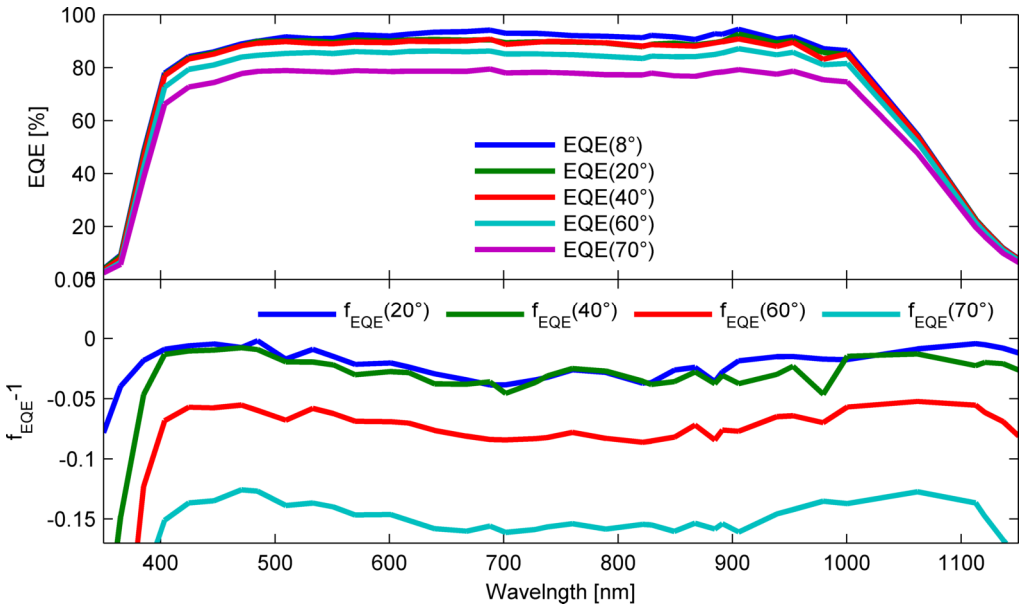

Fig. 5.13: EQE curves for different AOI of standard solar module sample (upper graph) and the corresponding corrections factor $f_{EQE} - 1$ (lower graph)

Again, the question arises as to which processes rule the angular dependence of the EQE in the case of a standard solar module. For this purpose, a ray tracing simulation was performed for different AOI. It is meaningful to define currents for the different optical processes that are involved. The photocurrent provided by the global solar spectrum with AM 1.5 is about 44.1 mA/cm^2 (for the silicon bandgap of 1.1 eV), which is hence the sum off all processes involved. The eight different processes that can be simulated with the ray tracing software SMARTI are exemplarily presented in the upper graph of Fig. 5.14 for the incidence angles of 8° and 70°. The FCA is not included in the SMARTI software.

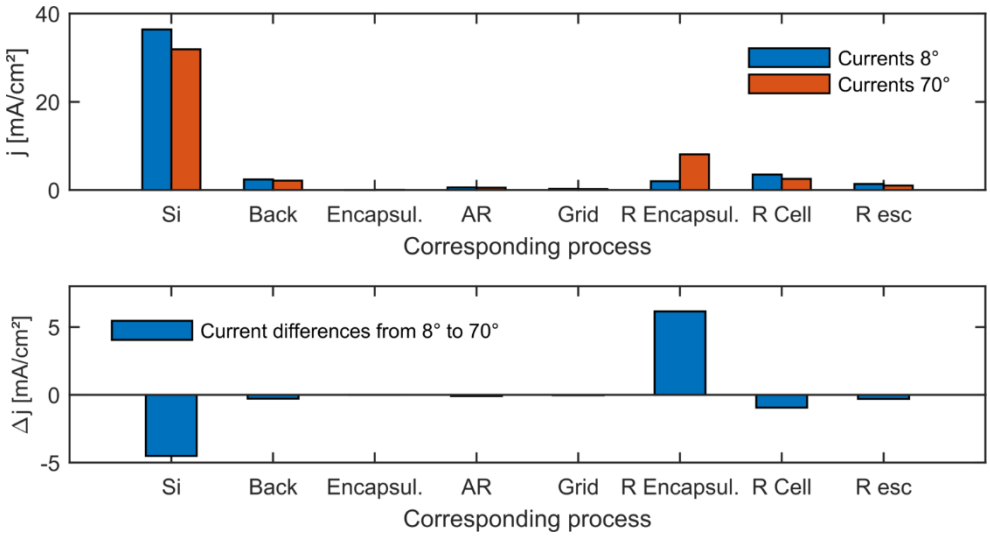

Fig. 5.14: Absorption and reflection current densities of a standard solar module at 8° and 70° AOI (upper graph) and the corresponding differences (lower graph)

The resulting differences in current density of the corresponding processes due to the angle variation are presented in the lower graph of Fig. 5.14. The total sum of these current

differences need to result in zero. A strong reduction of the absorption of photons in the silicon layer can be observed, which is mainly due to the increase of reflection on the external encapsulation surface. The angular dependence seems to be negligible for the parasitic absorption processes in the encapsulation layer, the AR coating and the contact grid. But care need to be taken interpreting these values. The currents of these three processes are certainly reduced by the fact that more photons are reflected at the external interface, which would lead to a negative Δj value. As the values are close to zero, that means that a counterbalancing increase of the currents resulting from these processes occurs.

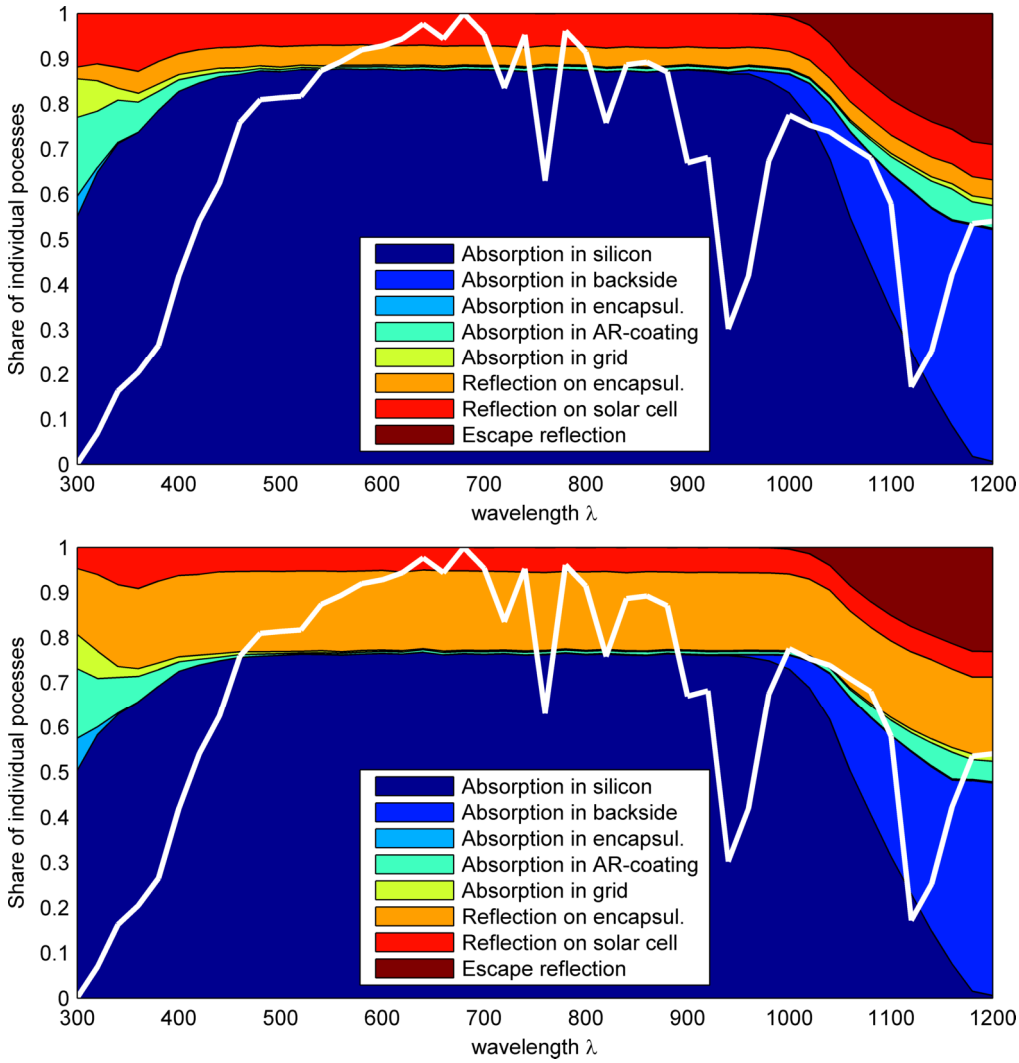

Fig. 5.15: Share of the absorption and reflection processes in a standard solar module for 8° (upper graph) and 70° (lower graph). The white line shows the normalized solar spectrum AM 1.5.

Moreover, the total current as well as the relative current deviation due to the AOI are strongly dependent on the radiation spectrum, which is incident on the sample. To illustrate this, the relative processes are plotted in Fig. 5.15 for the incidence angles of 8° and 70°. The white line in both graphs shows the normalized photon density of the AM 1.5 spectrum. Looking at the absorption inside the encapsulation layer, an increase in the UV-

region can be observed; which however results in a very small current, because of the low photon density.

5.4.3 Angle dependence of the *IQE* in a standard silicon solar module

As it was shown in the previous section, the number of photons absorbed inside the silicon layer decreases when the AOI is increased. However, the question remains open if the variation of the AOI results in a changing generation profile, which could then lead to a changing IQE. The analysis will be done below by using the SMARTI ray tracing software. However, an alternative approach will first be presented applying the concept of effective angles that was defined above by (158).

First, all light paths, which occur inside the silicon wafer after the light is transmitted through the textured cell surface, were determined with the help of the SMARTI ray-tracer. Three basic simplifications were used for the simulation. First, the transmission angles were all determined for a wavelength of 550 nm. This wavelength was chosen because it is generally used as an average representation for the whole solar spectrum. Second, the ray was stopped from further interaction directly after it transmitted inside the silicon wafer. Hence the internal reflection inside the texture was neglected. The error caused by this effect is assumed to be low for a pyramid base angle of 54.74°. The third simplification is that the simulated texture was chosen to be regular and not random.

On the left-hand side of Fig. 5.16 the share of the different possible angles of transmission are plotted for the incidence angles 8° and 70°. While for perpendicular incidence (8°) the transmission angle of 36.8° is dominant followed by 60.6°, the overall distribution of different angles increases for an incidence angle of 70°.

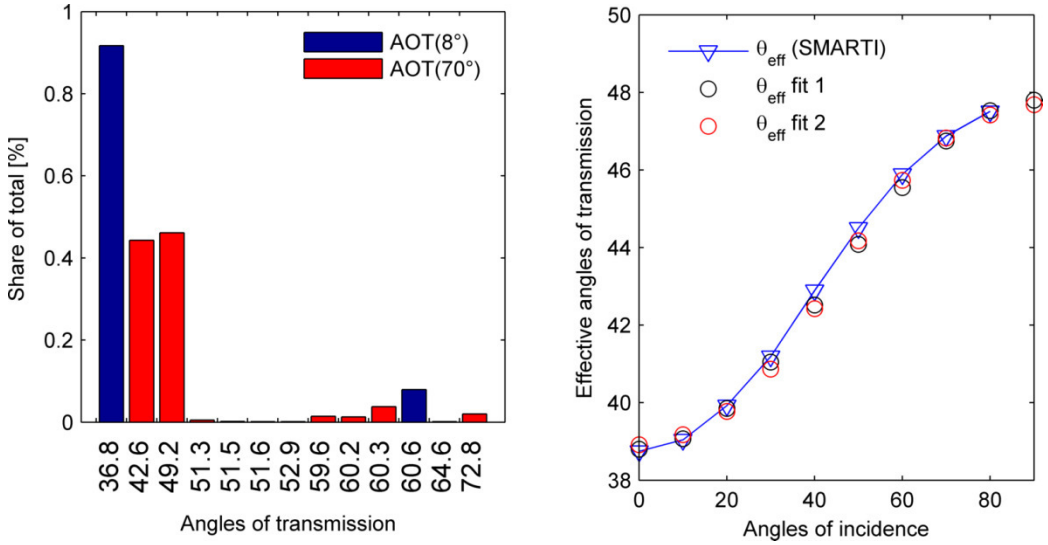

Fig. 5.16: Overview of the transmission angles inside a solar module were the cell texture consists of regular upright pyramids with a base angle of 54.57° for the incidence angle of 8° and 70° (left graph) and the effective angles of the module determined by means of ray tracing and two different fitting functions (right graph)

The effective angle of transmission θ_{eff} was calculated for all AOI from 0° to 80° in steps of 10°. The results are plotted on the right side of Fig. 5.16. The resulting function

monotonically increases and is surprisingly simple. Two different functions were heuristically found as best fits.

$$\theta_{eff} = 38.5° + \frac{5.2°}{2} \cdot \left(1 - \cos\left(\theta_{AOI} \cdot \frac{\pi}{90°}\right)\right) \tag{160}$$

$$\theta_{eff} = 38.5° + \frac{5.2°}{2} \cdot \left(1 + \mathrm{erf}\left((\theta_{AOI} - 45°) \cdot \frac{\pi}{90°}\right)\right) \tag{161}$$

Equation (160) is simpler with respect to its usage, because the error function used in the second equation needs to be evaluated numerically. The two constant angles 38.5° and 5.2° that are in the equations are found iteratively and no particular meaning could be given to these so far.

The effective transmission angle θ_{eff} can now be used in the analytical model. Again, all of the parameters are kept the same as presented in Table 5.2. The internal front side reflection is set to zero to allow only one forward and one backward pass through the cell. In Fig. 5.17 the angular correction factors $f_{IQE} - 1$ for the incidence angles 40°, 60° and 70° were simulated with the ray tracing tool and are compared to the results of the texture emulation.

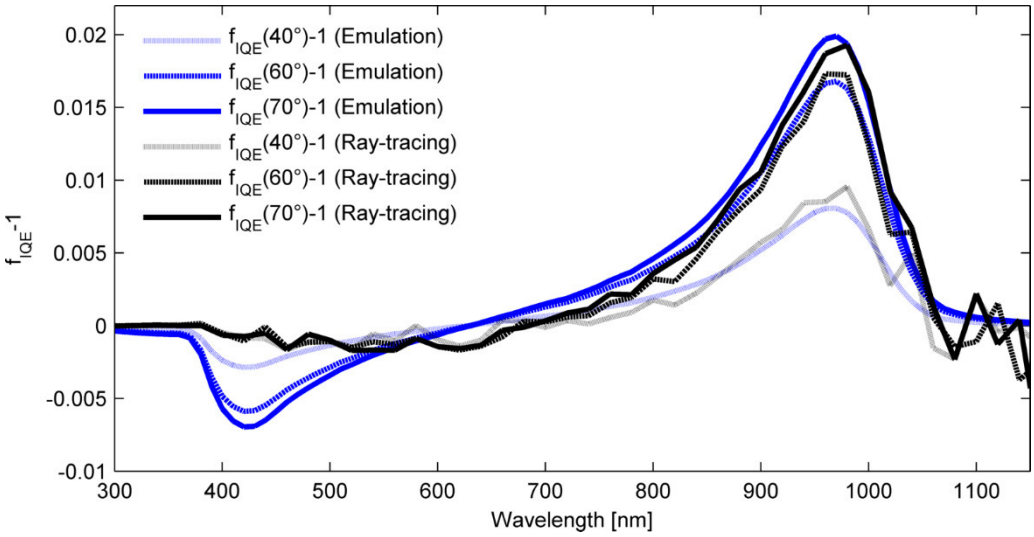

Fig. 5.17: Comparison of the $f_{IQE} - 1$ curves for 40°, 60° and 70° simulated with the ray tracing software SMARTI and the analytical model using the effective angle approach.

The results of the two simulations are comparable concerning the maximum value at around 960 nm. However, the slope in the region from 500 nm to 900 nm deviates a little bit. The negative local maximum at about 410 nm is entirely missing for the ray tracing simulation. This is probably due to the fact that the ray tracing algorithm uses the effective solution dimension ζ, which was explained in detail in section 3.2.2.

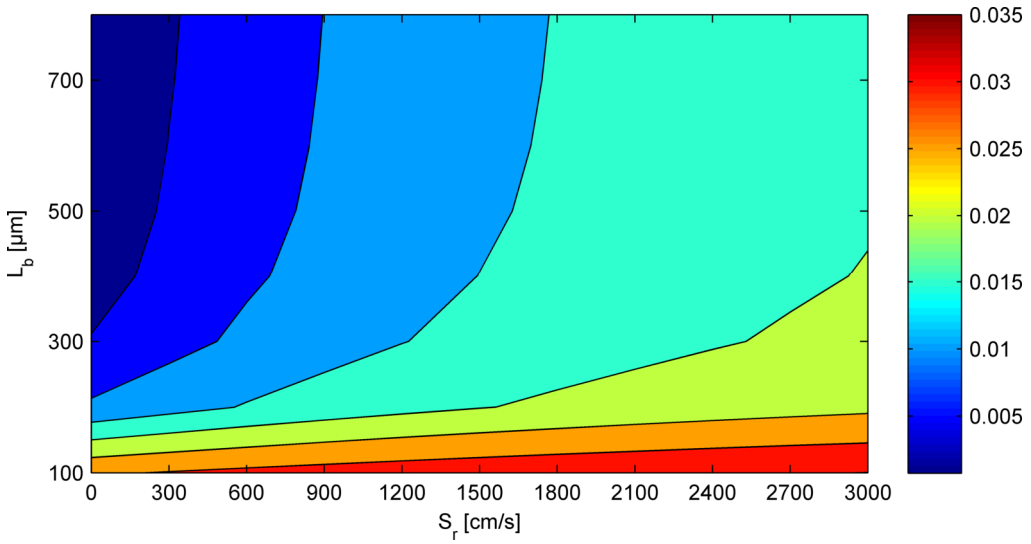

Fig. 5.18: Contour plot of the maximum value of $f_{IQE} - 1$ for the incidence angle of 70° as a function of the rear surface recombination velocity S_r and the base minority diffusion length L_n

The maximum value of the curve again is strongly dependent on the bulk diffusion length L_n and the rear surface recombination velocity S_r. To illustrate this dependency and to effectively be able to estimate the impact of the factor f_{IQE}, its maximum value for 70° was plotted as a contour plot in Fig. 5.18. The generation profiles that were created using the SMARTI software were subsequently uploaded into the software PC1D. Here the parameters L_n and S_r were systematically varied to receive the corresponding spectral response curves.

This plot is similar to the one for the planar solar cell (Fig. 5.6) but the actual values are much higher. The plot reveals that for low L_n, the impact of the rear surface recombination is minor while it is the dominant parameter for high bulk diffusion lengths. For very low diffusion lengths, a maximum increase of the IQE due to setting the AOI to 70° is in the range of 3 %. For a standard module, the maximum value will be at about 2.5 %, which can also be seen in Fig. 5.19 where the factor $f_{IQE^*} - 1$ generated with the help of the ray tracing software, and the corresponding measured values are plotted in comparison. An increase can be seen in the long wavelength region for incidence angles of 60° and 70° in the simulation as well as the measurement. The increase in the low wavelength region of the measurement has no correspondence in the simulation. This is most probably due to an underestimation of the simulated parasitic absorption in the encapsulation layer. For further investigations on this effect, the exact extinction coefficient of the encapsulation layer would need to be determined experimentally.

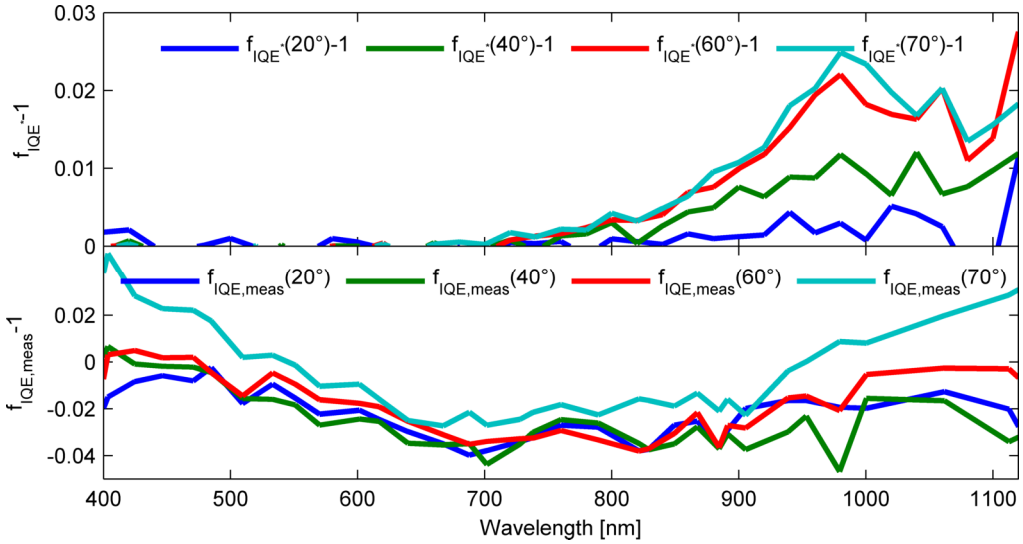

Fig. 5.19: Simulated correction factor $f_{IQE} - 1$ for the incidence angles of 20°, 40°, 60° and 70° of a standard solar module (upper graph) and the corresponding measurements (lower graph)

5.5 Angle dependence of solar modules with textured encapsulation

It is possible to strongly reduce the perpendicular and angular dependent reflectivity on the top surface of the encapsulation layer by implementing a texture as exemplarily shown in Fig. 2.12 (section 2.6). To investigate the angular dependency of such a solar module with two stacked textures, a sample was prepared. It consists of a standard mono-c-Si solar cell, which is encapsulated beneath a 100 μm thick PVDF polymeric film textured with 63.5° base angle grooves. The textured mono-c-Si solar cell implemented in the module was of the same type as the one in the standard module investigated above. Again, the electrical properties were similar to the ones of the planar solar cell listed in Table 5.2.

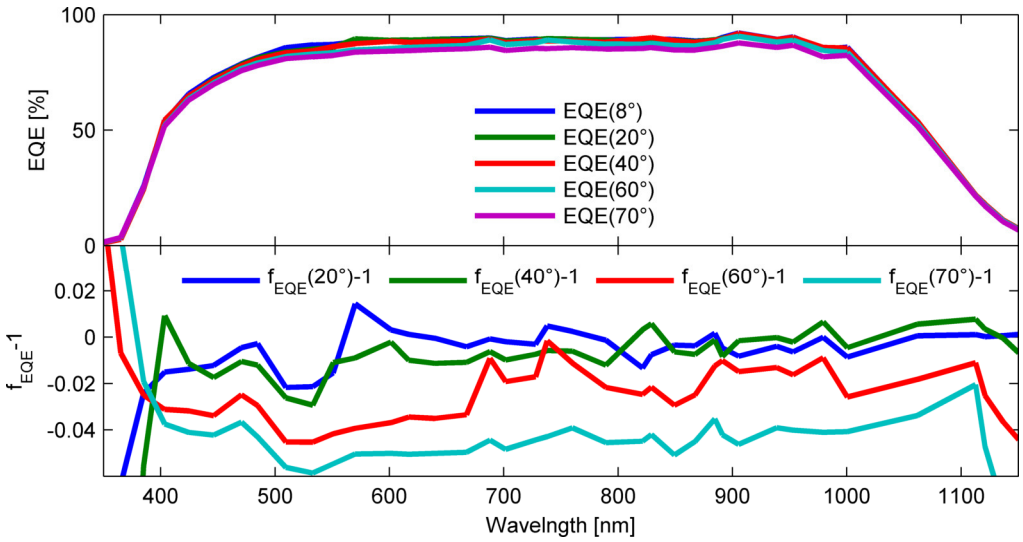

Fig. 5.20: EQE and $f_{EQE} - 1$ curves for the incidence angles of 20°, 40°, 60° and 70° for a solar module with textured encapsulation film

Comparing the factors $f_{EQE} - 1$ in Fig. 5.20 to the ones of the standard solar module (Fig. 5.13), it can be seen that the curves for the incidence angle of 60° and 70° are significantly

higher. Even though it is obvious that this effect is mainly due to the reduction of reflectivity on the top surface of the module, it is still interesting to investigate the angular dependency of the IQE in such a solar module. For this purpose, a ray tracing study was performed using the SMARTI software again. The results of the simulation are plotted in the upper part of Fig. 5.21. Again, an increase of the $f_{IQE^*} - 1$ can be seen for all AOI; but this time it is the incidence angle of 40° that gives the highest value, followed by 60°. In contrast, the IQE^* is comparably low for 70°. It is in the range of the one at 20° AOI. This effect suggests that due to the combination of both textures the mean angle of transmission is directed back to more vertical values for AOI > 40°.

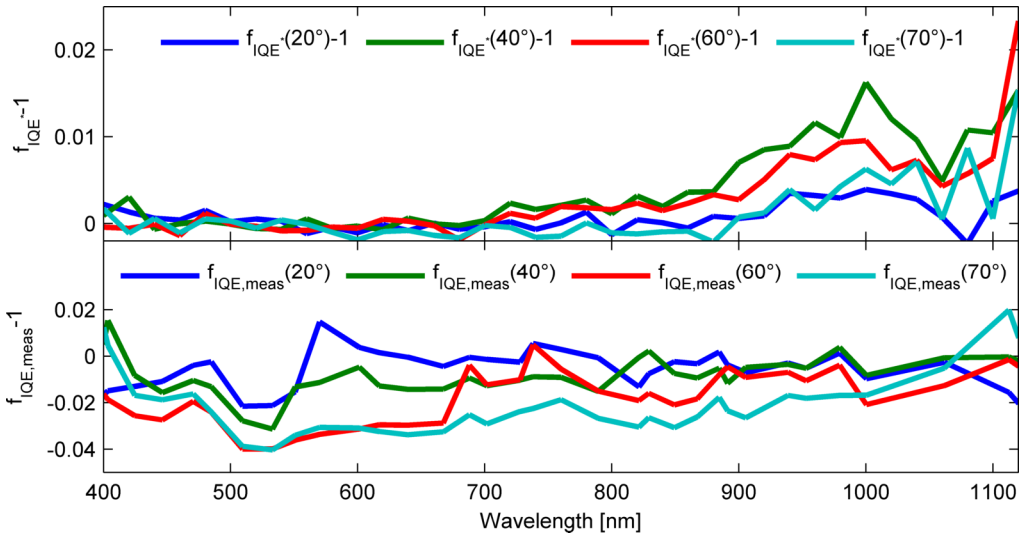

Fig. 5.21: Simulation of the $f_{IQE^*} - 1$ values for for the incidence angles of 20°, 40°, 60° and 70° for a solar module with textured front side encapsulation (upper graph) and the corresponding measurement values for $f_{IQE,meas} - 1$.

The corresponding measurements show a diverging behavior in the low wavelength range. It can be observed though that the curve for the incidence angle of 40° exceeds all the other curves in the wavelength region between 900 nm and 1060 nm. Altogether it seems that compared to the standard module, the effect of the AOI variation on the IQE is reduced with the application of an external texture.

5.6 Effects on the energy yield prediction

Above, the different angular effects were presented and analyzed for a planar cell and two module configurations. The question arises if it is necessary to implement any of these effects into the existing procedures for the annual energy yield calculation. Here no complete answer on this question can be given, as the simulation of all possible IQE curves including all azimuth angles would take too much time. However, it is already very instructive to investigate the impact that the implementation of the different angular effects has on the simulated current output at the incidence angle of 70°. For this purpose, the starting point is chosen to be the general equation for the determination of the short circuit current density $j_{sc}(\theta_i)$ at the AOI θ_i.

$$j_{sc}(\theta_i, \lambda) = q\phi_i(\lambda)\cos(\theta_i)\, EQE(\theta_i, \lambda) \tag{162}$$

Of course, this is not the approach that is generally used for the yield prediction in commercial software tools. These apply a procedure that corrects the current density at the maximum power point j_{MPP} by the incidence angle modifier (IAM) and an air mass correction factor (f_{AM}) as presented in section 2.2. As this approach obscures many of the actual physical effects, it is more reasonable to use (162). Unfortunately, the measurement of the EQE at all AOI is very time consuming and it is not probable that module manufacturers will provide the customers with these data. It is however much more probable to receive the EQE curve at perpendicular incidence, which then can be translated into the corresponding EQE curves at all other AOI. In the following, five different models for such a conversion procedure were analyzed for the incidence angle of 70°. The fifth model includes the angular reflection, the angle dependence of the parasitic absorption, and the angle dependence of the IQE and thus serves as a reference to evaluate the other models.

Table 5.3: Models for the transformation of the perpendicular EQE to the corresponding EQE at any AOI

	Equations	$j_{sc}(70°)$ $[mA/cm^2]$	**Deviation from model 5**
Model 1	$EQE(\theta_i, \lambda) = EQE_0(\lambda)$	11.90	13.80%
Model 2	$EQE(\theta_i, \lambda) = EQE_0(\lambda) \cdot (1 - R_F(\theta_i))/(1 - R_{F,0})$	10.28	-1.74%
Model 3	$EQE(\theta_i, \lambda) = EQE_0(\lambda) \cdot \frac{1-R_{tot,0}(\lambda)\cdot f_{R,tot}(\theta_i)}{1-R_{tot,0}(\lambda)}$	10.42	-0.38%
Model 4	$EQE(\theta_i, \lambda) = EQE_0(\lambda) \cdot \frac{1-R_{tot,0}(\lambda)\cdot f_{R,tot}(\theta_i,\lambda)-A_{Pa,0}(\lambda)\cdot f_{A,Pa}(\theta_i,\lambda)}{1-R_{tot,0}(\lambda)-A_{Pa,0}(\lambda)}$	10.43	-0.26%
Model 5	$EQE(\theta_i, \lambda) = EQE_0(\lambda) \cdot f_{IQE}(\theta_i, \lambda) \cdot \frac{1-R_{tot,0}(\lambda)\cdot f_{R,tot}(\theta_i,\lambda)-A_{Pa,0}(\lambda)\cdot f_{A,Pa}(\theta_i,\lambda)}{1-R_{tot,0}(\lambda)-A_{Pa,0}(\lambda)}$	10.46	Reference

The equations of the models as well as the results for the short circuit current densities at 70° and the relative deviations from the reference model 5 are given in Table 5.3. Model 1 assumes that the perpendicular EQE is not at all corrected, i.e., only the influence of the cosine loss is considered. This model overestimates the j_{sc} value by 13.8%. Model 2 includes the Fresnel reflection at the air-glass interface using (22). It reduces the EQE by a factor including the Fresnel reflection at any angle of incidence $R_F(\theta_i)$ and the Fresnel reflection at perpendicular incidence $R_{F,0}$. The results of this method are much closer to the reference model, but the deviation is still -1.74 % and as the simple Fresnel equation does not include spectral effects, which play an important role for AR-coatings for example, the deviation can change significantly if the solar spectrum is different from the AM 1.5 spectrum. Model 3 uses the angular correction factor $f_{R,tot}(\theta_i, \lambda)$ to correct the overall reflectivity at perpendicular incidence to the desired AOI. The correction factor can either be determined by measurements or by ray tracing simulations. The deviation from the reference model is comparably small with a value of -0.38 %. In model 4, the angular effect of the parasitic absorption is added using the correction factor $f_{A,Pa}(\theta_i, \lambda)$. To use this model in practical cases it is reasonable to perform ray tracing simulations to determine the perpendicular parasitic absorption and the corresponding correction factors. A

measurement of the different parasitic absorption mechanisms is possible in principle, but the effort would be accordingly high. The relative deviation of this model compared to the reference is -0.26 %. Thus, this is also the extent to which the implementation of the angle dependence of the IQE increases the accuracy of the module performance prediction compared to model 4.

6 Conclusion and outlook

In this thesis the influence of a changing AOI on the performance of solar cells and modules was investigated. To separate the different relevant effects an analytical model as well as a numerical simulation model were developed. The analytical model was primarily established for the simulation of the angular effects in a simple planar c-Si solar cell. But the model could also be used for the determination of the angle dependence of the IQE in a standard solar module by the application of an effective angle approach. The numerical model consists of a ray tracing tool that was named SMARTI which is combined with the one-dimensional semiconductor simulation software PC1D. With the help of this model textured solar cells and modules can be simulated and their angular performance can be determined.

Beside the simulations a measurement setup was developed consisting of a system for the determination of the angular spectral response and an integrating sphere in that the angular hemispherical reflectance of single cells or mini-modules can be measured. The combination of the measurement results allows the determination of the angular IQE.

The measurements as well as the simulations showed a strong angle dependence of the EQE for the planar solar cell sample. A less pronounced but still relevant angular effect on the EQE was demonstrated for a standard solar module. This angle and spectral dependence of a standard solar module was confirmed by the application of an angular electroluminescence measurement evaluated with help of the opto-electronic reciprocity relation.

The angle dependence of the EQE was also determined for a solar module with textured front side encapsulation layer where a strong reduction of the effect for high AOI was observed.

The angle dependence of the EQE is mainly determined by the changing reflectivity on the cells surface and the encapsulation layer if one is applied. The AR-coating on the cells surface is changing its spectral performance when the AOI is varied. Thick layers such as a glass cover are leading to an overall increase of reflectivity due to the spectral independent Fresnel reflection.

Additionally, the angle dependence of the EQE is also caused by the variation of different parasitic absorption processes. These are namely the absorption in inactive layers, in the contact grid, in the AR-coating and by free carriers. Using the analytical model and the SMARTI ray tracer the processes were evaluated for a planar solar cell and a standard solar module.

Beyond that a detailed analysis was given on the variation of the IQE with a changing AOI. The effect strongly depends on the thickness of the solar cell W, its base diffusion length L_b and its rear surface recombination velocity S_r. The analysis showed that the IQE increased in the long wavelength region up to a value of about 960 nm from where it decreases back to the perpendicular value. The effect was attributed to the fact that photons

get absorbed closer to the surface when the AOI is getting steeper and thus the probability to reach the collecting junction is increased. This effect is strongly reduced as soon as the photons get reflected from the back side of the cell and is completely negligible for long wavelength photons as their absorption location is randomly distributed over the cells thickness. Furthermore, it could be shown that the angular effect on the IQE is strongly increased if a texture is applied to the solar cell because the shift of the absorption location closer to the junction is even more pronounced for the case of a textured surface.

If the power output of a solar cell or module is calculated on the basis of its spectral response, for high AOI the perpendicular SR-curve should be correspondingly corrected. At least the variation of the overall reflectance with the AOI should be considered in the correction procedure. The influence of the parasitic absorption however is comparably small for a standard solar module. The overall influence of the angle dependence of the IQE is a little bit higher but its importance for the accuracy of an annual yield prediction is still comparably small.

However, the influence of the different effects on the prediction of the annual yield could not be determined as the time consumption of the ray tracing tool SMARTI is too high. A combination of the ray tracing tool with a matrix formalism as implemented in OPTOS presented by Tucher [158] could in future be used to determine the influence of the different angular effects on the overall annual energy yield.

To further increase the accuracy of the measurement setups for the angular spectral response and the angular reflection determination, a systematic comparison to similar measurement setups in other laboratories should be performed.

In the future the investigation of the angular performance of other solar cell and module samples should be conducted. Silicon-technologies of interest are multi-crystalline silicon solar cells, the PERC-technology, IBC (Interdigitated Back Contact Solar Cells), Bifacial solar cells and HIT (Heterojunction with Intrinsic Thin-layer) solar cells. Also thin film technologies such as CIGS, CdTe and Perovskites are of interest as well as tandem and triple junction solar cells.

Appendix A

Determination of the cell temperature with the help of the $NOCT$ parameter

$$T_{cell} = T_{amb} + \frac{(NOCT - 20)}{800 * I_g} \tag{A.1}$$

Source: [63, p. 1024]

Determination of the generation profile for the backward passes in the base region of a solar cell (simple model)

Table A.1: Determination of the generation profile of the subsequent back reflections in the base region using the simple solar cell model described in 2.4.2

$G_{bv,b}(\lambda, x) =$	$\phi_{b,b,init}$	$T_{d,v}$	$T_{u,v}$	R_{bv}	R_{fv}	$\frac{\alpha}{\cos(\theta_v)} \exp\left(-\frac{\alpha(W_b - x)}{\cos(\theta_v)}\right)$
1. backward pass	1	0	0	0	0	1
2. backward pass	1	1	1	1	1	1
3. backward pass	1	2	2	2	2	1
…						
$(v+1)^{th}$ backward pass	1	v	v	v	v	1

where

$$\phi_{b,b}^{init} = \phi_i\left(1 - R_{fe}\right) T_{d,1} R_{b1} T_{u,1} R_{f1} T_{d,v} R_{bv} \tag{A.2}$$

Determination of the number of absorbed photons in the emitter

$$f_{a,e} = \phi_i\left(1 - R_{fe}\right)\left(1 - \exp(-\alpha'(\theta_1) W_e)\right) \tag{A.3}$$

$$f_{b,e} = \phi_i\left(1 - R_{fe}\right) T_{d,1} R_{b1} \exp(-\alpha'(\theta_2)(W_b + W_{SCR}))\left(1 - \exp(-\alpha'(\theta_2) W_e)\right) \tag{A.4}$$

$$f_{c,e} = \phi_i\left(1 - R_{fe}\right) \frac{T_{d,1} R_{b1} T_{u,1}}{1 - R_{bv} R_{fv} T_{d,v} T_{u,v}}\left(1 - \exp(-\alpha'(\theta_v) W_e)\right) \tag{A.5}$$

$$f_{d,e} = \phi_i\left(1 - R_{fe}\right) \frac{T_{d,1} R_{b1} T_{u,1} R_{f1} \exp\left(-\alpha'(\theta_n)(2W - W_e)\right) R_{bn}}{1 - R_{bv} R_{fv} T_{d,v} T_{u,v}} \cdot \left(1 - \exp(-\alpha'(\theta_v) W_e)\right) \tag{A.6}$$

Determination of the collection probabilities in the emitter region

$$\eta_{forward,e}(\theta) = \frac{\alpha'(\theta)L_e}{(\alpha'(\theta)^2 L_e^2 - 1)(1 - \exp(-\alpha'(\theta)W_e))}\left(\alpha'(\theta)L_e - \frac{\sinh\left(\frac{W_e}{L_e}\right) + \frac{S_n L_e}{D_e}\cosh\left(\frac{W_e}{L_e}\right) - \left(\frac{S_e L_e}{D_e} - \alpha'(\theta)L_e\right)\exp(-\alpha'(\theta)W_e)}{\cosh\left(\frac{W_e}{L_e}\right) + \frac{S_e L_e}{D_e}\sinh\left(\frac{W_e}{L_e}\right)}\right) \quad \text{(A.7)}$$

$$\eta_{back,e}(\theta) = \frac{\alpha'(\theta)L_e}{(\alpha'(\theta)^2 L_e^2 - 1)(1 - \exp(-\alpha'(\theta)W_e))}\left(\alpha'(\theta)L_e \exp(-\alpha'(\theta)W_e) - \frac{\left(\sinh\left(\frac{W_e}{L_e}\right) + \frac{S_e L_e}{D_e}\cosh\left(\frac{W_e}{L_e}\right)\right)\exp(-\alpha'(\theta)W_e) - \left(\frac{S_e L_e}{D_e} + \alpha'(\theta)L_e\right)}{\cosh\left(\frac{W_e}{L_e}\right) + \frac{S_e L_e}{D_e}\sinh\left(\frac{W_e}{L_e}\right)}\right) \quad \text{(A.8)}$$

Determination of the number of absorbed photons in the space charge region

$$f_{a,scr} = \phi_i\left(1 - R_{fe}\right)\exp(-\alpha'(\theta_1)W_e)\left(1 - \exp(-\alpha'(\theta_1)W_{scr})\right) \quad \text{(A.9)}$$

$$f_{b,scr} = \phi_i\left(1 - R_{fe}\right)T_{d,1}R_{b1}\exp(-\alpha'(\theta_2)W_b)\left(1 - \exp(-\alpha'(\theta_2)W_{scr})\right) \quad \text{(A.10)}$$

$$f_{c,scr} = \phi_i\left(1 - R_{fe}\right)\frac{T_{d,1}R_{b1}T_{u,1}R_{f1}\exp(-\alpha'(\theta_v)W_e)}{1 - R_{bv}R_{fv}T_{d,v}T_{u,v}}\left(1 - \exp(-\alpha'(\theta_v)W_{scr})\right) \quad \text{(A.11)}$$

$$f_{d,scr} = \phi_i\left(1 - R_{fe}\right)T_{d,1}R_{b1}T_{u,1}R_{f1}R_{bv}\frac{\exp(-\alpha'(\theta_v)(W + W_b))}{1 - R_{bv}R_{fv}T_{d,v}T_{u,v}} \cdot \left(1 - \exp(-\alpha'(\theta_v)W_{scr})\right) \quad \text{(A.12)}$$

Appendix B

Compilation of all relevant equations for the complete analytical solar cell model described in section 3.1

$$R_{fe} = M_{fi} \cdot R_{fi} + M_{bb} \cdot R_{bb} + M_c \cdot R_c \quad \text{(B.1)}$$

$$T_{fe} = M_c \cdot T_c \quad \text{(B.2)}$$

$$A_{grid} = M_{fi} \cdot A_{fi} + M_{bb} \cdot A_{bb} \quad \text{(B.3)}$$

$$A_{AR} = M_c \cdot A_c \quad \text{(B.4)}$$

$$R_f = (1 - M_c) + M_c \cdot R_{c,i} \quad \text{(B.5)}$$

$$T_f = 1 - R_f \quad \text{(B.6)}$$

$$T_{f,d} = 1 - R_{f,d} \quad \text{(B.7)}$$

$R_c/A_c/T_c/R_b/R_{c,i}/R_{fi}/A_{fi}/R_{bb}/A_{bb}$: Calculated with transfer matrix method [61] (B.8)

$$T = \exp(-(\alpha + \alpha_{FCA,e})W_e/\cos(\theta_t))\exp(-(\alpha + \alpha_{FCA,scr})W_{scr}/\cos(\theta_t))\exp(-(\alpha + \alpha_{FCA,b})W_b/\cos(\theta_t)) \quad \text{(B.9)}$$

$$T_{diff} = \exp(-(2\alpha + 2\alpha_{FCA,e})W_e)\exp(-(2\alpha + 2\alpha_{FCA,scr})W_{scr})\exp(-(2\alpha + 2\alpha_{FCA,b})W_b) \quad \text{(B.10)}$$

$$p_{sc} = \alpha \cdot W/(\alpha \cdot W + \alpha_{FCA,e} \cdot W_e + \alpha_{FCA,scr} \cdot W_{scr} + \alpha_{FCA,b} \cdot W_b) \quad \text{(B.11)}$$

$$p_{FCA} = (\alpha_{FCA,e} \cdot W_e + \alpha_{FCA,scr} \cdot W_{scr} + \alpha_{FCA,b} \cdot W_b)/(\alpha \cdot W + \alpha_{FCA,e} \cdot W_e + \alpha_{FCA,scr} \cdot W_{scr} + \alpha_{FCA,b} \cdot W_b) \quad \text{(B.12)}$$

$$A_{tot} = A_{dir} + A_{diff} \quad \text{(B.13)}$$

$$A_{dir} = \frac{T_{fe}(1-h_f)(1+(1-h_b)TR_b)(1-T)}{1-(1-h_f)(1-h_b)T^2R_bR_f} \quad \text{(B.14)}$$

$$A_{diff} = \frac{T_{fe}(h_f + h_b(1-h_f)T_{diff}TR_{f,d}R_b + h_fT_{diff}R_{b,d} + h_b(1-h_f)TR_b)(1-T_{diff})}{(T_{diff}^2R_{b,d}R_{f,d}-1)\left((1-h_f)(1-h_b)T^2R_bR_f-1\right)} \quad \text{(B.15)}$$

$$A_{sc} = p_{sc} \cdot A_{tot} \quad \text{(B.16)}$$

$$A_{FCA} = p_{FCA} \cdot A_{tot} \quad \text{(B.17)}$$

$$T_{tot} = T_{dir} + T_{diff} \quad \text{(B.18)}$$

$$T_{dir} = \frac{T_{fe}(1-d_{rel,f})T(1-R_b)}{1-(1-d_{rel,f})(1-d_{rel,b})T^2R_bR_f} \quad \text{(B.19)}$$

$$T_{diff} = \frac{T_{fe} \cdot (d_{rel,f} \cdot T(60°) + d_{rel,b} \cdot (1-d_{rel,f}) \cdot T(60°)^2 \cdot T \cdot R_{f,d} \cdot R_b) \cdot (1-R_{b,d})}{(T(60°)^2 \cdot R_{b,d} \cdot R_{f,d}-1)\left((1-d_{rel,b})(1-d_{rel,f}) \cdot T^2 \cdot R_b \cdot R_f - 1\right)} \quad \text{(B.20)}$$

$$\hat{\phi}_a = \phi_i \frac{T_{fe}(1-h_f)}{(1-(1-h_f)(1-h_b)T^2R_bR_f)} \quad \text{(B.21)}$$

$$\hat{\phi}_b = \phi_i \frac{T_{fe}(1-h_f)(1-h_b)TR_b}{(1-(1-h_f)(1-h_b)T^2R_bR_f)} \quad \text{(B.22)}$$

$$\hat{\phi}_c = \phi_i \frac{T_{fe}(h_f + h_b(1-h_f)T_{diff}TR_{f,d}R_b)}{(T_{diff}^2R_{b,d}R_{f,d}-1)\left((1-h_f)(1-h_b)T^2R_bR_f-1\right)} \quad \text{(B.23)}$$

$$\hat{\phi}_d = \phi_i \frac{T_{fe}(h_fT_{diff}R_{b,d} + h_b(1-h_f)TR_b)}{(T_{diff}^2R_{b,d}R_{f,d}-1)\left((1-h_f)(1-h_b)T^2R_bR_f-1\right)} \quad \text{(B.24)}$$

$$T_{e,s}^{+} = 1 \quad \text{(B.25)}$$

$$T_{e,s}^{-} = \exp\left(-\left((\alpha' + \alpha'_{FCA,b}) \cdot W_b + (\alpha' + \alpha'_{FCA,scr}) \cdot W_{scr}\right)\right) \quad \text{(B.26)}$$

$$T_{e,d}^{+} = 1 \quad \text{(B.27)}$$

$$T_{e,d}^{-} = \exp\left(-2 \cdot \left((\alpha + \alpha_{FCA,b}) \cdot W_b + (\alpha + \alpha_{FCA,scr}) \cdot W_{scr}\right)\right) \quad \text{(B.28)}$$

$$T_{scr,s}^{+} = \exp(-(\alpha' + \alpha'_{FCA,e}) \cdot W_e) \quad \text{(B.29)}$$

$$T_{scr,s}^{-} = \exp(-(\alpha' + \alpha'_{FCA,b}) \cdot W_b) \quad \text{(B.30)}$$

$$T_{scr,d}^{+} = \exp\left(-2 \cdot \left((\alpha + \alpha_{FCA,e}) \cdot W_e\right)\right) \quad \text{(B.31)}$$

$$T_{scr,d}^{-} = \exp\left(-2 \cdot \left((\alpha + \alpha_{FCA,b}) \cdot W_b\right)\right) \quad \text{(B.32)}$$

$$T_{b,s}^{+} = \exp\left(-\left((\alpha' + \alpha'_{FCA,e}) \cdot W_e + (\alpha' + \alpha'_{FCA,scr}) \cdot W_{scr}\right)\right) \quad \text{(B.33)}$$

$$T_{b,s}^{-} = 1 \quad \text{(B.34)}$$

$$T_{b,d}^{+} = \exp\left(-2 \cdot \left((\alpha + \alpha_{FCA,b}) \cdot W_b + (\alpha + \alpha_{FCA,scr}) \cdot W_{scr}\right)\right) \quad \text{(B.35)}$$

$$T_{b,d}^{-} = 1 \quad \text{(B.36)}$$

$$\eta_{forward,e}(\theta) = \frac{\alpha'(\theta)L_e}{(\alpha'(\theta)^2 \cdot L_e^2 - 1)(1-\exp(-\alpha'(\theta) \cdot W_e))}\left(\alpha'(\theta)L_e - \frac{\sinh\left(\frac{W_e}{L_e}\right) + \frac{S_nL_e}{D_e}\cosh\left(\frac{W_e}{L_e}\right) - \left(\frac{S_eL_e}{D_e} - \alpha'(\theta)L_e\right)\exp(-\alpha'(\theta)W_e)}{\cosh\left(\frac{W_e}{L_e}\right) + \frac{S_eL_e}{D_e}\sinh\left(\frac{W_e}{L_e}\right)}\right) \quad \text{(B.37)}$$

$$\eta_{back,e}(\theta) = \frac{\alpha'(\theta)L_e}{(\alpha'(\theta)^2 L_e^2 - 1)(1 - \exp(-\alpha'(\theta)W_e))}\left(\alpha'(\theta)L_e \exp(-\alpha'(\theta)W_e) - \frac{\left(\sinh\left(\frac{W_e}{L_e}\right) + \frac{S_e L_e}{D_e}\cosh\left(\frac{W_e}{L_e}\right)\right)\exp(-\alpha'(\theta)W_e) - \left(\frac{S_e L_e}{D_e} + \alpha'(\theta)L_e\right)}{\cosh\left(\frac{W_e}{L_e}\right) + \frac{S_e L_e}{D_e}\sinh\left(\frac{W_e}{L_e}\right)}\right) \tag{B.38}$$

$$\eta_{forward,b}(\theta) = \frac{\alpha'(\theta)L_b}{(\alpha'(\theta)^2 L_b^2 - 1)(1 - \exp(-\alpha'(\theta)W_b))}\left(\alpha'(\theta)L_b - \frac{\sinh\left(\frac{W_b}{L_b}\right) + \frac{S_b L_b}{D_b}\cosh\left(\frac{W_b}{L_b}\right) - \left(\frac{S_b L_b}{D_b} - \alpha'(\theta)L_b\right)\exp(-\alpha'(\theta)W_b)}{\cosh\left(\frac{W_b}{L_b}\right) + \frac{S_b L_b}{D_b}\sinh\left(\frac{W_b}{L_b}\right)}\right) \tag{B.39}$$

$$\eta_{back,b}(\theta) = \frac{\alpha'(\theta)L_b}{(\alpha'(\theta)^2 L_b^2 - 1)(1 - \exp(-\alpha'(\theta)W_b))}\left(\alpha'(\theta)L_b \exp(-\alpha'(\theta)W_b) - \frac{\left(\sinh\left(\frac{W_b}{L_b}\right) + \frac{S_b L_b}{D_b}\cosh\left(\frac{W_b}{L_b}\right)\right)\exp(-\alpha'(\theta)W_b) - \left(\frac{S_b L_b}{D_b} + \alpha'(\theta)L_b\right)}{\cosh\left(\frac{W_b}{L_b}\right) + \frac{S_b L_b}{D_b}\sinh\left(\frac{W_b}{L_b}\right)}\right) \tag{B.40}$$

Derivation of the direct escape reflection

Table B.1: Derivation of the direct component of the escape reflection using listed exponents for the corresponding terms where $v = 0, 1, 2 \cdots \infty$

	T_{fe}	$(1-h_f)$	T	R_b	$(1-h_b)$	R_f	T_f
$R_{1.dir}$	1	1	2	1	1	0	1
$R_{2.dir}$	1	2	4	2	2	1	1
$R_{3.dir}$	1	3	6	3	3	2	1
…							
$R_{(v+1).dir}$	T_{fe}	$(1-h_f)^{v+1}$	$T^{2(v+1)}$	R_b^{v+1}	$(1-h_b)^{v+1}$	R_f^v	T_f

$$R_{esc,dir} = \frac{T_{fe}(1-h_f)(1-h_b)T^2 R_b T_f}{1 - (1-h_f)(1-h_b)T^2 R_b R_f} \tag{B.41}$$

Derivation of the diffuse escape reflection

Table B.2: Derivation of the diffuse component of the escape reflection using listed exponents for the corresponding terms. The bold formatted numbers indicate the light paths where the light is transformed into diffuse light at the front surface and the grey numbers the paths where this transition occurs at the back surface.

		T_{fe}	h_f	h_b	$(1-h_f)$	$(1-h_b)$	T_{diff}	T	$R_{b,d}$	$R_{f,d}$	R_b	R_f	$T_{f,d}$
$R_{1,diff}=$		**1**	**1**		**0**	**0**	**2**	**0**	**1**	**0**	**0**	**0**	**1**
	+	1		1	1	0	1	1	0	0	1	0	1
$R_{2,diff}=$		**1**	**1**		**0**	**0**	**4**	**0**	**2**	**1**	**0**	**0**	**1**
	+	**1**	**1**		**1**	**1**	**2**	**2**	**1**	**0**	**1**	**1**	**1**
	+	1		1	1	0	3	1	1	1	1	0	1
	+	1		1	2	1	1	3	0	0	2	1	1
$R_{3,diff}=$		**1**	**1**		**0**	**0**	**6**	**0**	**3**	**2**	**0**	**0**	**1**
	+	**1**	**1**		**1**	**1**	**4**	**2**	**2**	**1**	**1**	**1**	**1**
	+	**1**	**1**		**2**	**2**	**2**	**4**	**1**	**0**	**2**	**2**	**1**
	+	1		1	1	0	5	1	2	2	1	0	1
	+	1		1	2	1	3	3	1	1	2	1	1
	+	1		1	3	2	1	5	0	0	3	2	1
…													
$\sum_{l=0}^{\infty}\sum_{v=0}^{l} f$		$\boldsymbol{T_{fe}}$	h_f		$\boldsymbol{(1-h_f)^v}$	$\boldsymbol{(1-h_b)^v}$	$\boldsymbol{T_{diff}^{2+2l-2v}}$	$\boldsymbol{T^{2v}}$	$\boldsymbol{R_{b,d}{}^{1+l-v}}$	$\boldsymbol{R_{f,d}{}^{l-v}}$	$\boldsymbol{R_b{}^v}$	$\boldsymbol{R_f{}^v}$	$\boldsymbol{T_{f,d}}$
$\sum_{l=0}^{\infty}\sum_{v=0}^{l} f$		T_{fe}		h_b	$(1-h_f)^{v+1}$	$(1-h_b)^v$	$T_{diff}^{1+2l-2v}$	T^{2v+1}	$R_{b,d}{}^{l-v}$	$R_{f,d}{}^{l-v}$	$R_b{}^{v+1}$	$R_f{}^v$	$T_{f,d}$

$$R_{esc1,diff}=\frac{T_{fe}h_fT_{diff}^2R_{b,d}T_{f,d}}{\left(T_{diff}^2R_{b,d}R_{f,d}-1\right)\left((1-h_b)(1-h_f)T^2R_bR_f-1\right)} \tag{B.42}$$

$$R_{esc2,diff}=\frac{T_{fe}h_b(1-h_f)T_{diff}TR_bT_{f,d}}{\left(T_{diff}^2R_{b,d}R_{f,d}-1\right)\left((1-h_b)(1-h_f)T^2R_bR_f-1\right)} \tag{B.43}$$

$$R_{esc,diff}=\frac{T_{fe}(h_fT_{diff}^2R_{b,d}+\ h_b(1-h_f)T_{diff}TR_b)T_{f,d}}{\left(T_{diff}^2R_{b,d}R_{f,d}-1\right)\left((1-h_b)(1-h_f)T^2R_bR_f-1\right)} \tag{B.44}$$

Derivation of the direct absorption

Table B.3: Derivation of the direct component of the absorption using listed exponents for the corresponding terms where $v=0,1,2\cdots\infty$.

	T_{fe}	$(1-h_f)$	T	R_b	$(1-h_b)$	R_f	$(1-T)$
$A_{forw1.dir}$	**1**	**1**	**0**	**0**	**0**	**0**	**1**
$A_{back1.dir}$	1	1	1	1	1	0	1
$A_{forw2.dir}$	**1**	**2**	**2**	**1**	**1**	**1**	**1**
$A_{back2.dir}$	1	2	3	2	2	1	1
$A_{forw3.dir}$	**1**	**3**	**4**	**2**	**2**	**2**	**1**
$A_{back3.dir}$	1	3	5	3	3	2	1
…							
$\sum_{v=0}^{\infty} f$	$\boldsymbol{T_{fe}}$	$\boldsymbol{(1-h_f)^{v+1}}$	$\boldsymbol{T^{2v}}$	$\boldsymbol{R_b^v}$	$\boldsymbol{(1-h_b)^v}$	$\boldsymbol{R_f^v}$	$\boldsymbol{(1-T)}$
$\sum_{v=0}^{\infty} f$	T_{fe}	$(1-h_f)^{v+1}$	T^{2v+1}	R_b^{v+1}	$(1-h_b)^{v+1}$	R_f^v	$(1-T)$

$$A_{dir}^{forw} = \frac{T_{fe}(1-h_f)(1-T)}{1-(1-h_f)(1-h_b)T^2R_bR_f} = \hat{\phi}_a \frac{1-T}{\phi_i} \tag{B.45}$$

$$A_{dir}^{back} = \frac{T_{fe}(1-h_f)(1-h_b)TR_b(1-T)}{1-(1-h_f)(1-h_b)T^2R_bR_f} = \hat{\phi}_b \frac{1-T}{\phi_i} \tag{B.46}$$

$$A_{dir} = \frac{T_{fe}(1-h_f)(1+(1-h_b)TR_b)(1-T)}{1-(1-h_f)(1-h_b)T^2R_bR_f} \tag{B.47}$$

Derivation of the diffuse absorption

For the determination of the diffuse absorption the forward and the backward passes are handled separately. Additionally, for both directions two absorptions paths are handled separately depending on whether the transformation from direct to diffuse light is occurring at the fron or at the back surface.

Diffuse forward absorption:

Table B.4: Derivation of the diffuse component of the absorption in forward direction using listed exponents for the corresponding terms. The bold formatted and the grey numbers indicate the separation in two double sums.

		T_{fe}	h_f	h_b	$(1-h_f)$	$(1-h_b)$	T_{diff}	T	$R_{b,d}$	$R_{f,d}$	R_b	R_f	$(1-T_{diff})$
$A_{1,diff}^{forw}$		***1***	***1***	***0***	***0***	***0***	***0***	***0***	***0***	***0***	***0***	***0***	***1***
$A_{2,diff}^{forw}$		***1***	***1***	***0***	***0***	***0***	***2***	***0***	***1***	***1***	***0***	***0***	***1***
	+	1	0	1	1	0	1	1	0	1	1	0	1
	+	***1***	***1***	***0***	***1***	***1***	***0***	***2***	***0***	***0***	***1***	***1***	***1***
$A_{3,diff}^{forw}$		***1***	***1***	***0***	***0***	***0***	***4***	***0***	***2***	***2***	***0***	***0***	***1***
	+	1	0	1	1	0	3	1	1	2	1	0	1
	+	***1***	***1***	***0***	***1***	***1***	***2***	***2***	***1***	***1***	***1***	***1***	***1***
	+	1	0	1	2	1	1	3	0	1	2	1	1
	+	***1***	***1***	***0***	***2***	***2***	***0***	***4***	***0***	***0***	***2***	***2***	***1***
…													
$\sum_{l=0}^{\infty}\sum_{v=0}^{l} f$		$\boldsymbol{T_{fe}}$	h_f		$\boldsymbol{(1-h_f)^v}$	$\boldsymbol{(1-h_b)^v}$	$\boldsymbol{T_{diff}^{2l-2v}}$	$\boldsymbol{T^{2v}}$	$\boldsymbol{{R_{b,d}}^{l-v}}$	$\boldsymbol{{R_{f,d}}^{l-v}}$	$\boldsymbol{{R_b}^v}$	$\boldsymbol{{R_f}^v}$	$\boldsymbol{(1-T_{diff})}$
$\sum_{l=0}^{\infty}\sum_{v=0}^{l} f$		T_{fe}		h_b	$(1-h_f)^{v+1}$	$(1-h_b)^v$	$T_{diff}^{1+2l-2v}$	T^{2v+1}	${R_{b,d}}^{l-v}$	${R_{f,d}}^{l-v+1}$	${R_b}^{v+1}$	${R_f}^v$	$(1-T_{diff})$

$$A_{diff,1}^{forw} = \frac{T_{fe}h_f(1-T\_diff)}{\left(T(60°)^2R_{b,d}R_{f,d}-1\right)\left((1-h_f)(1-h_b)T^2R_bR_f-1\right)} \tag{B.48}$$

$$A_{diff,2}^{forw} = \frac{T_{fe}h_b(1-h_f)T_{diff}TR_{f,d}R_b(1-T_{diff})}{\left(T_{diff}^2R_{b,d}R_{f,d}-1\right)\left((1-h_f)(1-h_b)T^2R_bR_f-1\right)} \tag{B.49}$$

$$A_{diff}^{forw} = \frac{T_{fe}\left(h_f+h_b(1-h_f)T_{diff}TR_{f,d}R_b\right)(1-T_{diff})}{\left(T_{diff}^2R_{b,d}R_{f,d}-1\right)\left((1-h_f)(1-h_b)T^2R_bR_f-1\right)} = \hat{\phi}_c \frac{1-T_{diff}}{\phi_i} \tag{B.50}$$

Diffuse backward absorption:

Table B.5: Derivation of the diffuse component of the absorption in backward direction using listed exponents for the corresponding terms. The bold formatted and the grey numbers indicate the separation in two double sums.

		T_{fe}	h_f	h_b	$(1-h_f)$	$(1-h_b)$	T_{diff}	T	$R_{b,d}$	$R_{f,d}$	R_b	R_f	$(1-T_{diff})$
$A_{1,diff}^{back}$		***1***	***1***	***0***	***0***	***0***	***1***	***0***	***1***	***0***	***0***	***0***	***1***
	+	1	0	1	1	0	0	1	0	0	1	0	1
$A_{2,diff}^{back}$		***1***	***1***	***0***	***0***	***0***	***3***	***0***	***2***	***1***	***0***	***0***	***1***
	+	1	0	1	1	0	2	1	1	1	1	0	1
	+	***1***	***1***	***0***	***1***	***1***	***1***	***2***	***1***	***0***	***1***	***1***	***1***
	+	1	0	1	2	1	0	3	0	0	2	1	1
$A_{3,diff}^{back}$		***1***	***1***	***0***	***0***	***0***	***5***	***0***	***3***	***2***	***0***	***0***	***1***
	+	1	0	1	1	0	4	1	2	2	1	0	1
	+	***1***	***1***	***0***	***1***	***1***	***3***	***2***	***2***	***1***	***1***	***1***	***1***
	+	1	0	1	2	1	2	3	1	1	2	1	1
	+	***1***	***1***	***0***	***2***	***2***	***1***	***4***	***1***	***0***	***2***	***2***	***1***
	+	1	0	1	3	2	0	5	0	0	3	2	1
…													
$\sum_{l=0}^{\infty}\sum_{v=0}^{l} f$		$\boldsymbol{T_{fe}}$	h_f		$(\mathbf{1}-h_f)^{v}$	$(\mathbf{1}-h_b)^{v}$	$\boldsymbol{T_{diff}^{1+2l-2v}}$	$\boldsymbol{T^{2v}}$	$\boldsymbol{R_{b,d}}^{l-v+1}$	$\boldsymbol{R_{f,d}}^{l-v}$	$\boldsymbol{R_b}^{v}$	$\boldsymbol{R_f}^{v}$	$(\mathbf{1}-\boldsymbol{T_{diff}})$
$\sum_{l=0}^{\infty}\sum_{v=0}^{l} f$		T_{fe}		h_b	$(1-h_f)^{v+1}$	$(1-h_b)^{v}$	T_{diff}^{2l-2v}	T^{2v+1}	${R_{b,d}}^{l-v}$	${R_{f,d}}^{l-v}$	${R_b}^{v+1}$	${R_f}^{v}$	$(1-T_{diff})$

$$A_{diff,1}^{back} = \frac{T_{fe}h_f T_{diff}R_{b,d}\big(1-T(60°)\big)}{\big(T_{diff}^2 R_{b,d}R_{f,d}-1\big)\big((1-h_f)(1-h_b)T^2R_bR_f-1\big)} \tag{B.51}$$

$$A_{diff,2}^{back} = \frac{T_{fe}h_b(1-h_f)TR_b(1-T_{diff})}{\big(T_{diff}^2 R_{b,d}R_{f,d}-1\big)\big((1-h_f)(1-h_b)T^2R_bR_f-1\big)} \tag{B.52}$$

$$A_{diff}^{back} = \frac{T_{fe}\big(h_f T_{diff}R_{b,d}+h_b(1-h_f)TR_b\big)(1-T_{diff})}{\big(T_{diff}^2 R_{b,d}R_{f,d}-1\big)\big((1-h_f)(1-h_b)T^2R_bR_f-1\big)} = \hat{\phi}_d\frac{1-T_{diff}}{\phi_i} \tag{B.53}$$

Combining diffuse forward and backward absorption:

$$A_{diff} = \frac{T_{fe}\big(h_f+h_b(1-h_f)T_{diff}TR_{f,d}R_b+h_fT_{diff}R_{b,d}+h_b(1-h_f)TR_b\big)(1-T_{diff})}{\big(T_{diff}^2 R_{b,d}R_{f,d}-1\big)\big((1-h_f)(1-h_b)T^2R_bR_f-1\big)} \tag{B.54}$$

Derivation of the direct transmission

Table B.6: Derivation of the direct component of the transmission using listed exponents for the corresponding terms

	T_{fe}	$(1-h_f)$	T	$(1-h_b)$	R_b	R_f	$(1-R_b)$
$T_{1,dir}$	1	1	1	0	0	0	1
$T_{2,dir}$	1	2	3	1	1	1	1
$T_{3,dir}$	1	3	5	2	2	2	1
…							
$\sum_{v=0}^{\infty} f$	T_{fe}	$(1-h_f)^{v+1}$	T^{2v+1}	$(1-h_b)^{v}$	R_f^{v}	R_f^{v}	$(1-R_b)$

$$T_{tot,dir} = \frac{T_{fe}(1-h_f)T(1-R_b)}{1-(1-h_f)(1-h_b)T^2R_bR_f} \tag{B.55}$$

Derivation of the diffuse transmission

Table B.7: Derivation of the diffuse component of transmission using listed exponents for the corresponding terms. The bold formatted numbers indicate the forward direction and the grey numbers the backward direction.

		T_{fe}	h_f	h_b	$(1-d_{rel,f})$	$(1-d_{rel,b})$	T_{diff}	T	$R_{b,d}$	$R_{f,d}$	R_b	R_f	$(1-R_{b,d})$
$T_{1,diff}=$		**1**	**1**	**0**	**0**	**0**	**1**	**0**	**0**	**0**	**0**	**0**	**1**
$T_{2,diff}=$		**1**	**1**	**0**	**0**	**0**	**3**	**0**	**1**	**1**	**0**	**0**	**1**
	+	1	0	1	1	0	2	1	0	1	1	0	1
	+	**1**	**1**	**0**	**1**	**1**	**1**	**2**	**0**	**0**	**1**	**1**	**1**
$T_{3,diff}=$		**1**	**1**	**0**	**0**	**0**	**5**	**0**	**2**	**2**	**0**	**0**	**1**
	+	1	0	1	1	0	4	1	1	2	1	0	1
	+	**1**	**1**	**0**	**1**	**1**	**3**	**2**	**1**	**1**	**1**	**1**	**1**
	+	1	0	1	2	1	2	3	0	1	2	1	1
	+	**1**	**1**	**0**	**2**	**2**	**1**	**4**	**0**	**0**	**2**	**2**	**1**
…													
$\sum_{l=0}^{\infty}\sum_{v=0}^{l} f$		$\boldsymbol{T_{fe}}$	h_f		$(\mathbf{1}-h_f)^v$	$(\mathbf{1}-h_b)^v$	$\boldsymbol{T_{diff}^{1+2k-2v}}$	$\boldsymbol{T^{2v}}$	$\boldsymbol{R_{b,d}}^{k-v}$	$\boldsymbol{R_{f,d}}^{k-v}$	$\boldsymbol{R_b}^v$	$\boldsymbol{R_f}^v$	$(1-R_{b,d})$
$\sum_{l=0}^{\infty}\sum_{v=0}^{l} f$		T_{fe}		h_b	$(1-h_f)^{v+1}$	$(1-h_b)^v$	$T_{diff}^{2+2l-2v}$	T^{2v+1}	${R_{b,d}}^{l-v}$	${R_{f,d}}^{l-v+1}$	${R_b}^{v+1}$	${R_f}^v$	$(1-R_{b,d})$

$$T_{diff}^{forw} = \frac{T_{fe}h_fT_{diff}(1-R_{b,d})}{\left(T_{diff}^2R_{b,d}R_{f,d}-1\right)\left((1-h_b)(1-h_f)T^2R_bR_f-1\right)} \tag{B.56}$$

$$T_{diff}^{backw} = \frac{T_{fe}h_b(1-h_f)T_{diff}^2TR_{f,d}R_b(1-R_{b,d})}{\left(T_{diff}^2R_{b,d}R_{f,d}-1\right)\left((1-h_b)(1-h_f)T^2R_bR_f-1\right)} \tag{B.57}$$

$$T_{tot,diff} = \frac{T_{fe}(h_fT_{diff}+h_b(1-h_f)T_{diff}^2TR_{f,d}R_b)(1-R_{b,d})}{\left(T_{diff}^2R_{b,d}R_{f,d}-1\right)\left((1-h_b)(1-h_f)T^2R_bR_f-1\right)} \tag{B.58}$$

Ray tracing software commonly used for photovoltaic research and development

Table B.8: List of the most popular ray tracing tools used in the photovoltaic community

Software's name	**Contributions in the field of solar research using the corresponding software**
Apex	[159]
Asap	[160]
Daidalos	[125]
Wafer Ray Tracer	[134]
SunSolve	[161]
Rayn	[78]
RaySim	[162]
Sunrays	[126]
Texture	[163]
Tracey	[164]
OpticStudio (Zemax)	[165]
Trace Pro	[166]

Appendix C

Derivation of the numerical approach for diffuse reflection

The following derivation could also be done by purely analytical means using integral expressions, but the following derivation leads to an equation that can directly be implemented in the programming code.

Imagine a circle in that points are randomly placed, such that they are evenly distributed. This is an easy visualization of the orientations diffuse light is incident on a plane, when the lateral position is equivalent to the angle of incidence and the position along the circle line is the orientation of the photon in the azimuth direction. The circle has a radius of 1 and thus is a unit circle. The area of the circle is calculated by $A_c = \pi r^2 = \pi$.

Now a number of smaller centered circles is placed inside the one described above. This step is dividing the circle into circular rings. For our purpose it is sufficient to divide the circle into $N = 90$ of such rings. Each of these rings has an area of $A_{cr} = \pi(r_{n-1}^2 - r_n^2)$. Where $n = \{1, 2, 3, \dots 90\}$ such that we can write

$$A_{cr}(n) = \pi\left(\left(\frac{n-1}{N}\right)^2 - \left(\frac{n}{N}\right)^2\right) \tag{C.1}$$

The total number of points in the circle is ϕ_0 such that the number of points in the circle ring n is $\phi(n) = \phi_0 \cdot \frac{A_{cr}}{A_c} = \phi_0 \cdot f(n)$. The function $f(n)$ was derived in a way that for n we can also write the angles of incidence θ between 1° and 90°

$$f(n) = \left(\frac{n-1}{N}\right)^2 - \left(\frac{n}{N}\right)^2 \rightarrow f(\theta, \lambda) = \left(\frac{\theta - 1°}{90°}\right)^2 - \left(\frac{\theta}{90°}\right)^2 \tag{C.2}$$

To find the diffuse reflection for a given wavelength we now can write

$$\begin{aligned} &R_{diff}(\lambda) \\ &= \frac{\phi_0 \cdot (f(1°,\lambda) \cdot R(1°,\lambda) + f(2°,\lambda) \cdot R(2°,\lambda) + \cdots + f(90°,\lambda) \cdot R(90°,\lambda))}{\phi_0} \\ &= f(1°,\lambda) \cdot R(1°,\lambda) + f(2°,\lambda) \cdot R(2°,\lambda) + \cdots + f(90°,\lambda) \cdot R(90°,\lambda) \end{aligned} \tag{C.3}$$

From this the determination of the diffuse reflection for different wavelengths is possible. As for the case of the analytical model used in this work only one value is necessary, it is meaningful to take the mean value for the wavelengths > 900 nm as the photons with smaller wavelengths do not reach the back surface.

Abbreviations

AOI	Angle of incidence
AR	Anti reflection
BIPV	Building integrated photovoltaic
CdTe	Cadmium telluride solar cell
CIGS	Copper indium gallium selenide solar cell
CUAS	Cologne University of Applied Sciences
c-Si	Crystalline Silicon
DWD	German Meteorological Service (Deutscher Wetterdienst)
DWS	Diamond Wire Sawing
EVA	Ethylene-vinyl-acetate
FCA	Free carrier absorption
FEM	Finite Element Method
GNU	GNU is Not Unix
IBC	Interdigitated back contact solar cell
IPCC	Intergovernmental Panel on Climate Change
LED	Light emitting diode
LLFP	Long-Lived Fission Products
MWSS	Multi Wire Slurry Sawing
PECVD	Plasma enhanced chemical vapour deposition
PERC	Passivated Emitter and Rear Cell
PERD	Passivated Emitter and Rear Directly-contacted
PERF	Passivated Emitter, Rear Floating-junction
PERL	Passivated Emitter Rear Locally-diffused
PERT	Passivated Emitter Rear Totally-diffused
PERX	Abbreviation containing all the technologies where the name starts with 'PER'
PET	Polyethylenterephthalat
PTB	Federal Institute of Physical Technology in Braunschweig
PV	Photovoltaic
PVB	Polyvinyl Butyral
QNR	Quasi neutral region
RRR	Rau's Reciprocity Relation
SCR	Space charge region
SMARTI	Solar MATLAB Ray Tracing Implementation
SQ-limit	Shockley-Queisser-limit
STC	Standard test conditions
VAS	Variable angle spectroscopy
WRT	Wafer Ray Tracer

Symbols

Symbol	Description	Si-Units
a_b	Variable containing all constant parameters of the generation profile due to the first forward pass in the base	$[m^{-2}s^{-1}\mu m^{-1}]$
A	Absorption	[ ]
A_{AR}	Parasitic absorption in the AR-coating	[ ]
A_{back}	Absorption in the back contact	[ ]
A_c	Total cell area	$[m^2]$
A_{fe}	Absorption inside the AR-coating	[ ]
A_{FCA}	Free carrier absorption	[ ]
A_{grid}	Parasitic absorption in the contact grid	[ ]
A_l	Parasitic absorption in a layer except the seiconductor	[ ]
A_{Pa}	Parasitic absorption	[ ]
A_{rc}	Area of the reference cell	$[m^2]$
A_{sc}	Absorption in the semiconductor material	[ ]
A_{sp}	Inner surface of the integrating sphere	$[m^2]$
A_{tc}	Area of the test cell	$[m^2]$
A_{tot}	Total absorption in the semiconductor including FCA	[ ]
AM	Airmass	
b_b	Variable containing all constant parameters of the generation profile due to the first backward pass in the base	$[m^{-2}s^{-1}\mu m^{-1}]$
B	Magnetic flux density	$[T]$
$BRDF$	Bidirectional Reflection Distribution Function	[ ]
c_b	Variable containing all constant parameters of the generation profile due to all subsequent forward passes in the base	$[m^{-2}s^{-1}\mu m^{-1}]$
C	Factor for the determination of the free carrier absorption	[ ]
c_0	Speed of light in vacuum	$[m/s]$
c_m	Phase velocity of light in medium	$[m/s]$
d_b	Variable containing all constant parameters of the generation profile due to all subsequent backward passes in the base	$[m^{-2}s^{-1}\mu m^{-1}]$
d_{AR}	Thickness of AR-coating	$[m]$
d_j	Thickness of j^{th} thin-film	$[m]$
D_n	Diffusion coefficient for electrons	$[m^2/s]$
D_p	Diffusion coefficient for holes	$[m^2/s]$
E	Electric field strength	$[V/m]$
E_0	Amplitude of the electric field	$[V/m]$
E_i	Incident electric field strength	$[V/m]$
EQE	External Quantum Efficiency	[ ]

f	frequency	$[1/s]$
$f_{a,b}$	Density of absorbed photons due to the first forward pass in the base	$[m^{-2}s^{-1}\mu m^{-1}]$
$f_{a,e}$	Density of absorbed photons due to the first forward pass in the emitter	$[m^{-2}s^{-1}\mu m^{-1}]$
$f_{a,scr}$	Density of absorbed photons due to the first forward pass in the SCR	$[m^{-2}s^{-1}\mu m^{-1}]$
f_{AM}	Air mass correction factor	[ ]
$f_{b,b}$	Density of absorbed photons due to the first backward pass in the base	$[m^{-2}s^{-1}\mu m^{-1}]$
$f_{b,e}$	Density of absorbed photons due to the first backward pass in the emitter	$[m^{-2}s^{-1}\mu m^{-1}]$
$f_{b,scr}$	Density of absorbed photons due to the first backward pass in the SCR	$[m^{-2}s^{-1}\mu m^{-1}]$
f_{BE}	Bose-Einstein distribution function	[ ]
$f_{c,b}$	Density of absorbed photons due to all subsequent forward passes in the base	$[m^{-2}s^{-1}\mu m^{-1}]$
$f_{c,e}$	Density of absorbed photons due to all subsequent forward passes in the emitter	$[m^{-2}s^{-1}\mu m^{-1}]$
$f_{c,scr}$	Density of absorbed photons due to all subsequent forward passes in the SCR	$[m^{-2}s^{-1}\mu m^{-1}]$
$f_{d,b}$	Density of absorbed photons due to all subsequent backward passes in the base	$[m^{-2}s^{-1}\mu m^{-1}]$
$f_{d,e}$	Density of absorbed photons due to all subsequent backward passes in the emitter	$[m^{-2}s^{-1}\mu m^{-1}]$
$f_{d,scr}$	Density of absorbed photons due to all subsequent backward passes in the SCR	$[m^{-2}s^{-1}\mu m^{-1}]$
f_{EQE}	Angular correction factor for EQE	[ ]
f_{IQE}	Angular correction factor for IQE	[ ]
f_{sp}	Port fraction of the integrating sphere	[ ]
FF	Fill factor	[ ]
G	Generation rate	$[m^{-3}s^{-1}\mu m^{-1}]$
G_{f1}	Generation rate at first forward pass	$[m^{-3}s^{-1}\mu m^{-1}]$
$G_{f1,b}$	Generation rate at first forward pass in the base	$[m^{-3}s^{-1}\mu m^{-1}]$
G_{fn}		$[m^{-3}s^{-1}\mu m^{-1}]$
G_{b1}	Generation rate at first backward pass	$[m^{-3}s^{-1}\mu m^{-1}]$
$G_{b1,b}$	Generation rate at first backward pass in the base	$[m^{-3}s^{-1}\mu m^{-1}]$
G_{bn}		$[m^{-3}s^{-1}\mu m^{-1}]$
h	Planck's constant	$[Js]$
h_b	Haze factor of the back side of the absorber	[ ]
h_f	Haze factor oft he front side of the absorber	[ ]
H	Magnetic field strength	$[A/m]$
I	Total current	$[A]$
I_b	Beam irradiance	$[W/m^2]$
I_g	Global irradiance	$[W/m^2]$

I_i	Irradiance on cell or module surface	$[W/m^2]$
I_{sc}	Total short circuit current	$[A]$
$I_{sc,rc}$	Short circuit current of the reference cell	$[A]$
$I_{sc,tc}$	Short circuit current of the test cell	$[A]$
IAM	Incidence angle modifier	[ ]
IQE	Internal Quantum Efficiency	[ ]
IQE_{meas}	Measured Internal Quantum Efficiency	[ ]
IQE^*	Simulated IQE corresponding to IQE_{meas}	[ ]
j	Current density	$[A/m^2]$
j_0	Saturation current density	$[A/m^2]$
j_n^{drift}	Current density due to drift of electrons	$[A/m^2]$
j_n^{diff}	Current density due to diffusion of electrons	$[A/m^2]$
j_p^{drift}	Current density due to drift of holes	$[A/m^2]$
j_p^{diff}	Current density due to diffusion of holes	$[A/m^2]$
j_{sc}	Short circuit current density	$[A/m^2]$
k	Extinction coefficient	$[1/m]$
k_0	Extinction coefficient of the incoming medium	$[1/m]$
k_B	Boltzmann coefficient	$[Jk^{-1}]$
k_j	Extinction coefficients of j^{th} thin films	$[1/m]$
k_m	Extinction coefficient of the adjacent medium	$[1/m]$
K_E	Relative permittivity	[ ]
K_M	Relative permeability	[ ]
L_e	Diffusion length in the emitter	$[m]$
L_{eff}	Effective diffusion length	$[m]$
L_b	Diffusion length in the base	$[m]$
m	Diode ideality factor	[ ]
M_{bb}	Share of busbar surface	[ ]
M_{cell}	Share of cell surface	[ ]
M_{dark}	Dark measurement	$-$
M_{EQE}	Measured EQE value	[ ]
M_{fi}	Share of contact fingers	[ ]
M_{meas}	Measurement result	$-$
M_{real}	Real value of a quantity under investigation	$-$
M_{ref}	Measured quantity as reference	$-$
M_{ts}	Measured value of a test sample	$-$
M_v	Transfer matrix of the v^{th} thin-film	[ ]
n	Refractive index	[ ]
n_0	Refractive index of the ambient	[ ]
n_1	Refractive index of first medium	[ ]
n_c	Free electron concentration	$[m^{-3}]$
n_i	Intrinsic carrier concentration	$[m^{-3}]$
n_j	Refractive index of j^{th} thin film	[ ]
n_{jct}	Injected charges at the junction	$[m^{-2}s^{-1}]$
n_m	Refractive index of adjacent medium	[ ]

n_s	Refractive index of AR-coating	[ ]
N	Complex refractive index	[ ]
N_0	Complex refractive index of the ambient medium	[ ]
N_A	Acceptor carrier concentration	$[m^{-3}]$
N_A^-	Ionized acceptor carrier concentration	$[m^{-3}]$
N_D	Donor carrier concentration	$[m^{-3}]$
N_D^-	Ionized donor carrier concentration	$[m^{-3}]$
$N_{D,e}$	Donor carrier concentration in the emitter	$[m^{-3}]$
N_j	Complex refractive index of different applied thin layers	[ ]
N_m	Complex refractive index of the adjacent medium	[ ]
N_s	Number of individual measurements	[ ]
N_x	Carrier concentration for the determination of the free carrier absorption	$[m^{-3}]$
$NOCT$	Normal operating cell temperature	$[K]$
p_{bb}	Pitch between busbars	$[m]$
p_c	Free hole concentration	$[m^{-3}]$
p_{sc}	Share of absorption in semiconductor without FCA in relation to the total absorption	[ ]
p_{FCA}	Share of FCA in relation to the total absorption	[ ]
p_{fi}	Pitch between fingers	$[m]$
P_{mpp}	Power at maximum power point	$[W]$
q	Elementary charge	$[C]$
r_{ij}	Rate of particle transition from state i to j	$[\,s^{-1}]$
r_E	Ratio of the reflected and the incident complex electric field amplitude	[ ]
R	Reflection	[ ]
R_b	Internal back side reflectivity of direct light	[ ]
R_{b1}	Internal back side reflectivity of direct light at the first interaction	[ ]
$R_{b,d}$	Internal back side reflectivity of diffuse light	[ ]
R_{bv}	Internal back side reflectivity of direct light at the v^{th} interaction	[ ]
R_{esc}	Escape reflection	[ ]
R_{fe}	External reflection	[ ]
R_f	Internal front side reflectivity of direct light	[ ]
R_{f1}	Internal front side reflectivity of direct light at the first interaction	[ ]
$R_{f,d}$	Internal front side reflectivity of diffuse light	[ ]
R_{fv}	Internal front side reflectivity of direct light at the v^{th} interaction	[ ]
R_F	Fresnel reflection	[ ]
R_p	Reflection of p-polarized light	[ ]
R_s	Reflection of s-polarized light	[ ]

R_{sp}	Reflectivity of the inner surface of an integrating sphere	[ ]
R_{tot}	Reflection including external and escape reflection	[ ]
R_s	Series resistance	$[\Omega]$
R_{sh}	Shunt resistance	$[\Omega]$
t	Time	$[s]$
t_{ij}	Probability for a transition from state i to j	[ ]
s	Standard deviation	$-$
S_f	Front surface recombination velocity	$[1/m^2 s]$
S_r	Rear surface recombination velocity	$[1/m^2 s]$
$S_{\bar{M}}$	Standard error of the mean	$-$
SEM	Standard error of the mean	$-$
SM_{sp}	Port multiplier of an integrating sphere	[ ]
SR	Spectral response	$[A/W]$
SR_{rc}	Spectral response of the reference cell	$[A/W]$
SR_{tc}	Spectral response of the test cell	$[A/W]$
t_E	Ratio of the transmitted and the incident complex electric field amplitude	[ ]
T	Transmission of specular light through the solar cell	[ ]
T_{amb}	Ambient temperature	
$T_{b,d}$	Internal transmissivity of the back side for diffuse light	[ ]
T_{cell}	Temperature of the solar cell	$[K]$
$T_{d,1}$	Transmission of specular light at the first forward pass	[ ]
$T_{d,v}$	Transmission of specular light at the v^{th} forward pass	[ ]
T_{diff}	Transmission of diffuse light through solar cell	[ ]
T_f	Internal transmissivity of the front side for specular light	[ ]
$T_{f,d}$	Internal transmissivity of the front side for diffuse light	[ ]
T_s	Temperature of the sun	$[K]$
$T_{u,1}$	Transmission of specular light at the first backward pass	[ ]
$T_{u,v}$	Transmission of specular light at the v^{th} backward pass	[ ]
U	Recombination rate	$[1/m^3 s]$
U_{eff}	Effective recombination rate	$[1/m^3 s]$
V	Voltage	$[V]$
V_{bi}	Built-in voltage	$[V]$
V_{oc}	Open circuit voltage	$[V]$
w_{bb}	Width of the busbars	$[m]$
w_{fi}	Width of the finger	$[m]$
W	Total width of the solar cell	$[m]$

W_b	Width of the base region	$[m]$
W_e	Width of the emitter region	$[m]$
W_{scr}	Width of space charge region	$[m]$
$W_{scr,e}$	Width of space charge region inside the emitter	$[m]$
$W_{scr,b}$	Width of space charge region inside the base	$[m]$
Y	Optical admittance	$[S]$
Z	Pathlength enhancement factor	[ ]
Z_i	Number of particles in state i	$-$
	Greek and other symbols	
α	Absorption coefficient	$[1/m]$
α'	Effective absorption coefficient	$[1/m]$
α_{FCA}	Absorption coefficient for free carrier absorption	$[1/m]$
$\alpha_{FCA,e}$	Absorption coefficient for free carrier absorption in the emitter	$[1/m]$
$\alpha_{FCA,scr}$	Absorption coefficient for free carrier absorption in the space charge region	$[1/m]$
$\alpha_{FCA,b}$	Absorption coefficient for free carrier absorption in the base	$[1/m]$
α_g	Absorptivity of a gray body	[ ]
γ	Exponent for the determination of the free carrier absorption	[ ]
δ_a	Relative random error produced by angle positioning	[ ]
δ_{EQE}	Relative random error of the EQE measurement	[ ]
$\delta_{f,IQE}$	Relative random error of the f_{IQE} determination	[ ]
δ_i	Relative random error produced by process i	[ ]
δ_j	Phase shift factor in the j^{th} thin-film	[ ]
δ_l	Relative random error produced by lamp flickering and variation	[ ]
δ_m	Relative random error produced by measuring amplifier	[ ]
δ_p	Relative random error produced by positioning of the sample	[ ]
δ_R	Relative random error of the reflection measurement	[ ]
δ_T	Relative random error produced by temperature variation	[ ]
ε	Permittivity	$[F/m]$
ε_g	Emissivity of a gray body	[ ]
ε_0	Permittivity in vacuum	$[F/m]$
E	Energy	$[J]$
E_{ph}	Energy of a photon	$[J]$
η_0	Admittance of the incoming medium	$[S]$
η_1	Admittance of the adjacent medium	$[S]$
η_c	Collection probability	[ ]

$\eta_{back,b}$	Collection probability of charge carriers generated by light its backward pass in the base	[ ]
$\eta_{back,e}$	Collection probability of charge carriers generated by light its backward pass in the emitter	[ ]
$\eta_{forward,b}$	Collection probability of charge carriers generated by light its forward pass in the base	[ ]
$\eta_{forward,e}$	Collection probability of charge carriers generated by light its forward pass in the emitter	[ ]
η_p	Tilted optical admittance for p-polarized light	$[S]$
η_s	Tilted optical admittance for s-polarized light	$[S]$
η_{SQ}	Shockley-Queisser efficiency	[ ]
θ_0	Transmission angle in the ambient medium (equal to θ_i)	$[rad]$
θ_1	Transmission angle at first backward pass through cell	$[rad]$
θ_{eff}	Effective transmission angle	$[rad]$
θ_i	Angle of incidence	$[rad]$
θ_j	Transmission angle in the j^{th} thin-film	$[rad]$
θ_n	Transmission angle at n^{th} pass through cell	$[rad]$
θ_r	Angle of reflection	$[rad]$
ν	Frequency	$[1/s]$
λ	Wavelength	$[m]$
μ	Permeability	$[H/m]$
μ_0	Permeability in vacuum	$[H/m]$
μ_n	Mobility of electrons	$[m^2/Vs]$
μ_p	Mobility of holes	$[m^2/Vs]$
σ	Conductivity	[Ωm]
σ_{SB}	Stefan-Boltzmann constant	$[Wm^{-2}K^{-4}]$
∇	Nabla operator	[ ]
ρ	Total electric charge density	$[C/m^3]$
τ_n	Electron lifetime	$[s]$
φ	Electrostatic potential	$[V]$
ϕ_{abs}	Number of absorbed photons	$[m^{-2}s^{-1}\mu m^{-1}]$
$\phi_{abs,sc}$	Number of absorbed photons in the semiconductor excluding FCA	$[m^{-2}s^{-1}\mu m^{-1}]$
$\phi_{abs,tot}$	Number of absorbed photons in the semiconductor including FCA	$[m^{-2}s^{-1}\mu m^{-1}]$
ϕ_{bb}	Black body radiation	$[m^{-2}s^{-1}\mu m^{-1}]$
ϕ_{em}	Emitted photon flux	$[m^{-2}s^{-1}\mu m^{-1}]$
$\phi_{esc,v}$	Number of photons escaping from the solar cell or module after the v^{th} transition	$[m^{-2}s^{-1}\mu m^{-1}]$
ϕ_i	Photon density incident on the cell or module surface	$[m^{-2}s^{-1}\mu m^{-1}]$
ω	Angular velocity	$[rad/s]$
Δn	Excess carrier density	$[1/m^3]$

$\Delta\phi_{em}$	Excess emitted photon flux	$[m^{-2}s^{-1}\mu m^{-1}]$
Δz	Absolute reduction of the absorption depth	$[m]$

References

[1] IPCC, "Climate change 2014: Mitigation of climate change Working Group III contribution to the Fifth Assessment Report of the Intergovernmental Panel on Climate Change," Intergovernmental Panel on Climate Change (IPCC), New York NY, 2014.

[2] E. de Sanctis, S. Monti, and M. Ripani, *Energy from Nuclear Fission: An Introduction*. Cham: Springer, 2016.

[3] A. G. Ortiz, "Air quality in Europe: 2015 report," European Environment Agency (EEA), 2015.

[4] IPCC, "Climate Change 2013: The Physical Science Basis," Intergovernmental Panel on Climate Change (IPCC), 2013.

[5] J. Barnett and W. N. Adger, "Climate change, human security and violent conflict," *Political Geography*, vol. 26, no. 6, pp. 639–655, 2007.

[6] E. J. Kendon *et al.,* "Heavier summer downpours with climate change revealed by weather forecast resolution model," *Nature Climate Change*, vol. 4, no. 7, pp. 570–576, 2014.

[7] W. Cai *et al.,* "Increasing frequency of extreme El Niño events due to greenhouse warming," *Nature Climate Change*, vol. 4, no. 2, pp. 111–116, 2014.

[8] A. Dai, "Increasing drought under global warming in observations and models," *Nature Climate Change*, vol. 3, no. 1, pp. 52–58, 2013.

[9] R. Reuveny, "Climate change-induced migration and violent conflict," *Political Geography*, vol. 26, no. 6, pp. 656–673, 2007.

[10] B. W. Brook, E. C. Ellis, M. P. Perring, A. W. Mackay, and L. Blomqvist, "Does the terrestrial biosphere have planetary tipping points?," *Trends in ecology & evolution*, vol. 28, no. 7, pp. 396–401, 2013.

[11] T. M. Lenton *et al.,* "Tipping elements in the Earth's climate system," *PNAS*, no. vol. 105 no. 6, pp. 1786–1793, 2008.

[12] M. A. Delucchi and M. Z. Jacobson, "Providing all global energy with wind, water, and solar power, Part II: Reliability, system and transmission costs, and policies," *Energy Policy*, vol. 39, no. 3, pp. 1170–1190, 2011.

[13] S. Singer, "The Energy Report: 100% Renewable Energy By 2050," 2011.

[14] S. Hegedus and A. Luque, "Achievements and Challenges of Solar Electricity from Photovoltaics," in *Handbook of photovoltaic science and engineering*, A. Luque, Ed., 2nd ed., Chichester: Wiley, 2011.

[15] Fraunhofer Institut for Solar Energy Systems (ISE), "Photovoltaics Report," Feb. 2018.

[16] ITRPV, "International Technology Roadmap for Photovoltaic: 2016 Results including maturity report," Eighth edition, Sep. 2017.

[17] C. Huennekes, "Draft SET-Plan TWP PV Implementation Plan," Oct. 2017.

[18] German Meteorological Service (DWD), *Weather data Lindenberg (Germany)*. Provided by HTW-Berlin.

[19] C. Ulbrich, "Spectral and directional dependence of light-trapping in solar cells," Dissertation, Aachen, 2011.

[20] G. Dennler *et al.,* "Angle dependence of external and internal quantum efficiencies in bulk-heterojunction organic solar cells," (en), *J. Appl. Phys.*, vol. 102, no. 5, p. 54516, 2007.

[21] I. Geisemeyer *et al.,* "Angle Dependence of Solar Cells and Modules: The Role of Cell Texturization," (en), *IEEE J. Photovoltaics*, pp. 1–6, 2016.

[22] F. Plag, I. Kröger, T. Fey, F. Witt, and S. Winter, "Angular-dependent spectral responsivity-Traceable measurements on optical losses in PV devices," (en), *Prog Photovolt Res Appl*, vol. 8, no. 3, p. 121, 2017.

[23] U. Blieske and G. Stollwerck, "Glass and Other Encapsulation Materials," in *Semiconductors and semimetals, Advances in Photovoltaics: Part 2*: Elsevier, 2013, pp. 199–258.

[24] G. Seifert, I. Schwedler, J. Schneider, and R. B. Wehrspohn, "Light Management in Solar Modules," in *Photon management in solar cells*, R. B. Wehrspohn, U. Rau, and A. Gombert, Eds., Weinheim, Germany: Wiley-VCH, 2015, pp. 323–346.

[25] H. K. Raut, V. A. Ganesh, A. S. Nair, and S. Ramakrishna, "Anti-reflective coatings: A critical, in-depth review," (af), *Energy Environ. Sci.*, vol. 4, no. 10, p. 3779, 2011.

[26] K.-J. Chen, F.-Y. Hung, T.-S. Lui, L.-H. Chen, and Y.-W. Chen, "A study of green Sn–xZn photovoltaic ribbons for solar cell application," *Solar Energy Materials and Solar Cells*, vol. 143, pp. 561–566, 2015.

[27] S. W. Glunz, R. Preu, and D. Biro, "Crystalline Silicon Solar Cells," in *Comprehensive Renewable Energy*: Elsevier, 2012, pp. 353–387.

[28] M. A. Green, "The Passivated Emitter and Rear Cell (PERC): From conception to mass production," *Solar Energy Materials and Solar Cells*, vol. 143, pp. 190–197, 2015.

[29] I. Tobias, C. d. Canizo, and J. Alonso, "Crystalline Silicon Solar Cells and Modules," in *Handbook of photovoltaic science and engineering*, A. Luque, Ed., 2nd ed., Chichester: Wiley, 2011.

[30] S. C. Baker-Finch and K. R. McIntosh, "Reflection distributions of textured monocrystalline silicon: Implications for silicon solar cells," (en), *Prog. Photovolt: Res. Appl.*, pp. n/a-n/a, 2012.

[31] Y. Jiang *et al.,* "Hybrid process for texturization of diamond wire sawn multicrystalline silicon solar cell," *Phys. Status Solidi RRL*, vol. 10, no. 12, pp. 870–873, 2016.

[32] K. R. McIntosh, J. N. Cotsell, A. W. Norris, N. E. Powell, and B. M. Ketola, "An optical comparison of silicone and EVA encapsulants under various spectra," in *Photovoltaic Specialists Conference (PVSC), 2010 35th IEEE*, Honolulu, HI, USA, 2010.

[33] H. Wirth, C. Wiesmeier, and K.-A. Weiß, *Photovoltaic modules: Technology and reliability*. Berlin: De Gruyter, 2016.

[34] J.M. Rodrfguez, I. Tobias, and A. Luque, "Random pyramidal texture modelling A. Luque," *Solar Energy Materials and Solar Cells*, no. 45, pp. 241–253, 1997.

[35] *Measurement of Photovoltaic Current- Voltage Characteristics (2nd edn). 60904-3*, IEC 60904-3, 1989.

[36] G. Makrides, B. Zinsser, M. Schubert, and G. E. Georghiou, "Energy yield prediction errors and uncertainties of different photovoltaic models," (en), *Prog Photovolt Res Appl*, vol. 21, no. 4, pp. 500–516, 2013.

[37] S. Pelland, G. Galanis, and G. Kallos, "Solar and photovoltaic forecasting through post-processing of the Global Environmental Multiscale numerical weather prediction model," (en), *Prog. Photovolt: Res. Appl.*, vol. 21, no. 3, pp. 284–296, 2013.

[38] E. Lorenzo, "Energy Collected and Delivered by PV Modules," in *Handbook of photovoltaic science and engineering*, A. Luque, Ed., 2nd ed., Chichester: Wiley, 2011.

[39] J. Zorrilla-Casanova *et al.,* "Losses produced by soiling in the incoming radiation to photovoltaic modules," (en), *Prog. Photovolt: Res. Appl.*, no. 21, pp. 790–796, 2012.

[40] D. C. Jordan and S. R. Kurtz, "Photovoltaic Degradation Rates - An Analytical Review," NREL, 2012.

[41] D. C. Jordan, S. R. Kurtz, K. VanSant, and J. Newmiller, "Compendium of photovoltaic degradation rates," *Prog. Photovolt: Res. Appl.*, vol. 24, no. 7, pp. 978–989, 2016.

[42] H. Schmidt, B. Burger, and J. Schmid, "Power Conditioning for Photovoltaic Power Systems," in *Handbook of photovoltaic science and engineering*, A. Luque, Ed., 2nd ed., Chichester: Wiley, 2011.

[43] C. M. Whitaker, T. U. Townsend, A. Razon, R. M. Hudson, and X. Vallve, "PV Systems," in *Handbook of photovoltaic science and engineering*, A. Luque, Ed., 2nd ed., Chichester: Wiley, 2011.

[44] A. Parretta, A. Sarno, and L. R.M. Vicari, "Effects of solar irradiation conditions on the outdoor performance of photovoltaic modules," (en), *Optics Communications*, vol. 153, no. 1-3, pp. 153–163, 1998.

[45] J. A. Kratochvil, W. E. Boyson, and D. L. King, "Photovoltaic array performance model," Sandia National Laboratories, Albuquerque, 2004.

[46] A. Mermoud and T. Lejeune, "PVsyst 5.21: Contextual Help," PVsyst SA, 2012.

[47] G. Valentin, "PV*SOL Expert 6.0: Manual," Valentin Software, Berlin, 2013.

[48] K. R. Mclntosh, "Lumps, Humps and Bumps: Three Detrimental Effects in the Current-Voltage Curve of Silicon Solar Cells," PhD Thesis, University of New South Wales, 2001.

[49] A. Louwen, A. C. de Waal, R. E. I. Schropp, A. P. C. Faaij, and van Sark, Wilfried G. J. H. M., "Comprehensive characterisation and analysis of PV module performance under real operating conditions," (en), *Prog. Photovolt: Res. Appl.*, vol. 25, no. 3, pp. 218–232, 2017.

[50] J. Kuitche *et al.,* "One year NOCT Round-Robin testing per IEC 61215 standard: 19 - 24 June 2011, Seattle, Washington ; conference proceedings," (en), pp. 2380–2385, 2011.

[51] M. Schweiger *et al.,* "Spectral Analysis of Various Thin-Film Modules Using High Precision Spectral Response Data and Solar Spectral Irradiance Data," in *Proceedings / EU PVSEC 2012, 27th European Photovoltaic Solar Energy Conference and Exhibition*, 2012, pp. 3284–3290.

[52] D. L. King, J. A. Kratochvil, and W. E. Boyson, "Measuring Solar Spectral and Angle-of-incidence Effects on Photovoltaic Modules and Solar Irradiance Sensors," Sandia National Laboratories, Albuquerque, 1997.

[53] N. Reiners, U. Blieske, and S. Omidi, "Modelling and Measuring the Performance of Textured Front Surfaces Under Diffuse Radiation," 31th European Solar Energy Conference and Exhibition (PVSEC): Poster presentation. Hamburg, 2015.
[54] M. Ebert, H. Stascheit, I. Hädrich, and U. Eitner, "The impact of angular dependent loss measurements on PV module energy yield prediction," 29th European PV Solar Energy Conference and Exhibition: Presentation. Amsterdam, 2014.
[55] N. Martin and J. M. Ruiz, "Calculation of the PV modules angular losses under field conditions by means of an analytical model," (en), *Solar Energy Materials and Solar Cells*, vol. 70, no. 1, pp. 25–38, 2001.
[56] J.-A. Jiang, J.-C. Wang, K.-C. Kuo, Y.-L. Su, and J.-C. Shieh, "On evaluating the effects of the incident angle on the energy harvesting performance and MPP estimation of PV modules," (en), *Int. J. Energy Res.*, vol. 38, no. 10, pp. 1304–1317, 2014.
[57] P. Würfel, *Physics of Solar Cells: From Basic Principles to Advanced Concepts,* 3rd ed. s.l.: Wiley-ISTE, 2016.
[58] J. A. Woollam Co. and Inc., "Guide to Using WVASE," J. A. Woollam Co.; Inc., 2012.
[59] E. Hecht, *Optics,* 5th ed. Boston, Columbus, Indianapolis: Pearson, 2017.
[60] D. A. Miller, "Huygens's wave propagation principle corrected," *Optics Letters*, no. Vol. 16, No. 18, pp. 1370–1372, 1991.
[61] H. A. Macleod, *Thin-film optical filters,* 3rd ed. Bristol, Philadelphia: Institute of Physics Pub, 2001.
[62] D. Meschede, *Optics, light, and lasers: The practical approach to modern aspects of photonics and laser physics*. Weinheim, Germany: Wiley-VCH, 2017.
[63] A. Luque, Ed., *Handbook of photovoltaic science and engineering,* 2nd ed. Chichester: Wiley, 2011.
[64] Z. Wen, W. Wang, C. Zhou, and J. Zhang, "Analytical solution for the photocurrent of solar cells with internal reflection," (en), *J. Appl. Phys.*, vol. 111, no. 3, p. 34502, 2012.
[65] P. A. Basore, "PC-1D Installation Manual and User's Guide Version 3.1," (en), *Sandia Report*, 1991.
[66] F. Thuselt, *Physik der Halbleiterbauelemente*. Berlin, Heidelberg: Springer Berlin Heidelberg, 2011.
[67] J. L. Gray, "The Physicsof the Solar Cell," in *Handbook of photovoltaic science and engineering*, A. Luque, Ed., 2nd ed., Chichester: Wiley, 2011, pp. 82–129.
[68] A. Cuevas, "The Recombination Parameter J0," (en), *Energy Procedia*, vol. 55, pp. 53–62, 2014.
[69] W. Shockley, "The Theory of p-n Junctions in Semiconductors and p-n Junction Transistors," *Bell System Technical Journal*, pp. 435–489, 1949.
[70] P. A. Basore, "Extended Spectral Analysis of Internal Quantum Efficincy," (af), *IEEE Twenty Third Photovoltaic Specialists Conference*, Sep. 1993.
[71] R. Brendel, M. Hirsch, R. Plieninger, and J. H. Werner, "Quantum efficiency analysis of thin-layer silicon solar cells with back surface fields and optical confinement," (en), *IEEE Trans. Electron Devices*, vol. 43, no. 7, pp. 1104–1113, 1996.
[72] J. Nelson, *The physics of solar cells*. London: Imperial College Press, 2010.

[73] D. Abou-Ras, *Advanced characterization techniques for thin film solar cells*. Weinheim, Germany: Wiley-VCH Verlag, 2016.

[74] M. Spiegel, B. Fischer, S. Keller, and E. Bucher, "Separation of bulk diffusion length and back surface recombination velocity by improved IQE-analysis," in *28th IEEE Photovoltaic Specialists Conference*, Anchorage, AK, USA, Sep. 2000, pp. 311–314.

[75] S. Keller, M. Spiegel, P. Fath, G. P. Willeke, and E. Bucher, "A critical evaluation of the effective diffusion length determination in crystalline silicon solar cells from an extended spectral analysis," (en), *IEEE Trans. Electron Devices*, vol. 45, no. 7, pp. 1569–1574, 1998.

[76] T. A. Germer, J. C. Zwinkels, and B. K. Tsai, *Spectrophotometry: Accurate Measurement of Optical Properties of Materials*. Burlington: Elsevier Science, 2014.

[77] A. von Finck, M. Trost, S. Schröder, and A. Duparré, "Parallelized multichannel BSDF measurements," (eng), *Optics express*, vol. 23, no. 26, pp. 33493–33505, 2015.

[78] D. Kray, M. Hermle, and S. W. Glunz, "Theory and experiments on the back side reflectance of silicon wafer solar cells," (en), *Prog. Photovolt: Res. Appl.*, vol. 16, no. 1, pp. 1–15, 2008.

[79] P. Shirley, S. R. Marschner, and M. Ashikhmin, *Fundamentals of computer graphics*, 3rd ed. Natick, Mass.: A K Peters, 2010.

[80] E. Yablonovitch, "Statistical ray optics," *J. Opt. Soc. Am.*, vol. 72, no. 7, p. 899, 1982.

[81] C. Ulbrich *et al.*, "Directional selectivity and ultra-light-trapping in solar cells," *phys. stat. sol. (a)*, vol. 205, no. 12, pp. 2831–2843, 2008.

[82] T. Markvart, "Beyond the Yablonovitch limit: Trapping light by frequency shift," *Appl. Phys. Lett.*, vol. 98, no. 7, p. 71107, 2011.

[83] R. Biswas and C. Xu, "Photonic and plasmonic crystal based enhancement of solar cells — Theory of overcoming the Lambertian limit," *Journal of Non-Crystalline Solids*, no. Volume 358, Issue 17, pp. 2289–2294, 2012.

[84] L. Xiaogang *et al.*, "Black silicon: Fabrication methods, properties and solar energy applications," (en), *Energy Environ. Sci.*, vol. 7, no. 10, pp. 3223–3263, 2014.

[85] V. K. Narasimhan and Y. Cui, "Nanostructures for photon management in solar cells," (en), *Nanophotonics*, vol. 2, no. 3, 2013.

[86] S. Kubota, K. Kanomata, B. Ahmmad, J. Mizuno, and F. Hirose, "Optimized design of moth eye antireflection structure for organic photovoltaics," *J Coat Technol Res*, vol. 13, no. 1, pp. 201–210, 2016.

[87] M. Piralaee, A. Asgari, and V. Siahpoush, "Modeling and optimizing the performance of plasmonic solar cells using effective medium theory," *Physics Letters A*, vol. 381, no. 5, pp. 489–493, 2017.

[88] R. Brendel and D. Scholten, "Modeling light trapping and electronic transport of waffle-shaped crystalline thin-film Si solar cells," (en), *Applied Physics A: Materials Science & Processing*, vol. 69, no. 2, pp. 201–213, 1999.

[89] Y. Yang *et al.*, "Characterization of 2-D reflection pattern from textured front surfaces of silicon solar cells," (en), *Solar Energy Materials and Solar Cells*, vol. 115, pp. 42–51, 2013.

[90] N. Reiners, "Effizienzsteigerung von Solarmodulen bei Schräg- und Schwachlichtverhalten : ESOSWA: Abschlussbericht: Ingenieurnachwuchs 2012," 2016.

[91] U. Rau, "Reciprocity relation between photovoltaic quantum efficiency and electroluminescent emission of solar cells," (en), *Phys. Rev. B*, vol. 76, no. 8, 2007.

[92] M. Bokalič, B. E. Pieters, A. Gerber, U. Rau, and M. Topič, "Bandgap imaging in Cu(In,Ga)Se 2 photovoltaic modules by electroluminescence," (af), *Prog. Photovolt: Res. Appl.*, vol. 25, no. 2, pp. 184–191, 2017.

[93] U. Rau *et al.,* "Photocurrent collection efficiency mapping of a silicon solar cell by a differential luminescence imaging technique," *Appl. Phys. Lett.*, vol. 105, no. 16, p. 163507, 2014.

[94] M. Hermle, F. Granek, O. Schultz, and S. W. Glunz, "Analyzing the effects of front-surface fields on back-junction silicon solar cells using the charge-collection probability and the reciprocity theorem," (en), *J. Appl. Phys.*, vol. 103, no. 5, p. 54507, 2008.

[95] J. M. Raguse and J. R. Sites, "Correlation of Electroluminescence With Open-Circuit Voltage From Thin-Film CdTe Solar Cells," (en), *IEEE J. Photovoltaics*, vol. 5, no. 4, pp. 1175–1178, 2015.

[96] Z. Liu, I. M. Peters, Y. S. Khoo, V. Shanmugam, and R. Stangl, "Luminescence Imaging Analysis of Light Trappping in Crystalline SI PV Modules," 31st European Photovoltaic Solar Energy Conference and Exhibition. Hamburg, 2015.

[97] X. Wang and M. S. Lundstrom, "On the Use of Rau's Reciprocity to Deduce External Radiative Efficiency in Solar Cells," (en), *IEEE J. Photovoltaics*, vol. 3, no. 4, pp. 1348–1353, 2013.

[98] T. Mochizuki, C. Kim, M. Yoshita, J. Mitchell, and Z. Lin, "Voc Evaluation of Solar Cells and Modules using absolute EL images," 31st European Photovoltaic Solar Energy Conference and Exhibition. Hamburg, 2015.

[99] T. Kirchartz, *Generalized detailed balance theory of solar cells*. Dissertation. Jülich: Jülich Forschungszentrum, 2009.

[100] U. Rau and R. Brendel, "The detailed balance principle and the reciprocity theorem between photocarrier collection and dark carrier distribution in solar cells," (en), *J. Appl. Phys.*, vol. 84, no. 11, p. 6412, 1998.

[101] W. Shockley and H. J. Queisser, "Detailed Balance Limit of Efficiency of p-n Junction Solar Cells," (af), *J. Appl. Phys.*, vol. 32, no. 3, p. 510, 1961.

[102] C. Donolato, "A reciprocity theorem for charge collection," (da), *Appl. Phys. Lett.*, vol. 46, no. 3, p. 270, 1985.

[103] U. Rau, "Superposition and Reciprocity in the Electroluminescence and Photoluminescence of Solar Cells," (en), *IEEE J. Photovoltaics*, vol. 2, no. 2, pp. 169–172, 2012.

[104] T. Kirchartz *et al.,* "Reciprocity between electroluminescence and quantum efficiency used for the characterization of silicon solar cells," (en), *Prog. Photovolt: Res. Appl.*, vol. 17, no. 6, pp. 394–402, 2009.

[105] G. Lasher and F. Stern, "Spontaneous and Stimulated Recombination Radiation in Semiconductors," *Physical Review*, no. Volume 133, Number 2A, A553-A563, 1964.

[106] P. Würfel, "The chemical potential of radiation," (en), *J. Phys. C: Solid State Phys.*, vol. 15, no. 18, pp. 3967–3985, 1982.

[107] P. Würfel, S. Finkbeiner, and E. Daub, "Generalized Planck's radiation law for luminescence via indirect transitions," *Applied Physics A: Materials Science & Processing*, vol. 60, no. 1, pp. 67–70, 1995.

[108] Z. Liu *et al.,* "A modeling framework for optimizing current density in four-terminal tandem solar cells: A case study on GaAs/Si tandem," (en), *Solar Energy Materials and Solar Cells*, vol. 170, pp. 167–177, 2017.

[109] K.-H. Yang and J.-Y. Yang, "The analysis of light trapping and internal quantum efficiency of a solar cell with DBR back reflector," (en), *Solar Energy*, vol. 83, no. 11, pp. 2050–2058, 2009.

[110] K.-H. Yang and J.-Y. Yang, "The analysis of light trapping and internal quantum efficiency of a solar cell with grating structure," (en), *Solar Energy*, vol. 85, no. 3, pp. 419–431, 2011.

[111] R. Brendel, *Thin-film crystalline silicon solar cells: Physics and technology,* 2nd ed. Weinheim: Wiley-VCH, 2009.

[112] P. Campbell and M. A. Green, "Light trapping properties of pyramidally textured surfaces," (af), *J. Appl. Phys.*, vol. 62, no. 1, p. 243, 1987.

[113] K. O. Davis *et al.,* "Investigation of the Internal Back Reflectance of Rear-Side Dielectric Stacks for c-Si Solar Cells," (en), *IEEE J. Photovoltaics*, vol. 3, no. 2, pp. 641–648, 2013.

[114] W. J. Yang *et al.,* "Internal quantum efficiency for solar cells," (da), *Solar Energy*, vol. 82, no. 2, pp. 106–110, 2008.

[115] R. Woehl, M. Hörteis, and S. W. Glunz, "Analysis of the Optical Properties of Screen-Printed and Aerosol-Printed and Plated Fingers of Silicon Solar Cells," (en), *Advances in OptoElectronics*, vol. 2008, pp. 1–7, 2008.

[116] M. R. Vogt, "Development of Physical Models for the Simulation of Optical Properties of Solar Cell Modules," Dissertation, Gottfried Wilhelm Leibniz Universität, Hannover, 2015.

[117] PV Lighthouse, *Refractive Index Library*. [Online] Available: https://www2.pvlighthouse.com.au/resources/photovoltaic%20materials/refractive%20index/refractive%20index.aspx.

[118] M. Rudiger, J. Greulich, A. Richter, and M. Hermle, "Parameterization of Free Carrier Absorption in Highly Doped Silicon for Solar Cells," (en), *IEEE Trans. Electron Devices*, vol. 60, no. 7, pp. 2156–2163, 2013.

[119] S. C. Baker-Finch, K. R. McIntosh, Di Yan, K. C. Fong, and T. C. Kho, "Near-infrared free carrier absorption in heavily doped silicon," (en), *J. Appl. Phys.*, vol. 116, no. 6, p. 63106, 2014.

[120] K. F. Riley, M. P. Hobson, and S. J. Bence, *Mathematical methods for physics and engineering,* 3rd ed. Cambridge: Cambridge Univ. Press, 2014.

[121] P. A. Basore and D. A. Clugston, *PC1D Version 4 for Windows: From Analysis to Design*. New York: Institute of Electrical and Electronics Engineers; IEEE Service Center, 1996.

[122] H. Haug, A. Kimmerle, J. Greulich, A. Wolf, and E. Stensrud Marstein, "Implementation of Fermi–Dirac statistics and advanced models in PC1D for precise simulations

of silicon solar cells," (en), *Solar Energy Materials and Solar Cells*, vol. 131, pp. 30–36, 2014.

[123] H. Haug, B. R. Olaisen, Ø. Nordseth, and E. S. Marstein, "A Graphical User Interface for Multivariable Analysis of Silicon Solar Cells Using Scripted PC1D Simulations," (en), *Energy Procedia*, vol. 38, pp. 72–79, 2013.

[124] PV Lighthouse, *OPAL 2*: PV Lighthouse, 2012.

[125] H. Holst *et al.*, "Application of a New Ray Tracing Framework to the Analysis of Extended Regions in Si Solar Cell Modules," *Energy Procedia*, vol. 38, pp. 86–93, 2013.

[126] R. Brendel, "Sunrays: A versatile raytracing programm for the photovoltaic community: 12th European Photovoltaic Solar Energy Conference," (en), vol. 1994.

[127] A. S. Glassner, *An introduction to ray tracing*. San Francisco, Calif.: Kaufmann, 2007.

[128] A. Sherrod, *Game graphics programming*. Boston, MA: Course Technology/Charles River Media/Cengage Learning, 2008.

[129] H. Holst, "Development and application of a modular ray tracing framework to multi-scale simulations in photovoltaics," Gottfried Wilhelm Leibnitz Universität Hannover, Hannover, 2015.

[130] Maria Grazia Pia and Georg Weidenspointner, Eds., "Monte Carlo Simulation for Particle Detectors," CERN Council Open Symposium on European Strategy for Particle Physics, Krakow, 2012.

[131] D. Poole, *Linear algebra: A modern introduction,* 4th ed. Stamford, CT: Cengage Learning, 2015.

[132] N. Reiners, "SMARTI 4.0: User manual," 2018.

[133] S. C. Baker-Finch and K. R. McIntosh, "One-dimensional photogeneration profiles in silicon solar cells with pyramidal texture," (en), *Prog. Photovolt: Res. Appl.*, vol. 20, no. 1, pp. 51–61, 2012.

[134] PV Lighthouse, *Wafer Ray Tracer*: PV Lighthouse, 2016.

[135] J. Melskens, S.G.M. Heirman, R. N. Koornneef, M.A.A. Elshinawy, and M. Schouten, "Fast Optical Measurement System: Ultrafast external quantum efficiency measurements on silicon solar cells," (ca), *Solar Energy Materials and Solar Cells*, vol. 173, pp. 6–11, 2017.

[136] B. H. Hamadani, J. Roller, B. Dougherty, and H. W. Yoon, "Versatile light-emitting-diode-based spectral response measurement system for photovoltaic device characterization," *Applied Optics*, vol. 51; Jg. 2012-07-01, no. 19, pp. 4469–4476, 2012.

[137] E. J. Schneller, K. Ogutman, S. Guo, W. V. Schoenfeld, and K. O. Davis, "Crystalline Silicon Device Loss Analysis Through Spatially Resolved Quantum Efficiency Measurements," *IEEE J. Photovoltaics*, vol. 7, no. 4, pp. 957–965, 2017.

[138] J. R. Taylor, *An introduction to error analysis the study of uncertainties in physical measurements*. University Science Books, Sausalito, California, United States.

[139] S. Rein, *Lifetime Spectroscopy: A Method of Defect Characterization in Silicon for Photovoltaic Applications*. Berlin, Heidelberg: Springer-Verlag Berlin Heidelberg, 2005.

[140] T. Haslwanter, *An Introduction to Statistics with Python: With Applications in the Life Sciences*. Cham: Springer, 2016.

[141] *Evaluation of measurement data - Supplement 1 to the GUM*, 2008.

[142] P. A. van Nijnatten, "Optical analysis of coatings by variable angle spectrophotometry," (af), *Thin Solid Films*, vol. 516, no. 14, pp. 4553–4557, 2008.

[143] J. Jaglarz and A. Grabowski, "Optical investigations of AlSi–SiC composites subjected to laser CO2 annealing," (en), *Optics and Lasers in Engineering*, vol. 48, no. 10, pp. 1038–1044, 2010.

[144] A. Fernández-García *et al.,* "Equipment and methods for measuring reflectance of concentrating solar reflector materials," *Solar Energy Materials and Solar Cells*, vol. 167, pp. 28–52, 2017.

[145] A. Parretta, A. Sarno, and H. Yakubu, "Non-destructive optical characterization of photovoltaic modules by an integrating sphere," (en), *Optics Communications*, vol. 161, no. 4-6, pp. 297–309, 1999.

[146] A. Parretta *et al.,* "Angle-dependent reflectance measurements on photovoltaic materials and solar cells," (en), *Optics Communications*, vol. 172, no. 1-6, pp. 139–151, 1999.

[147] P. Maddalena, A. Parretta, A. Sarno, and P. Tortora, "Novel techniques for the optical characterization of photovoltaic materials and devices," (en), *Optics and Lasers in Engineering*, vol. 39, no. 2, pp. 165–177, 2003.

[148] A. Höpe and K.-O. Hauer, "Three-dimensional appearance characterization of diffuse standard reflection materials," *Metrologia*, vol. 47, no. 3, pp. 295–304, 2010.

[149] Labsphere, "A guide to integrating sphere theory and applications," 2017.

[150] SphereOptics, "Integrating Sphere Design and Applications: Technical Information," 2007.

[151] Matthias Winter, Hendrik Holst, Malte R. Vogt, and Pietro P. Altermatt, "Impact of Realistic Illumination on Optical Losses in Si Solar Cell Modules compared to standard Testing Conditions," 31th European PV Solar Energy Conference und Exhibition. Hamburg, 2015.

[152] I. Haedrich, U. Eitner, M. Wiese, and H. Wirth, "Unified methodology for determining CTM ratios: Systematic prediction of module power," *Solar Energy Materials and Solar Cells*, vol. 131, pp. 14–23, 2014.

[153] S. C. Baker-Finch and K. R. McIntosh, "Reflection of normally incident light from silicon solar cells with pyramidal texture," *Prog. Photovolt: Res. Appl.*, vol. 19, no. 4, pp. 406–416, 2011.

[154] M. A. Green, "Self-consistent optical parameters of intrinsic silicon at 300K including temperature coefficients," *Solar Energy Materials & Solar Cells*, no. 92, pp. 1305–1310, 2008.

[155] E. Palik, *Handbook of Optical Constants of Solids Vol I*. Orlando: Academic Press, 1985.

[156] K. R. McIntosh *et al.,* "Increase in external quantum efficiency of encapsulated silicon solar cells from a luminescent down-shifting layer," *Prog. Photovolt: Res. Appl.*, vol. 17, no. 3, pp. 191–197, 2009.

[157] S. Duttagupta, F. Ma, B. Hoex, T. Mueller, and A. G. Aberle, "Optimised Antireflection Coatings using Silicon Nitride on Textured Silicon Surfaces based on Measurements and Multidimensional Modelling," *Energy Procedia*, vol. 15, pp. 78–83, 2012.

[158] N. Tucher, "Analysis of Photonic Structures for Silicon Solar Cells," Dissertation, Fraunhofer Verlag, Albert-Ludwigs-Universität Freiburg im Breisgau, Freiburg, 2017.

[159] N. Reiners, U. Blieske, C. Kirkes, D. Czyba, and W. Minich, Eds., *Inverstigation on Light Trapping Structures Using Ray Tracing*, 2014.

[160] F. Duerr, B. Muthirayan, Y. Meuret, and H. Thienpont, "Benchmarking concentrating photovoltaic systems," Proceedings of the SPIE, Volume 7773, id. 777315, 2010.

[161] PVlighthouse, *SunSolve*. [Online] Available: www.pvlighthouse.com.au/sunsolve. Accessed on: Mar. 16 2018.

[162] J. E. Cotter, "Raysim 6.0 - a free geometrical ray tracing program for silicon solar cells," pp. 1165–1168.

[163] A. W. Smith, A. Rohatgi, and S. C. Neel, "Texture: a ray tracing program for the photovoltaic community: - Photovoltaic Specialists Conference, 1990., Conference Record of the Twenty First IEEE," (en), pp. 426–431, 1990.

[164] D. Alonso-Álvarez, D. Ross, K. R. McIntosh, and B. S. Richards, "Performance of luminescence down shifting for CdTe solar cells as a function of the incident solar spectrum: 3 - 8 June 2012, Austin Convention Center, Austin, Texas," 38th IEEE Photovoltaic Specialists Conference (PVSC). Piscataway, NJ, 2012.

[165] S. Jutteau, J.-F. Guillemoles, and M. Paire, "Study of a micro-concentrated photovoltaic system based on Cu(In,Ga)Se<sub2</sub microcells array," (eng), *Appl. Opt.*, vol. 55, no. 24, pp. 6656–6661, 2016.

[166] S. Pavlovic, V. Stefanovic, and M. Bojic, "Optical simulation of a solar parabolic collector using ray-tracing software TracePro," in Hong Kong, China, 2014, pp. 211–218.

Acknowledgements

These lines are dedicated to those who supported me on my pathway through the ups and downs of this thesis.

First of all I want to warmly thank Prof. Dr. Ulf Blieske from the TH Köln - University of Applied Sciences who initiated the research project that this thesis is based on and who trusted in me from the start. He opened many doors for me and introduced me to many interesting people from the PV community. Whenever there was an obstacle on my way, he stood by my side and helped me find a solution.

I am deeply grateful that Prof. Dr. Susanne Siebentritt from the University of Luxembourg who was willing to supervise my thesis. She was the one who pushed me to the right level of scientific research and who invested a lot of time and passion to discuss the topic with me. It was a great pleasure and honor working together with such a great scientist.

Thank you also to Ludger Wirtz who joined the supervision team and thus invested his valuable time into the correction and reading of this thesis.

The TH Köln - University of Applied Sciences is an inspiring and collegial place to work. I am particularly thankful for the nice colleagues with whom I shared an office. Johannes Ruloff who also shared the fortune of writing a thesis was always at my side and always had an open ear for my professional as well as my social concerns.

I am also thankful for the many content-related discussions and nice social moments I was able to share with the other colleagues from the office, namely Tobias Kunze, Christian Weger, Julia Müller-Ost, Tobias Rehm, and Lukas Hilger.

The professors, scientific assistants and students who form the Cologne Institute for Renewable Energy (CIRE) inspired me with their enthusiasm and constantly reminded me on why I started working in the field of renewable energy.

Special thanks belong to Rudolf Gecke who helped me out with much practical advice, Stefanie Könen-Sagui who complemented the CIRE with her cheerful nature, Christian Brosig who always reminded me of how much of a difference we can make in our everyday lives and Jan Bollenbacher who helped me out with my programming problems. A warm thank you goes to Iris Müser, who was always present when I needed advice on administrative issues and supported everyone with what we needed to get our work done.

The scientific assistants working at the Institute of Applied Optics and Electronics always helped me out when I needed support with my measurements. A special thank goes to Klaus Dollinger for many fruitful discussions and practical support.

I am thankful for numerous discussions with scientists from different research institutes and universities all over the world who helped me to obtain new ideas and to overcome obstacles. A special thank goes to Pietro Altermatt, who supported me with simulation tools and his wisdom concerning the optics of PV. The Fraunhofer ISE in Freiburg as well as in Gelsenkirchen supported us with solar cell samples. Dr. Dietmar Borchert from the ISE Gelsenkirchen permitted me to use the institute's Perkin Elmer UV/VIS spectrometer several times and always had an open ear for my questions. Keith McIntosh from PV-Lighthouse helped me out several times on simulation topics.

I would also like to thank my friend Johannes Pernpeintner from the German Centre for Aviation and Space Travel (DLR) who helped me out several times with specific problems I ran into.

Felix Schubert from the company Aescusoft that constructed the spectral response system which I modified helped me solving multiple measurement problems.

I would like to express my great respect and recognition to Karen Schneider who proofread my sometimes unconventional English, not only correcting the spelling but also getting into the content of the thesis.

Thank also goes to all the students who I helped supervise in projects, Bachelor's and Master's theses. Even though I often had the impression of losing time for my own research, in reality I learned quite a bit by explaining and discussing the topics with them.

I also want to thank my friends who, especially in the last few months, had too often received the answer that I couldn't find the time to meet them. Thank you for still being there for me.

Of course without my parents it would have never been possible to reach this point. They always believed in me and I know that I can always rely on them. Thank also to my brothers and my sister who I admire and who are great idols for me.

But to be honest, I owe most of my thankfulness to the two persons who make the sun shine for me every day: my girlfriend Nina Peter and our daughter Tamina. I am sorry for the hard time and I'm ever so grateful to have you by my side!